PARAMETRIC STUDIES OF INDUCED

POLARIZATION SPECTRA

by

Grant Whitney De Witt

A thesis submitted to the faculty of The
University of Utah in partial fulfillment of the requirements
for the degree of

Master of Science

in

Geophysics

Department of Geology and Geophysics

The University of Utah

March 1979

THE UNIVERSITY OF UTAH GRADUATE SCHOOL

SUPERVISORY COMMITTEE APPROVAL

of a thesis submitted by

Grant Whitney De Witt

I have read this thesis and have found it to be of satisfactory quality for a master's degree.

_1-19-78_
Date

Dr. William R. Sill
Chairman, Supervisory Committee

I have read this thesis and have found it to be of satisfactory quality for a master's degree.

_1-30-78_
Date

Dr. Ralph T. Shuey
Member, Supervisory Committee

I have read this thesis and have found it to be of satisfactory quality for a master's degree.

_1-20-78_
Date

Dr. William T. Parry
Member, Supervisory Committee

ABSTRACT

In order to understand quantitatively the various parameters that
control the IP response in rocks, a series of measurements have been
made on artificially prepared "rock" samples. These samples are
prepared from mixtures of quartz sand, ore mineral grains and a
cementing agent. The controlled parameters are concentrations of ore
mineral, grain size, grain shape, mineralogy, porosity and pore
structure.

A theoretical complex resistivity rock model based on layered
spheres is derived. It accounts for the microscopic charge separation
within the diffuse zones between the electrolyte and mineral grains
and the macroscopic decay of that charge build up through out the
rock. Using inversion techniques the data are compared to the rock
model parameters of, background resistivity (ρ_1), mineral grain radius
(a), Warburg impedance (A), the frequency dependence (c) of the
Warburg impedance, the volume fraction (V) of the mineral, and the
resistivity contrast between the electrolyte (ρ_e) and the mineral
(ρ_3). Results indicate that at low concentrations some of the
observed dependencies are in approximate agreement with the rock
model. The frequency range at which the dispersive region of the
complex resistivity occurs was observed to be largely a function of
ρ_1, a and A, which represent macroscopic rock conditions. Due to the
rather limited range observed for the Warburg impedance of different

minerals in various electrolyte concentrations, the position of the dispersion is a stronger function of ρ_1 and a. The magnitude of the phase response, a function of a microscopic charge separation in the diffuse zones, was observed to depend on V, ρ_3 and ρ_e . The volume fraction (V) of the mineral is relative to the conductive elements within the rock. Such conductive elements include the mineral, the electrolyte and clay type minerals (i.e. minerals which have a capacity for cation exchange). The degree of charge separation (polarization) was observed to be a strong function of the resistivity contrast between the electrolyte and the mineral. The frequency dependence (c) or the asymptotic phase slope was observed to be a function of the range of mineral grain sizes. For a limited range of grain sizes the frequency dependence (c) was around 0.5 indicating a simple Warburg diffusion impedance. A larger range of grain sizes resulted in smaller phase slopes due to the summation of dispersions, one for each grain size.

A similar theoretical development for layered ellipsoids is combined with mixing formulas of Fricke (1953) for dispersed triaxial ellipsoids, which are then extended to include the effect of particle shape and frequency dependent behavior (complex conductivity). For some cases of nonspherical sample conditions a simple spherical model could distinguish textural differences of synthetic samples constructed to test the ellipsoidal model. With an appropriate regrouping of parameters the above model can be expressed in terms of a simple Cole-Cole model for the relaxation spectrum and thus can be related to the results of in situ field measurements.

The inversion of core sample and in situ field IP spectra to the spherical model gave parameter results and trends which were approximately explained in some of the actual observations of rock and field site conditions. Possible applications of the model to in situ field IP measurements over disseminated and veined deposits include indication of

1. electrolyte resistivity, porosity and/or alteration mineral (e.g. "clay") content variations.

2. a conductive mineral volume fraction relative to the pore volume and the "clay" content.

3. a distinction between a random distribution of mineral shapes (e.g. veinlets) or a preferred orientaion.

4. a relative difference between dominant length scales (e.g. grain sizes) and/or dominant mineral Warburg impedance values between two different in situ IP measurements.

5. and a possible range of mineral grain dimensions in a deposit.

ACKNOWLEDGEMENTS

I would like to thank the faculty of the Geology department at Temple University for my undergraduate learning experience and especially Dr. G. C. Ulmer, R. E. Bischke and D. E. Grandstaff for their recommendations to graduate schools. Last but not least, I would like to acknowledge my wife, Joanne, for all her support during my academic career.

TABLE OF CONTENTS

LIST OF SYMBOLS

a	grain radius
A	Warburg surface impedance at $\omega = 1$
A to M	letter designation for grain radius (a)
A_i	depolarization factor
$\bar{A}$	average Warburg impedance
A_{min}	minimum Warburg impedance
A_{max}	maximum Warburg impedance
b	grain radius (a) plus thin layer thickness (t)
B	equivelent conductance of the clay exchange cation (Na^+)
B_1	coefficient of dipole term in region 1
c	frequency dependence
D	diffusion coefficient
D	coefficient of dipole term exterior to an ellipsoid
ε	dielectric constant
E_0	applied electric field
E	electric field
f	frequency in cycles per second
F	Faraday constant
g_2	electrode impedance function
$i(\alpha,\beta,\gamma)$	semi-major axis parallel to the applied electric field
I_i	definite elliptic integral
j	$\sqrt{-1}$

m	chargeability
M	Archie's law porosity exponent
N	number of spheres
Q_v	effective clay concentration
R, r	radius
R	gas constant
RMS	root mean square error
t	diffuse zone or thin layer thickness
T	temperature
V	Volume fraction
V'	Model 1 volume fraction
V''	Model 2 volume fraction
$\tilde{V}$	biased volume fraction
V_c	volume fraction of cement or "clay"
ω	angular frequency
X_i	form factor
$|z|$	amplitude in ohms
σ	conductivity
σ_2	conductivity of thin layer
σ_m	macroscopic conductivity
σ_s	effective "clay" conductivity
$\bar{\sigma}$	average conductivity
ρ_a	apparent resistivity
ρ_e	electrolyte resistivity

ρ_E	effective resistivity (ρ_1 or ρ_e)
ρ_0	low frequency resistivity asymptote
ρ_1	background resistivity
ρ_3	mineral resistivity
ρ_∞	high frequency resistivity asymptote
ρ^*	complex resistivity
ρ'	real resistivity
ρ''	imaginary resistivity
Ω	ohm
τ	time constant
ϕ	phase angle in milliradians
ϕ_e	porosity
ϕ_1	electric potential in region 1
δ	function of ρ_1, ρ_e, ρ_3, a and g_2

LIST OF FIGURES

xv

LIST OF TABLES

CHAPTER 1

INTRODUCTION

The purpose of this study was to determine the effect on IP
spectra of mineral composition, volume percent, grain size, shape,
particle orientation with respect to the applied electric field,
porosity and electrolyte ion concentration. Beginning with a three
component boundary value problem for a single sphere with a thin
surface layer embedded in some background medium, the electric
potential in the background medium is obtained. The thin layer about
the sphere is given a frequency dependent electrode impedance function
to represent the diffuse zone between the electrolyte and the mineral.
A Maxwell approach is then applied to the dipole term of this electric
potential expression, to account for the net effect of a distribution
of layered spheres. However, due to the background material of rocks
being inhomogeneously composed of electrolyte and nonconductive
silicate minerals, the background medium is incorporated into the
model in two ways, resulting in slightly different models. First the
background medium is considered macroscopically and the conductive
spheres are put into a "wet" rock. Second, the conductive spheres are
dispersed in the electrolyte and then this mixture is inserted into a
nonconducting rock matrix using Archie's law.

Observations from synthetic samples are in agreement with parts
of both models. With an appropriate regrouping of parameters the

models can be put in terms of simple Cole-Cole models.

The spherical models are then compared with the observed IP spectra for a number of synthetic rocks containing granular mineral grains. The electrolyte ion concentration is varied in a single sample to effect changes in the background resistivity (ρ_1) and the Warburg impedance (A). The volume of pyrite is varied in a suite of samples to analyze the effect of volume percent. The grain radius (a) of pyrite is varied, in a suite of samples over three orders of magnitude to assess the effect of grain sizes. Different minerals are used in the synthetic samples to investigate the possibility of mineral discrimination on the basis of the Warburg impedance values. The frequency dependence (c) observed for the synthetic samples is tabulated and compared to the frequency dependence observed in amplitude and phase measurements for two pyrite electrodes separated with electrolyte.

Other models describing complex resistivity have been developed by Waite (1959) and Grissemann (1971). Waite (1959) incorporates a thin film into the Clausius-Mosotti model (Fröhlich, 1949) whose behavior is described by a lossy capacitor. While Waite's model predicts an exponential decay (e.g. c=1.0) for the induced polarization voltage, Scott and West (1965) observe a logarithmic decay. Grissemann (1971) used the same procedure as Waite (1959) but substitutes a Warburg diffusion impedance (e.g. c=0.5) for the thin film. A similar analogy is used in the model described above, however a general electrode impedance function is substituted for the thin layer and the inhomogeneous background medium is handled in a

different manner.

Several authors such as Collett (1959), Scott and West (1965), and Grissemann (1971) have made similar studies on artificial rocks. Collett (1959) constructed artificial rock samples using andesite and various minerals, in which the pyrite grain size, pyrite volume percent, type of electrolyte and ion concentration, temperature, and primary voltage (time domain measurements) were varied. Results were then compared to Waite's model (1959). Scott and West (1965) constructed very low porosity samples containing quartz, pyrite, and cement, with pyrite of varying grain sizes and concentrations. They also relate their results for time domain measurements to the model by Waite (1959). Due to the low porosity and cement, a high degree of membrane polarization in the Scott and West (1965) samples was observed. Grissemann's (1971) artificial samples were composed of quartz, cement, and pyrite. He varies the grain size and volume percent pyrite. Grissemann's (1971) samples appear to be similar to the synthetic samples used in this report. The porosities are greater than those of the Scott and West (1965) samples and exhibit a smaller degree of membrane polarization.

The effect of mineral grain size, volume percent and electrolyte ion concentration observed by the above authors are in agreement with the observations in this report. However, a larger grain size and volume fraction range is considered here. While Collett (1959) varies the electrolyte ion concentration (NaCl) over a similar range as in this report, Scott and West (1965) and Grissemann (1971) used only one electrolyte ion concentration. Collett (1959) measured artificial

samples containing various sulfide minerals as in this report, while Scott and West (1965) and Grissemann (1971) worked only with pyrite. Collett (1959) and Scott and West (1965) measure in the time domain which results in a limited frequency window of around two to three orders of magnitude in frequency (e.g. 0.1 to 100 hz). Collett (1959) also measures in the frequency domain, as does Grissemann (1971), over about four orders of magnitude in frequency (e.g. 10^0 to 10^4 hz). In this report seven orders of magnitude in frequency are measured (i.e. 10^{-2} to 10^5 hz), due to the effect of grain size, background resistivity, and mineral Warburg impedance which can shift the IP spectra over the frequency range.

While Grissemann (1971) observes an increasing chargeability with decreasing mineral grain size (at constant volume percents), Collett (1959) and Scott and West (1965) do not. A similar trend as observed by Grissemann (1971) is noted in this report, however only for the smallest grain sizes of pyrite. While Grissemann attributes this to increased mineral surface area, this report suggests that sample inhomogeneities with respect to the mineral distribution is responsible. As the mineral grain size gets smaller than the quartz sand, minerals can collect into interstitial spaces. This can result in particle field interactions, which the Clausius-Mosotti model does not consider, creating larger dipole moments than if the particles were far apart. Collett (1959) and Scott and West (1965) seem to have avoided this problem by using similar grain sizes of ore minerals and background minerals.

To account for the effect of particle shape a similar theoretical

development for layered ellipsoids is compared to various mixing formulas of Fricke (1953), which have been extended to include the diffuse zone between the electrolyte and ellipsoids. These results are compared to the observed IP data for synthetic rocks containing copper wire cut into various length to width ratios. Due to the number of unresolvable parameters in the ellipsoidal model, the feasibility of a spherical model approximation is investigated using the copper wire samples. Indications are that a spherical model can be useful in distinguishing nonspherical sample conditions.

In order to relate the results obtained from the synthetic rock measurements to _in situ_ IP field data, two core samples and _in situ_ IP data from disseminated type sulfide deposits are analyzed via the theoretical models.

CHAPTER 2

THEORETICAL DEVELOPMENT

2.1 Spherical Particles

Figure 2.1 shows a model for a single sphere of conductivity with a thin surface layer (σ_2), embedded in some background medium (σ_1). These three regions represent respectively the sulfide particle, the diffuse zone between the particle and the electrolyte, and the medium surrounding the particle which in some cases might be the rock matrix with electrolyte filled pore passages. In relating this model to rock sample measurements, using low current densities, several assumptions are made.

1. Conductivity is a complex function of frequency.

2. Displacement currents are negligable.

3. All media are linearly conductive, isotropic, homogeneous and have electrical properties which are independent of time, temperature and pressure over the measurement time scale.

4. The background medium is frequency independent.

Provided assumptions 1, 2, and 3, the current density is related to the electric field by the constitutive relation

$$J = \sigma^* E e^{j\omega t}.$$

$(2-1)$

Figure 2.1 Theoretical model of a conducting sphere with a thin surface layer in a uniform alternating electic field $E_0 e^{i\omega t}$.

THEORETICAL
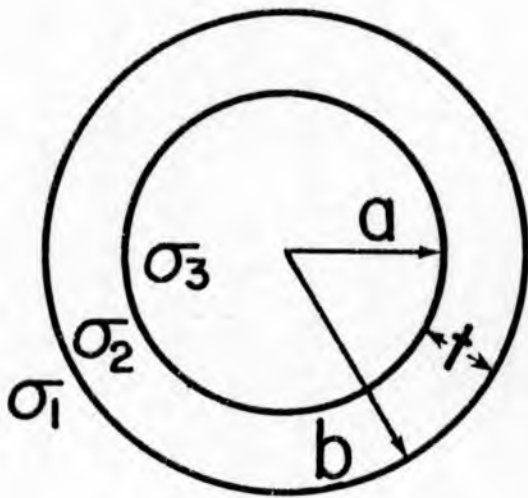
$$\sigma_1$$
$$\sigma_2$$

$$\sigma_3$$

$$b =$$

MODEL

⇢ BACKGROUND
⇢ THIN SURFACE
       LAYER
⇢ SPHERE

a + t

Solving this three component boundary value problem by applying the conditions of continuous electric potential and normal current densities at the boundaries, the electric potential (refer to appendix 1, equation A-17) in region 1 becomes

$$\phi_1 = -E_o \, r \, \cos \theta + \frac{a^3 \left[1 - \left(\frac{\sigma_1}{\sigma_3} + \frac{\sigma_1 t}{\sigma_2 a} \right) \right]}{r^2 \left[1 + 2 \left(\frac{\sigma_1}{\sigma_3} + \frac{\sigma_1 t}{\sigma_2 a} \right) \right]} E_o \, \cos \theta, \quad (2\text{-}2)$$

$\qquad\qquad$ Source $\qquad\qquad\qquad$ Dipole

with the approximation

$$\frac{t}{a} = \frac{t}{b} \ll 1. \tag{2-3}$$

The thickness (t) of the diffuse zone is estimated in the synthetic samples to range between $10^{-10} - 10^{-8}$ meters, while the mineral (e.g. pyrite) grain radii range between $10^{-2} - 10^{-5}$ meters. Assuming the synthetic samples are representative of natural mineralized environments, equation (2-3) then appears satisfied. As noted equation (2-2) contains a source and dipole term, where the magnitude of the dipole moment depends on the conductivity of the three regions, the radius (a) of the sphere, the thickness (t) of the thin surface layer, and is a measure of the charge separation product.

Current entering conductive minerals in rocks must generally pass an electrolyte-electrode type interface. To account for such behavior in the dipole term, the admittance of the thin layer per unit area

(σ_2/t) is equated to an electrode admittance function, g_2. Here t represents the width of the diffuse zone of unbalanced positive and negative ion concentrations on the electrolyte side of the interface. The charge separation within this zone results from an induced electric field produced by a net charge of fixed ions or molecules on the electrode (Grahame, 1947). Madden and Marshall (1959) derive several frequency dependent electrode admittance functions based on equations of ion motion (Mac Donald, 1953) and chemical reaction theory at the electrode (Grahame, 1952). For example the simplest model is a Warburg diffusion admittance having the square root of frequency dependence

$$g_2 = \frac{F^2}{RT} \; C\sqrt{j\omega D} = \frac{\sqrt{j\omega}}{A} \; , \qquad\qquad (2\text{-}4)$$

where

> F = Faradays' constant
>
> R = Gas constant
>
> T = Temperature
>
> C = Concentration of reacting ion
>
> D = Diffusion coefficient
>
> A = Warburg surface impedance at $\omega = 1$ ($\Omega\,m^2$)
>
> ω = radial frequency
>
> $j = \sqrt{-1}$.

Given any electrode admittance function in the general form

$$g_2 = \frac{\sigma_2}{t} = \frac{(j\omega)^C}{A} \; , \qquad\qquad (2\text{-}5)$$

then at low frequencies the diffuse layer will act more like an insulator about the conductive sphere, while at higher frequencies its conductivity will increase allowing more current to be channeled through the sphere. The dipole term in equation (2-2) expresses this frequency dependent behavior very nicely in that as

$$\omega \to 0, \ g_2 \to 0,$$

and the dipole moment reduces to

$$-\frac{a^3}{2} \ E_0 4\pi\epsilon. \tag{2-6}$$

This has the form of a resistive dipole moment, being oriented anti-parallel to the applied electric field, and shows only a cube of the spherical radius dependence on its magnitude. As

$$\omega \to \infty, \ g_2 \to \infty,$$

and the dipole moment reduces to

$$a^3 \left(\frac{\sigma_3 - \sigma_1}{\sigma_3 + 2\sigma_1} \right) E_0 4\pi\epsilon. \tag{2-7}$$

For σ_3 greater than σ_1 this positive high frequency dipole moment is aligned parallel to the applied electric field so that it adds to the total potential in region 1. The dipole magnitude now depends not only on the cube of the spherical radius but also on the conductivity contrast between the sphere and background medium. For large

conductivity contrasts (i.e. $\frac{\sigma_i}{\sigma_1} \geqslant 10^2$) the conductivity function in equation (2-7) saturates toward unity, leaving any change in the dipole magnitude again depending only on the cube of the spherical radius.

Since small conductivity contrasts can greatly decrease the magnitude of the dipole moment it is important to consider what is the effective background conductivity in rocks. Mineralized rocks have an inhomogeneous background material composed essentially of nonconducting silicates and a conducting electrolyte. While the background conductivity might be modeled as some macroscopic conductivity ($\sigma_1 = \sigma_m$) resulting from the geometric distribution of silicates and electrolyte, on the microscopic level the electrolyte is in actual electrical contact with the ore minerals. In natural environments electrolyte conductivity can be similar to those of some of the semiconducting ore minerals and therefore (microscopically speaking) small conductivity contrasts may indeed exist. In anticipation of this, two approaches are suggested resulting in slightly different models. First the background medium is considered macroscopically and the conductive particles are put into a "wet" rock. Second, the conductive particles are dispersed in the electrolyte and then this complex is inserted into a nonconducting rock matrix.

2.2 Model 1

Model 1 disperses the conductive particles in a rock and assumes that the background rock medium can be treated as an electrically

homogeneous region (1) with some average resistivity,ρ_1. The macroscopic resistivity (ρm) of a mixture of resistive particles dispersed in an electrolyte has been investigated by many authors. Shuey (1975) gives an excellent discussion on heterogeneous systems with various mixing formulas and indicates that, to a first order approximation, the macroscopic resistivity is equivalent to the average resistivity. Specifically Shuey (1975) gives an equation originally derived by Bruggman, which when the conductivity of the dispersed phase (here silicates) is zero, reduces to

$$\rho_m = \rho_e \left(1 - V_{silicates}\right)^{-M} \tag{2-8}$$

where

$M = 1.5$

ρ_e = resistivity of electrolyte

$V_{silicates}$ = volume fraction silicates

$1 - V_{silicates} = \emptyset_e$ = rock porosity.

Shuey (1975) also notes that equation (2-8) is quite similar to Archie's empirical law for which M is found to vary between 1.3 and 2.0 for consolidated sandstone (Archie, 1942).

In order to place the conductive spherical particles into the "wet" rock matrix, the dipole term in equation (2-2) must be transformed into an expression which holds for a distribution of non-interacting spheres. Maxwell's approach, figure 2.2, for determining the net effect of a distribution of particles is to equate

the sum of the fields produced by the individual spheres to the field produced by a homogeneous region of average conductivity $\bar{\sigma}$. In other words, if the region containing the mixture of particles and matrix is removed and replaced by a homogeneous medium of conductivity $\bar{\sigma}$, then the fields exterior to the region will be unaltered. By equating the expressions shown in figure 2.2 and substituting

$$\rho_1 = \frac{1}{\sigma_1} = \rho_m, \qquad\qquad\qquad (2\text{-}9)$$

$$V' = \frac{Na^3}{R'^3} = \frac{\text{Volume of conductive spheres}}{\text{Total rock volume}} \quad , \qquad (2\text{-}10)$$
$$\text{(ore, silicates, and electrolyte)}$$

the following equation for the complex resistivity of the rock is derived

$$\rho_{R'}^* = \bar{\rho}_R = \rho_1 \frac{[2 + V' + (1-V')\delta'^{-1}]}{[2(1-V') + (1+2V')\delta'^{-1}]} \quad , \qquad (2\text{-}11)$$

where

$$\delta' = \left(\frac{\rho_3}{\rho_1} + \frac{1}{g_2\rho_1 a} \right) . \qquad\qquad (2\text{-}12)$$

and ρ_1 equals the resistivity of the (rock) background medium.

2.3 Model 2

Model 2 assumes that the microscopic conditions have a greater

Figure 2.2 Maxwell's approach for determining the net effect of a distribution of particles by equating the sum of the fields produced by the individual spheres to the field produced by a homogeneous region of average conductivity $\bar{\sigma}$.

MAXWELL

MICRO
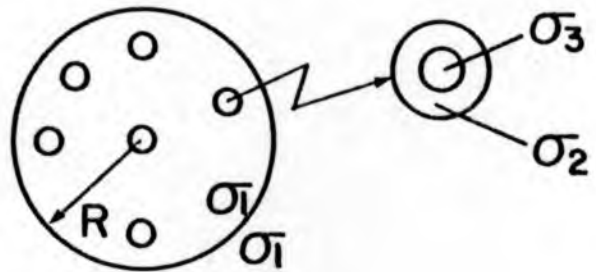
$$\sum_{i=1}^{N} \phi_{d_i} = N \frac{(1-\delta)a^3}{(1+2\delta)r^2} E_0 \cos\theta$$

WHERE: $\quad \delta = \dfrac{\sigma_1}{\sigma_3}\left(1 + \dfrac{\sigma_3}{\sigma_2}\dfrac{t}{a}\right)$

APPROACH

MACRO
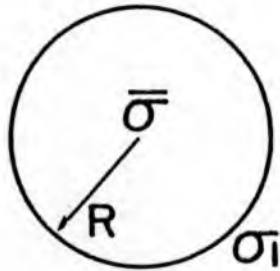
$$\phi_{\text{DIPOLE}} = \frac{(\bar{\sigma} - \sigma_1) R^3}{(\bar{\sigma} + 2\sigma_1) r^2} E_0 \cos\theta$$

$$= \frac{\sigma_1}{\sigma_3}\left(1 + \frac{\sigma_3}{g_2 a}\right)$$

influence on the magnitude of the dipole moment and therefore the conductive particles are first dispersed in an electrolyte. Using a similar Maxwell approach as in Model 1, although here

$$\rho_e = \frac{1}{\sigma_\epsilon} \equiv \frac{1}{\sigma_1} \tag{2-13}$$

an equation for the complex resistivity of the electrolyte and conductive particles becomes

$$\rho_e^* = \bar{\rho}_e = \rho_e \frac{\left[2 + V'' + (1-V'')\ \delta''^{-1}\right]}{\left[2(1-V'') + (1+V'')\ \delta''^{-1}\right]} \quad , \tag{2-14}$$

where

$$\delta'' = \left(\frac{\rho 3}{\rho_e} + \frac{1}{g_2\ \rho_e\ a}\right) \quad , \tag{2-15}$$

$$V'' \ (\neq V') = \frac{Na^3}{R''^3} = \frac{\text{Volume of conductive spheres}}{\text{Volume of spheres and electrolyte}} \tag{2-16}$$

Equation (2-14) is then inserted into a nonconducting rock matrix via some mixing formula such as equation (2-8). For example

$$\rho_{R''}^* = \bar{\rho}_e\ (1 - V_{silicates})^{-M} \tag{2-17}$$

where

$$(V' + \phi_e) + V_{silicates} = 1. \tag{2-18}$$

Therefore the equation for complex resistivity of the rock becomes

$$\rho^*_{R''} = \rho_e(V' + \phi_e)^{-M} \frac{[2+V'' + (1-V'')\ \delta''^{-1}]}{[2(1-V'') + (1+2V'')\ \delta''^{-1}]} \quad , \tag{2-19}$$

where δ'' is given by equation (2-15). Note the similarities in form of the two rock models given by equations (2-11) and (2-19), and that the form is identical to the Clausius-Mosotti relation of dielectric theory (Fröhlich, 1949). For low volume fractions of dispersed conductive particles let

$$\rho_1 = \rho_e(\phi_e)^{-M} \approx \rho_e\ (V'+\phi_e)^{-M}. \tag{2-20}$$

Also note that V' of equation (2-10) and V'' of equation (2-16) are not equal.

2.4 Model Summary

In summary, two models for complex resistivity have been derived. The first model assumes that the inhomogeneous background material can be treated as a homogeneous region resulting in the six parameter model

$$\rho^*_{R'} = \rho_1 \left[\frac{2 + V' + \left[1-V' + \frac{\rho_3}{\rho_1}(2+V')\right] \frac{\rho_1 a(j\omega)^c}{A}}{2(1-V') + \left[1 + 2V' + \frac{2\rho_3}{\rho_1}(1-V')\right] \frac{\rho_1 a(j\omega)^e}{A}} \right] \quad , \tag{2-21}$$

where ρ_1 is given by equation (2-8). The second model assumes that the electrolyte is the effective background material, producing the seven parameter model

$$\rho_{R''}^{*} = \rho_1 \left[\frac{2 + V'' + \left[1-V'' + \frac{\rho_3}{\rho_e}(2+V'')\right] \dfrac{\rho_1 a(j\omega)^c}{A\phi_e^{-M}}}{2(1-V'') + \left[1 + 2V'' + \frac{\rho_3}{\rho_e}(1-V'')\right] \dfrac{2\rho_1 a(j\omega)^c}{A\phi_e^{-M}}} \right] \quad , \qquad (2-22)$$

where ρ_1 is approximated by equation (2-20). Note that due to putting ρ_e in terms of ρ_1 in equation (2-15) for δ " (e.g. $\rho_e \approx \rho_1 \phi^M$), ϕ^{-M} becomes incorporated into equation (2-22). Although equations (2-21) and (2-22) are similar, if all the parameters are known and the forward problem calculated at various frequencies different IP spectra would result. However both models have been presented because data from the synthetic rock samples indicate that a better model lies somewhere between the two.

2.5 Equivalent Cole-Cole Model

The equivalence between the two models and a Cole-Cole model is presented here because their effects are better known in the literature and more often used in the analysis of in-situ field and laboratory rock measurements (Pelton et al., 1978). A Cole-Cole model is completely described by the four independent parameters ρ_0, m, τ, and c, whose effects are illustrated in figure 2.3 (Pelton et al., 1978). ρ_0 is the low frequency amplitude asymptote which shifts the amplitude curve up and down relative to the amplitude axis. The time constant (τ) refers to the dominant relaxation time and controls the peak phase angle position along the frequency axis. Changes in τ only shifts the amplitude and phase angle curves relative to the frequency axis. The chargeability (m) is a measure of the asymptotic amplitude
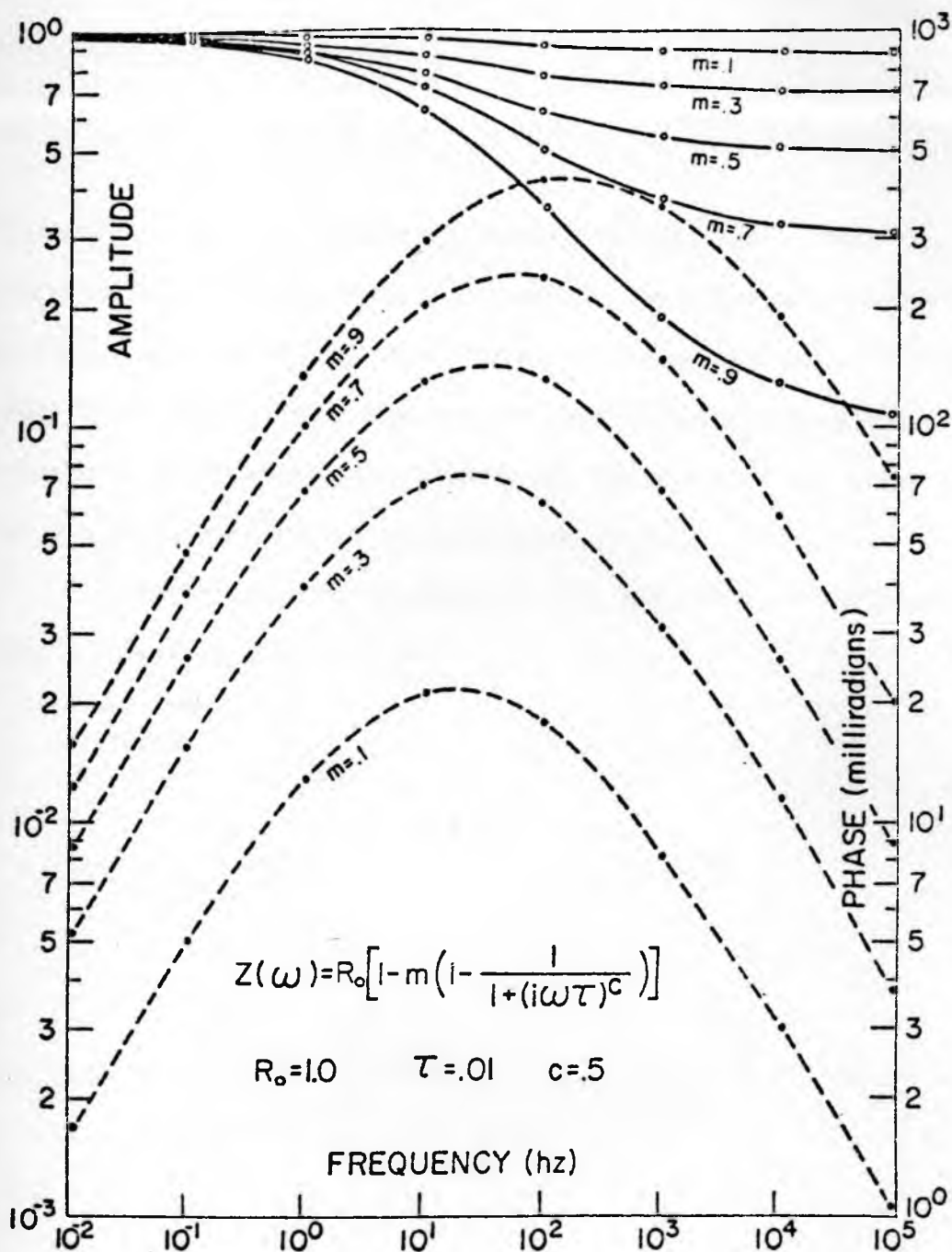
Figure 2.3 Amplitude and phase curves for a Cole-Cole relaxation
model with R=1.0, c=0.5, and m varying from 0.1 to 0.9
(Pelton et al., 1978).

difference and is defined here as

$$m = \frac{\rho_0 - \rho_\infty}{\rho_0}$$
(2-23)

where ρ_∞ is the high frequency asymptotic amplitude. The chargeability (m) only affects changes in the asymptotic resistivity amplitude and the magnitude of the phase angle response. In double logarithmic space, c is the low and high frequency phase angle asymptotic slope whose value determines the width of the dispersion. For a pure Warburg frequency dependence, c=0.5.

The models given by equations (2-21) and 2-22) can be rearranged into a Cole-Cole model so that

Model 1   Model 2

$$\rho_0(\omega=0) = \rho_1 \frac{2+V'}{2(1-V')} \quad : \quad \rho_1 \frac{2+V''}{2(1-V'')} \quad , \quad (2\text{-}24)$$

$$\rho_\infty(\omega=\infty) = \rho_1 \left[\frac{1-V'+\frac{\rho_3}{\rho_1}(2+V')}{1+2V'+\frac{2\rho_3}{\rho_1}(1-V')} \right] \quad : \quad \rho_1 \left[\frac{1-V''+\frac{\rho_3}{\rho_e}(2+V'')}{1+2V''+\frac{2\rho_3}{\rho_e}(1-V'')} \right] , \quad (2\text{-}25)$$

$$m = 1 - \left[\frac{\frac{1-V'}{2+V'}+\frac{\rho_3}{\rho_1}}{\frac{1+2V'}{2(1-V')}+\frac{\rho_3}{\rho_1}} \right] \quad : \quad 1 - \left[\frac{\frac{1-V''}{2+V''}+\frac{\rho_3}{\rho_e}}{\frac{1+2V''}{2(1-V'')}+\frac{\rho_3}{\rho_e}} \right] , \quad (2\text{-}26)$$

$$\tau = \left[\left(\frac{1+2V'}{2(1-V')} + \frac{\rho_3}{\rho_1} \right) \frac{\rho_1 a}{A} \right]^{1/c} \quad : \quad \left[\left(\frac{1 + 2V''}{2(1-V'')} + \frac{\rho_3}{\rho_e} \right) \frac{\rho_1 a}{A\phi^{-M}} \right]^{1/c} , \quad (2\text{-}27)$$

$$\pm c = \qquad\qquad\qquad\qquad \pm c. \qquad\qquad\qquad\qquad (2\text{-}28)$$

Note the dependence of the high frequency resistivity asymptote (ρ_∞), m, and τ on the resistivity ratios between an effective background medium and the conductive particles. For large resistivity contrast this dependence disappears. ρ_0 shows no such dependence on ρ_3 due to the diffuse layer becoming very resistive at low frequencies.

2.6 Inversion Model

Inversion techniques used to apply Models 1 and 2 to synthetic rock data indicate an apparent inability of the data to resolve more than four parameters (as in the Cole-Cole model). To reduce Model 1 to four independent parameters, the grain radius and the Warburg impedance amplitude are first combined into the quotient parameter, A/a (or for Model 2, $\frac{A\phi_e^{-M}}{a}$). Although it is unfortunate the data can not resolve both A and a independently, knowing one allows calculation of the other. Next the mineral particles are considered to be infinitely conductive (i.e. $\rho_3 = 0$). Theoretically this implies maximum polarization due to a large resistivity contrast between an effective background medium and the mineral particles. Low

resistivity contrasts however can greatly reduce the degree of polarization (or m). In reference to both parts of equations 2-25, 2-26, and 2-27, resistivity ratios greater than zero will introduce bias into the inversion models, primarily by absorbing the error into V' or V" making them biased. Keeping in mind the real possibility of V' or V" (=V, generalized volume fraction in the inversion model) being biased, the inversion model becomes

$$\rho^* = \rho_1 \frac{2+V}{2(1-V)} \left[1 - \frac{9V}{(1+2V)(2+V)} \left(1 - \frac{1}{1+\left(\frac{1+2V}{2(1-V)}\right)\frac{a\rho_1}{A}(j\omega)^c} \right) \right]. \quad (2-29)$$

During the discussions of data observations V' and V" of Models 1 and 2 respectively will be compared to the inversion parameter V. Also a biased volume fraction $\hat{V}$ will be determined on the basis of resistivity contrast considerations involving ρ_3 and ρ_e (or ρ_1) and then compared to the observed inversion parameter V. The equivalent Cole-Cole inversion model parameters are given by

$$\rho_\infty = \rho_1 \frac{1-V}{1+2V} \quad , \quad (2-30)$$

$$\rho_o = \rho_1 \frac{2+V}{2(1-V)} \quad , \quad (2-31)$$

$$m = 1 - \frac{2(1-V)^2}{(1+2V)(2+V)} \quad , \quad (2-32)$$

$$\tau = \left[\frac{1+2V}{2(1-V)} \cdot \frac{\rho_1 a}{A} \right]^{1/c} \quad , \qquad (2\text{-}33)$$

$$c = c \qquad \qquad . \qquad (2\text{-}34)$$

CHAPTER 3

METHODS OF SAMPLE PREPARATION AND DATA ANALYSIS

3.1 Sample Preparation

A number of synthetic rocks containing quartz sand, a low-alkali
Portland cement and various ore minerals were constructed in order to
test the theoretical models.

Control of grain size factors in sample preparation was achieved
by fourteen standard graduated seives covering three decades in
particle size. The ore minerals used included pyrite, chalcopyrite,
graphite, galena, molybdenite and copper metal. The average density
of the ore minerals, quartz sand, and cement was calculated, from
which the final volume fractions (V' and V") in each sample were
determined. Changes in sample background resistivity was achieved
through varying the salt concentration in the electrolyte. Sample
porosity and resulting pore structure was mainly controlled by the
amount of cement and the size of sand grains used.

Some samples, contained in a plastic (Lucite) sleeve were made
under uniaxial pressure to reduce porosity (refer to appendix 2).
They were then saturated in a saline solution for two weeks, to allow
equilibrium between the electrolyte and the samples' contents to be
reached.

The samples were then measured with a four electrode arrangement
over the frequency range of 10^{-2} to 10^5 hertz. The measurements were

made using two sets of equipment, a Kennecott digital receiver and tape recorder for the lowest frequencies (10^{-2}hz to 5 hz) and a phase sensitive synchronized detector (Princeton Applied Research PAR lock in amplifier) for the higher frequencies (5hz to 10^{5}hz). At the 5hz overlap (figures 3.1 and 3.2), there was generally good agreement between the two sets of equipment.

3.2 Data Analysis

Figures 3.1 and 3.2 shows typical IP spectra for the synthetic rock samples. Phase angle and complex resistivity have been plotted as a function of frequency. The smooth curves are the theoretical model (equation 2-29) fit to the data via a least squares inversion technique using the Marquardt algorithm (Marquardt, 1963). The parameters τ, A/a, V and c were generally well resolved, when the phase angle peak was observed, and fits to the data had 5-10% RMS error.

The phase angle curves typically show sharp peaks and slopes near 0.5, indicating a simple Warburg frequency dependence. The small increase in phase angle at the higher end of the measured frequency range is probably due to polarization effects in the cement matrix. Measurements performed on samples containing various combinations of sand, cement and electrolyte, making up the background medium, only showed appreciable polarization when cement was present, (figure 3.3). As the resistance of these cement samples increased, so did the amount of polarization and it is therfore concluded that membrane polarization caused by the cement particles is responsible for the

Figure 3.1   Inversion of complex resistivity specta obtained from measurements of a synthetic sample containing pyrite, quartz sand, and cement in 1 Ωm electrolyte (NaCl).

SAMPLE:
PYRITE (G)
$a = .175 - .295$ mm
$v' = .085, v'' = .16$
$\tilde{v} = .06$

DATA:
● OBSERVED PHASE ANGLE
△ OBSERVED COMPLEX RESISTIVITY
— SPHERICAL MODEL
$\rho_1 = 28.3 \pm .67 \ \Omega$-m
$A/a = 1076 \pm 108 \ \Omega$-m
$V = .093 \pm .34$
$C = .524 \pm .014$
RMS = .11

$|\rho*| (\Omega$-m)

FREQUENCY (HERTZ)

(MILLIRADIANS)

PHASE ANGLE

Figure 3.2   Inversion of complex resistivity spectra obtained from measurements of a synthetic sample containing chalcopyrite, quartz sand, and cement in 1Ω m electrolyte (NaCl).

DATA:
- ● OBSERVED PHASE ANGLE
- △ OBSERVED COMPLEX RESISTIVITY
- — SPHERICAL MODEL

ρ_i = 14.2 ± .32 Ω-m

A/a = 568 ± 48 Ω-m

V = .127 ± .005

C = .671 ± .013

RMS = .049

SAMPLE:

CHALCOPYRITE (I)

a = .584-1.00 mm

v' = .088, v" = .16

FREQUENCY (HERTZ)

$|\rho^*|(\Omega$-m)

PHASE ANGLE (MILLIRADIANS)
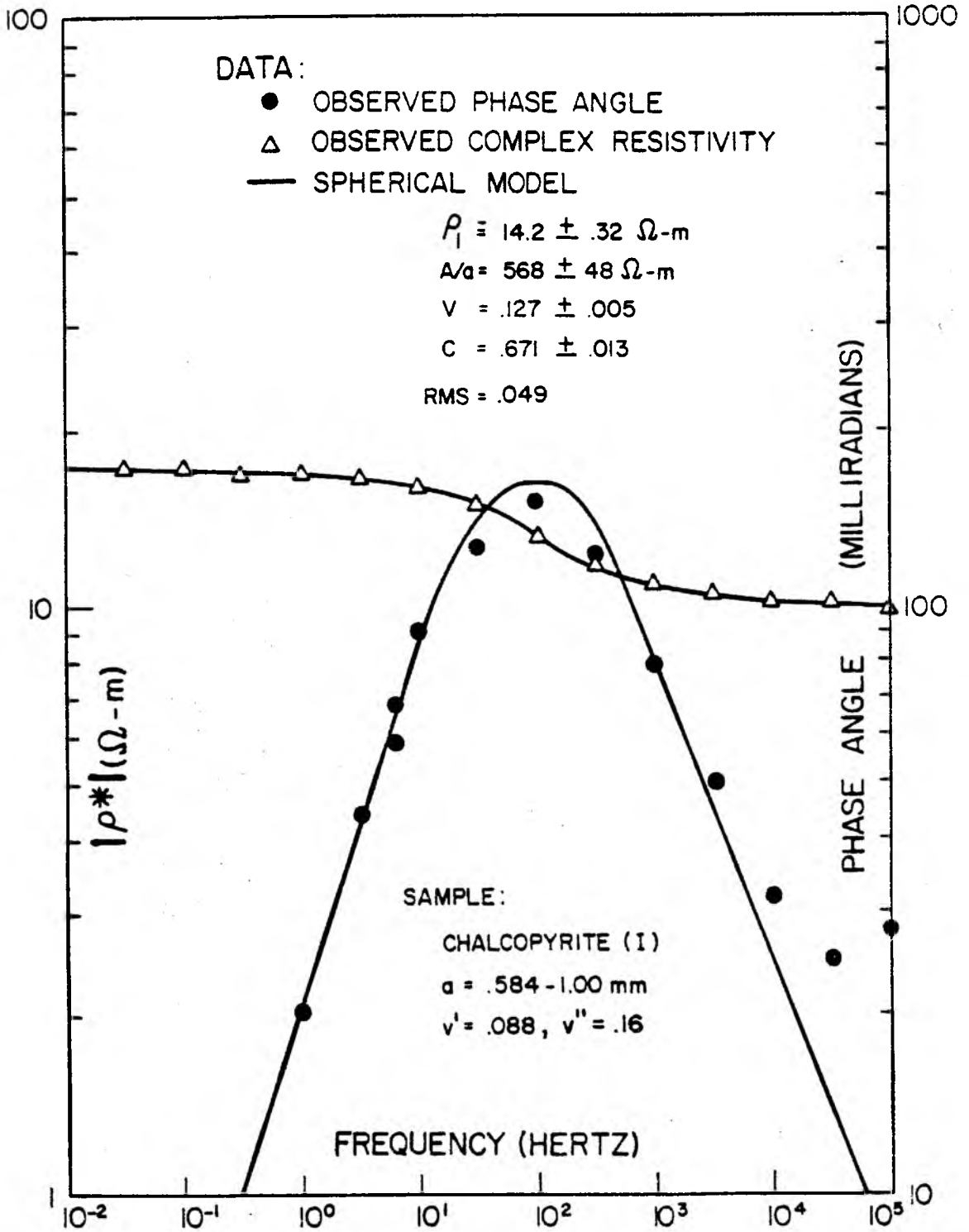
Figure 3.3 Phase angle spectra obtained from samples containing various combinations of quartz sand, cement, and 1Ωm electrolyte (NaCl) making up the background medium. Appreciable membrane polarization is observed when cement is present.

Legend:
● CEMENT, SAND AND ELECTROLYTE, $|\rho^*_{lhz}| = 25\ \Omega$-m.
□ CEMENT, SAND AND ELECTROLYTE, $|\rho^*_{lhz}| = 73\ \Omega$-m.
△ CEMENT, AND ELECTROLYTE, $|\rho^*_{lhz}| = 26\ \Omega$-m.
○ ELECTROLYTE, $|\rho^*_{lhz}| = .76\ \Omega$-m.
ELECTROLYTE AND SAND, $|\rho^*_{lhz}| = 3.2\ \Omega$-m, (NO OBSERVABLE PHASE ANGLE).

Y-axis: PHASE ANGLE (MILLIRADIANS)
X-axis: FREQUENCY (HERTZ)
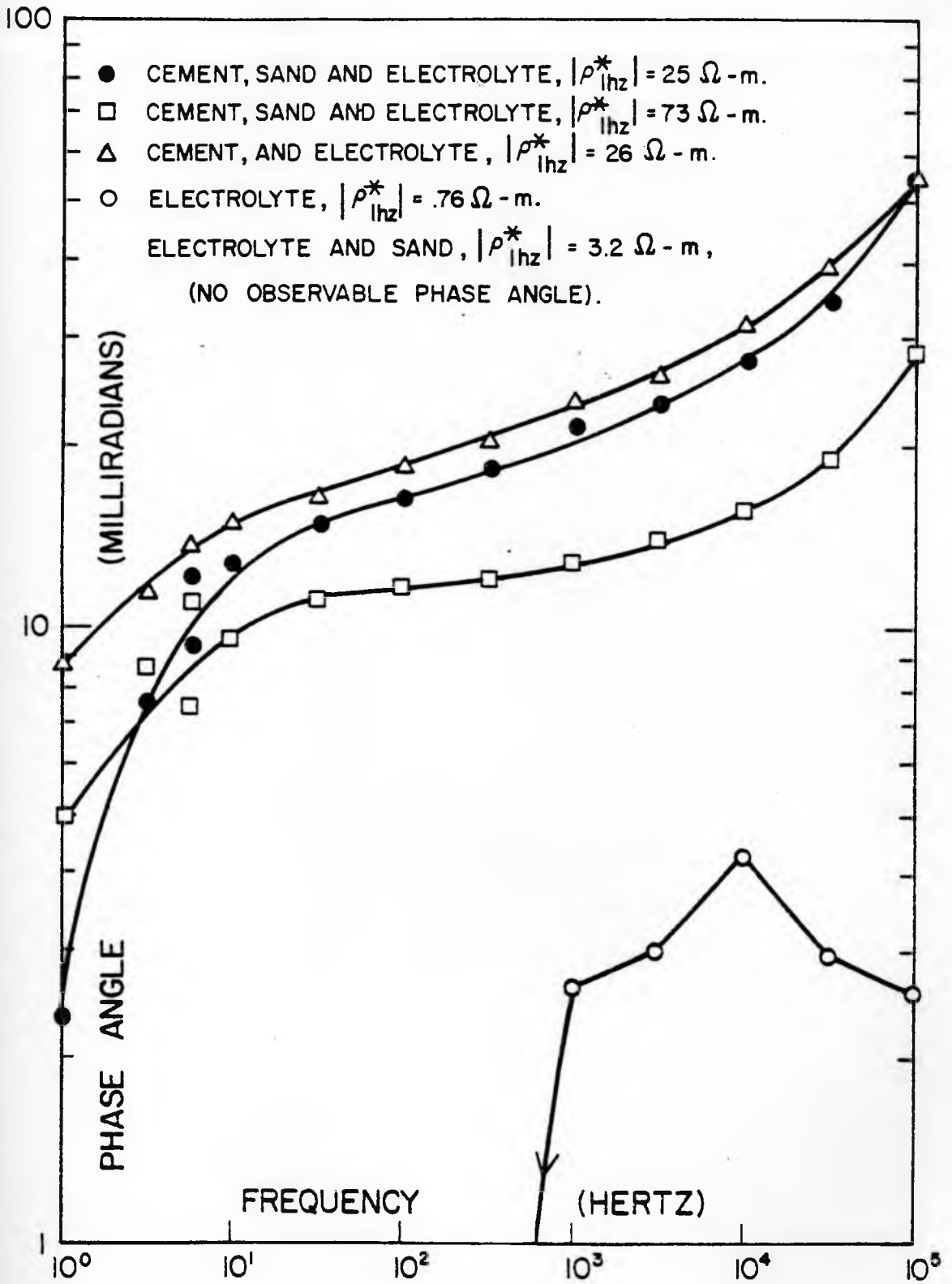
high frequency polarization.

Due to the dependence of membrane polarization on background resistivity and the resulting asymmetric nature of the phase angle curve, its effect was minimized during the inversion process generally by eliminating some of the high frequency data points, which contained the greatest contributions from membrane polarization.

CHAPTER 4

SYNTHETIC ROCK OBSERVATIONS AND RESULTS

4.1 Background Resistivity

Figure 4.1 (right hand side) shows the observed data (H-1 to H-5), in the form of amplitude and phase as a function of frequency. The data for H-1 to H-5 was obtained from one synthetic sample by changes in eletrolyte concentration. Note the general decrease in $|\rho|$ as the electrolyte concentration increases from H-1 to H-5. The background resistivity ρ_1 varies in a similar fashion (table 4.1). This sample has a porosity of .38, contains the grain size fraction H (a = .30-.58mm) of both quartz sand and pyrite (V'=.085, V"=.16), and is constructed with no cementing agent. Note the lack of the high frequency phase increase generally observed when cement is present.

Increases in the electrolyte concentration is observed to decrease the amplitude of the complex resistivity and shift the dispersive region to higher frequencies. Note the similar trend in the theoretical model as ρ_1 is decreased (figure 4.1, left hand side). ρ_1 is a function of the electrolyte resistivity (equation 2-20) and therefore it has a strong effect on the time constant (τ) of the Cole-Cole model (equation 2-33). Decreases in the electrolyte concentration (e.g. H-5 to H-1) is observed to increase the peak phase amplitude to an apparent maximum. This particular trend is not predicted by the model (figure 4.1). A measure of the asymptotic

Figure 4.1 Effect of background resistivity ($\rho_1 = \rho_{I,II,III}$) on the theoretical model (equation 2-29) and the observed IP spectra obtained from one synthetic sample by changes in the electrolyte concentration. The synthetic sample contains quartz sand, pyrite, and no cement, and has a porosity of ϕ_e = .38. For sample statistics and inversion results of the observed data H-1 to H-5 refer to table 4.1.

EFFECT OF BACKGROUND RESISTIVITY
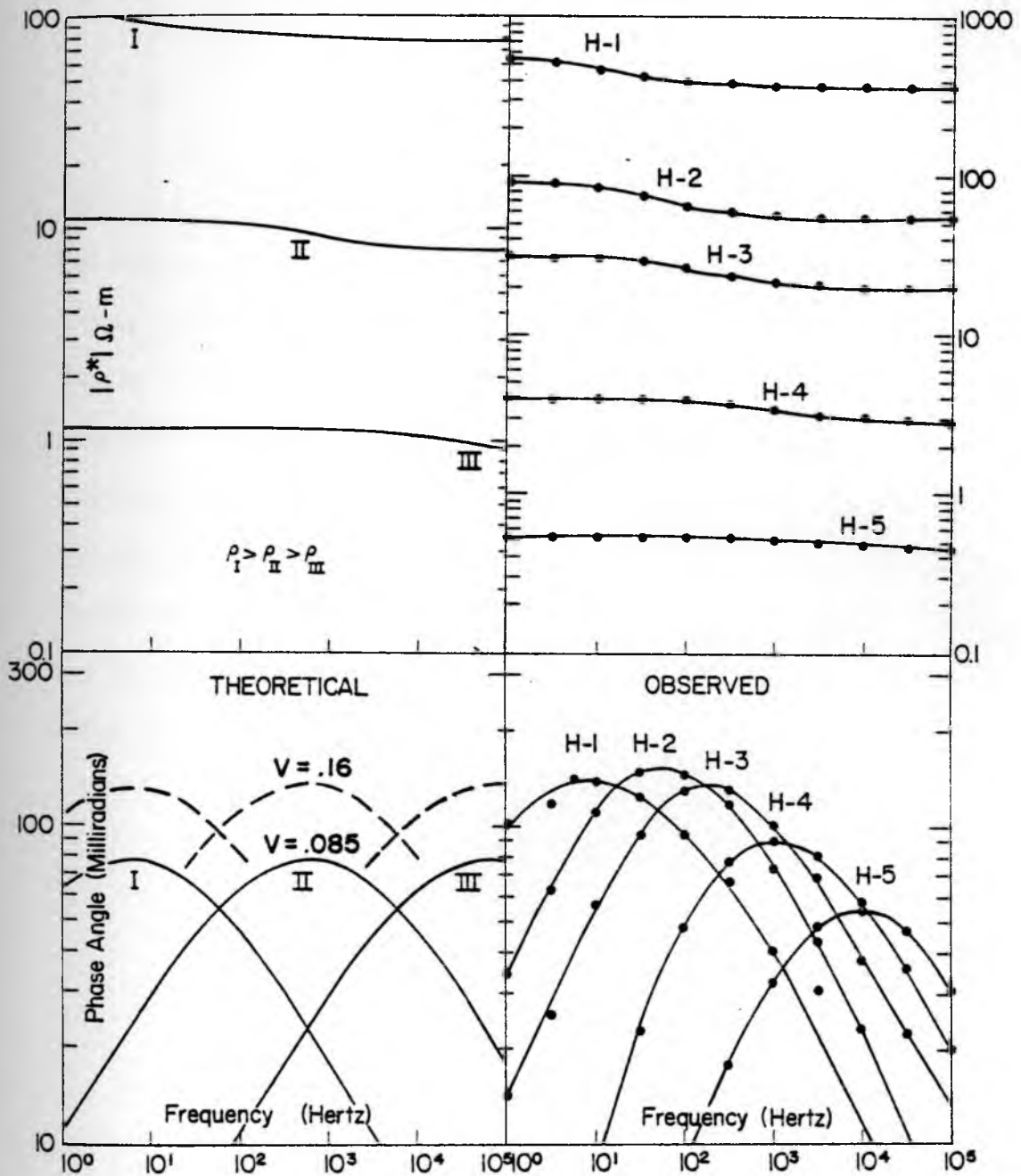
Table 4.1 Sample statistics and inversion results for electrolyte variations in synthetic samples. The observed IP spectra for sample H-1 to H-5 and G-1 are shown in figures 4.1 and 3.1 (G) respectively. Sample H-1 to H-5 contains pyrite of V' = .085, V" = .16. The predicted volume fraction $\tilde{V}$ is an estimate of the expected bias in the observed inversion parameter V, due to a finite resistivity contrast between the electrolyte and pyrite (refer to page 47). The Warburg impedance (A) is obtained by multiplying the observed grain radius (a) by the inversion parameter A/a. Letter grain radii are listed in table 4.3.

SAMPLE	ELECTROLYTE	ELECT. RESIST. ρ_e Ω-m	PREDICT VOL. FRACT. $\bar{v}$	INVERTED PARAMETERS ρ_i Ω-m	V	C	A/a Ω-m	TIME CONSTANT τ (sec.)	$\bar{A}$ Ω-m^2
H-1	DISTILLED H$_2$O DEIONIZED	308	.16	525	.159	.469	1927	3.72×10^{-2}	.848
H-2	DISTILLED H$_2$O	33	.15	77.5	.136	.594	1436	4.37×10^{-3}	.632
H-3	.01 M NaCl	10	.13	26.4	.118	.590	1088	1.01×10^{-3}	.479
H-4	0.1 M NaCl	1.0	.06	3.51	.077	.628	524	1.63×10^{-4}	.231
H-5	1.0 M NaCl	0.1	.01	.494	.046	.628	253	1.99×10^{-5}	.111
G-1	0.1M NaCl	1.0	.06	28.3	.093	.524	1076	4.11×10^{-4}	.253
G-2	AGED ONE YEAR	2.3	.09	63.3	.105	.474	1094	9.53×10^{-4}	.257

resistivity difference normalized by ρ_0 is the chargeability (m) of the Cole-Cole model. Theoretically m (equation 2-26) depends only on the resistivity ratio ρ_3/ρ_e (or ρ_3/ρ_1) and the volume fraction V" (or V'). The inversion model however does assume $\rho_3 = 0$, leaving only a volume fraction dependence as given in equation (2-32). Since the electrolyte resistivity (ρ_e) is changing in samples H-1 to H-5, the trend observed in the maximum phase amplitude may be indicating that nonnegligible resistivity ratios (ρ_3/ρ_e) are responsible for producing the trend.

Inversion parameters for the observed data shown in figure 4.1 are listed in table 4.1 (also G-1 and G-2) and show trends which are in reasonable agreement with Model 1 (equation 2-27) and Model 2 (equations 2-24, 2-25, and 2-26). For example as ρ_e decreases, the background resistivity (ρ_1) decreases proportionally as is in approximate agreement with Archie's law and/or both parts of equation (2-20). A relationship between τ and ρ_1 is given in equation (2-27 or 2-33). Since the radii of the pyrite grains are known, the Warburg impedance $\bar{A}$ ($\omega=1$) can be calculated and is seen in table 4.1 to decrease as the electrolyte concentration increases. From electrolyte-interface impedance measurements on pyrite electrodes a similar decreasing trend in the Warburg impedance as the electrolyte concentration increases is noted by Madden and Marshall (1959) and Klein and Pelton (1976). The actual magnitude of $\bar{A}$ for sample suites H and G are in approximate agreement with their results. For similar NaCl concentrations as in samples H-4 and G-1 (table 4.1), Klein and Pelton (1976) give a Warburg impedance of 1.2 Ωm^2($\omega=1$). In .014N KCl,

Madden and Marshall (1959) give a Warburg impedance of 0.2 $\Omega m^2 (\omega=1)$. Similar electrode measurements conducted over a two week period indicated a range of impedances from 0.1 to 0.6 Ωm^2 (e.g. figure 4.14, at $\omega=1$).

The Warburg impedance $\bar{A}$ obtained through inversion of H-4 and G-1 data are .23 and .25 Ωm^2 (table 4.1) respectively. These values are not only similar for the two different grain sizes of pyrite, but are in reasonable agreement with the independent electrode measurements.

Although discussed in more detail in a later section, note that the frequency dependent parameter (c) decreases as ρ_e increases (table 4.1). This trend is thought to result from the dispersive region shifting to lower frequencies in conjunction with the frequency dependence of the electrode impedance changing its character from a more capacitive nature (c=1.0) to a diffusion controlled (Warburg) behavior (c=.5) over the measured frequency range (figure 4.14). For example, sample H-1 shows a Warburg frequency dependence of c= .47 (table 4.1). This sample has a dispersive region occurring at lower frequencies than say H-2 to H-5, which show greater frequency dependencies.

To analyze the shifting trend of the dispersive region due to changes in ρ_1 and A, equation (2-33) for the time constant is linearized by taking the ln of both sides and rearranging terms so that

$$\ln \frac{\rho_1}{A} = c \ln \tau - \ln \left[\frac{1 + 2V}{2(1-V)} \right] \bar{a} , \qquad (4\text{-}1)$$

where

$$c = \text{slope} ,$$

$$-\ln \frac{1 + 2V}{2(1-V)} \ \bar{a} = y - \text{intercept.} \qquad (4\text{-}2)$$

Note that for low volume fractions the y-intercept is most sensitive grain radius. Equation (4-1) is equivalent to plotting ρ_1/A versus τ in log-log space, which has been done in figure 4.2. As seen the data points (ρ_1/A, τ) from samples H-1 to H-5 show quite a linear relationship for the wide range of values encountered. A linear least squares fit to the H-1 to H-5 data ($\ln^{\rho 1}/A$, $\ln \tau$) produces the observed equation shown in figure 4.2. Note that the observed slope of .66 does not indicate an ideal Warburg frequency dependence (c=.5). However it does lie within the range observed frequency dependency of $c \approx 0.5$ and $c \approx 0.8$ as displayed in figure 4.14 for pyrite electrodes. For Model 1 (V') and Model 2 (V") the theoretical y-intercept (equation 4-2) is calculated to be 8.2 and 8.0 respectively for the given grain size H. These intercept values are too close to be definitive with respect to V' and V" because of their theoretically weak influence on τ. However the observed y-intercept (figure 4.2) is in reasonable agreement with both theoretical values, which indeed suggest a grain size dominance as in equation (4-2). Note that although the inversion parameter V changes by almost a factor of four between samples H-1 and H-5, its effect on the time constant does appear to be quite minor, as indicated by the high degree of linearity observed in figure 4.2. Therefore the observed data ($^{\rho 1}/A$, τ) for samples H-1 to H-5 seems to be in good agreement with the theoretical dependence of the time constant (τ) primarily on changes in the samples' background resistivity ($^{\rho 1}$) and the minerals' Warburg

Figue 4.2   Plot of ρ_1/A versus the time constant (equation 2-33) for the synthetic sample data H-1 to H-5.   Inversion results for the background resistivity (ρ_1), Warburg impedance (A), and the time constant (τ) are listed in table 4.1.

MODEL: $\tau^c = \left[\dfrac{\rho_1}{A}\dfrac{a(1+2v)}{2(1-v)}\right]$

$\bar{a} = 4.4 \times 10^{-4} m$

$v' = .085$

$v'' = .16$

THEORETICAL: $\ln \dfrac{\rho_1}{A} = .5 \ln \tau + 8.2'(8.0'')$

OBSERVED: $\ln \dfrac{\rho_1}{A} = .655 \ln \tau + 8.50$

τ (sec)

$\dfrac{\rho_1}{A}\left(\dfrac{\Omega-m}{\Omega-m^2}\right)$

H-1

H-2

H-3

H-4

H-5
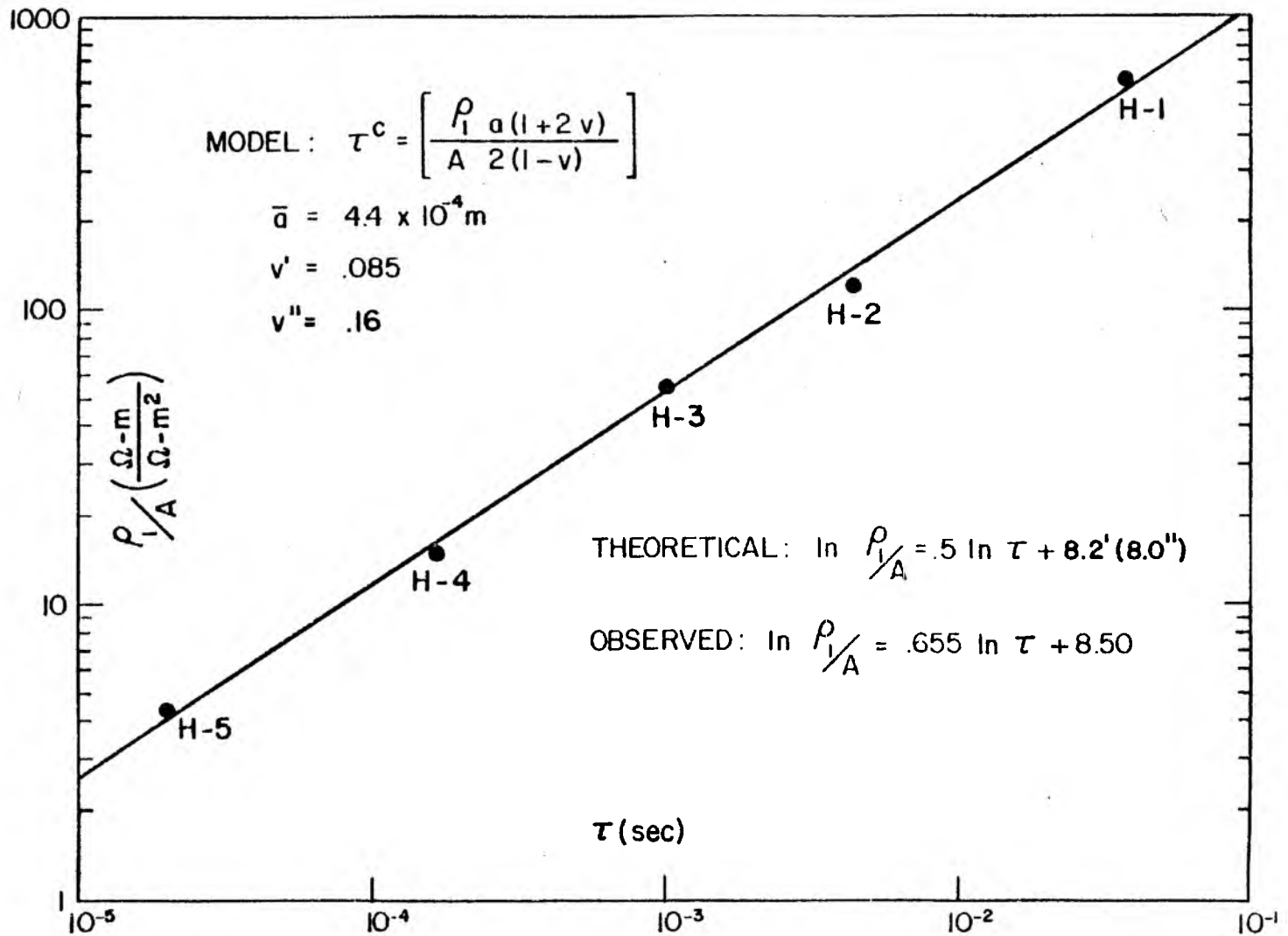
impedance (A), given by equation (2-33) for a given grain radius (a) and some volume fraction (V). The average frequency dependence of $c = .66$ estimated by the combined data (ρ_1/A, τ) in figure 4.2 suggest that on the average the time constant is proportional to $(\frac{\rho_1 a}{A})^{1/.66}$ over the measured frequency range.

The inversion parameter V (table 4.1) for samples H-1 to H-5 increase to an apparent maximum as the electrolyte resistivity is increased. This trend is also reflected in the observed phase data in figure 4.1. An unbiased parameter V, with respect to the inversion model, will be obtained from a sample when ρ_3/ρ_e (or ρ_3/ρ_1 in term of Model 1) can be assumed near zero. In reference to equation(2-7) this approximation is valid for $\rho_3/\rho_\epsilon \leq 10^{-2}$. Some measurements of ρ_3 for the pyrite used in the synthetic samples suggest values around .25-1.0Ω m, which is within the range of 10^5 to 10^0 Ωm reported by Pridmore and Shuey (1975). Noting the electrolyte resistivities given in table 4.1, it is seen that only sample H-1 has a large enough resistivity contrast to fit the criterion (e.g. $\rho_3/\rho_e = 3 \times 10^{-3} \leq 10^{-2}$). This suggests that its inversion parameter V=.16 is unbiased which is in excellent agreement with the observed volume fraction of V" = .16 (Model 2). V" remember is determined by the volume of pyrite relative to the conductors in the rock sample (equation 2-16), while V' (Model 1) is determined by the volume of pyrite in the total rock sample (equation 2-10). In reference to Model 1, near maximum polarization would occur when $\rho_3/\rho_1 \leq 10^{-2}$. Note that for samples H-1 and H-2 (table 4.1) their resistivity ratios ρ_3/ρ_1 ($\rho_3 \approx 1\Omega$ m) meet this criterion. However their inversion parameters V of .16 and .14

respectively are almost twice as large as the calculated V' = .085.
Therefore sample H-1, which fits the criterion of $\rho_3/\rho_e \leq 10^{-2}$ and
shows an excellent agreement between V and V", suggests that the
inversion model parameter V is giving information about V" (equation
2-16).

Another synthetic sample thought to give an unbiased volume
fraction estimate due to low resistivity ratios is sample C1 (table
5.1, figures 5.3 and 5.4), which contains copper wire particles ($\rho_3 = 10^{-7}$
Ω m), cement to reduce the porosity ($\emptyset_e = .16$), and is saturated with
1Ω m electrolyte (NaCl). Since ρ_3/ρ_e is approximately 10^{-7} for sample
C1, inversion of its data (figure 5.3) to the theoretical inversion
model should give unbiased results. Sample C1 gives an inversion
parameter of V=.16 and is calculated to have a V' = .085 and V" = .35,
neither of which is closely approximated by V. While V' (=.085) for
sample H-1 to H-5 and sample C1 are similar, the difference in V"
(=.16, H-1 to H-5; = .35, C1) between these samples is due to the
addition of cement in sample C1. According to equation (2-16) V"
depends on the volume of conductive elements (e.g. ρ_3 ,ρ_e) which
have been placed into a nonconductive rock matrix. Since the cement
minerals are resistive it might be expected that they could be lumped
into the nonconductive silicate group. However, the fine grained
cement particles represent a large surface area within the synthetic
samples. If the surface of the cement particles have a capacity for
cation exchange, then the potential surface conduction along the
cement-electrolyte interface may make the cement appear as a
conductive element in the sample. For example, the equation derived

by Waxman and Smits (1968) used to calculate the effects due to surface conduction in clay bearing sandstones is

$$\sigma_r = \phi_e^{M} (\sigma_e + \sigma_s),$$ (4-3)

$$\sigma_s = BQ_v (mhos/m),$$ (4-4)

where σ_s is the effective clay conductivity. Q_v (units of equiv/liter) is the effective clay concentration. B(units of liter/equiv-ohm-m) represents the equivalent conductance of the clay exchange cation (Na^+) as a function of solution conductivity (σ_e). For σ_e = 1 mho/m and 25°c, B (Waxman and Smits, 1968) is estimated at 1.9 liter/equiv. ohm-m. For sample Cl, where

σ_1 = .05 mhos/m

σ_e = 1.0 mhos/m

ϕ_e = .16

M = 2,

the effective cement conductivity is estimated from equation (4-3) to be 1.0 mho/m, which is equivalent to the electrolyte conductivity (σ_e). For the B value given above Q_v becomes .53 equiv/liter which is comparable to values observed for shaly sandstone (Waxman and Smits, 1968). In terms of the effective clay concentration (q_m), given in terms of meq. per 100 grams where

$$q_m = \frac{100 \, Q_v \phi_e}{V_c \rho_c}$$ (4-5)

and the density of cement (ρ_c) is estimated at 3 gms/cc and the volume

fraction of cement (V_c) is .30, q_m for sample C1 is 9.4 meq/100 gms. This suggests that the cement in C1 has a low to moderate cation exchange capacity and since $\sigma_e \approx \sigma_s$ indications are that the cement can and should be considered as a conductive element. Therefore

$$V'' = \frac{\text{Volume of conductive mineral}}{\text{Volume of conductive mineral, electrolyte, and cement,}}$$

$$= \frac{V'}{V' + \emptyset_e + V_c}, \qquad (4\text{-}6)$$

where V' is given by equation (2-10) and V_c is the volume fraction of cement or clay in the sample. From equation (4-6) then, V'' for samples C1 becomes .16, which is in excellent agreement with its inversion results ($V = .16$). Therefore with respect to samples H-1 and C1 the inversion parameter V appears to be giving unbiased information about V'' of Model 2, as calculated in equation (4-6).

Equations (2-26, Model 2) and (2-32) for the theoretical and inversion model chargeability (m) respectively are used to assess the possible bias, introduced by small resistivity contrasts into the inversion parameter V, obtained from samples suites H and G data (figure 3.1 and 4.1). For example the inversion model returns a V based on the the observed complex resistivity and phase data such that

$$m_{\text{Inversion}} = 1 - \frac{2(1-V)^2}{(1+2V)(2+V)}$$

With respect to the theoretical Model 2,

$$^m\text{Model 2} = 1 - \frac{\frac{1-V''}{2+V''} + \frac{\rho_3}{\rho_e}}{\frac{1+2V''}{2(1-V'')} + \frac{2\rho_3}{\rho_e}} \qquad . \qquad (2-26)$$

Since V" (=.16) is known for sample suites H and G, and ρ_3/ρ_e can be roughly estimated (i.e. Pyrite: $\rho_3 \approx 1\Omega$ m, ρ_e from table 4.1) ^{m}Model 2 can be calculated for the various electrolyte resistivities (or in terms of Model 1, ρ_1). By equating

$$^m\text{Model 2} = {}^m\text{Inversion} (= {}^m\text{observed}), \qquad (4-7)$$

a predicted inversion parameter $\tilde{V}(=V$ in equation 2-32) can be determined which will produce the calculated m in equation (2-26) for Model 2. This will estimate the expected bias in the observed inversion parameter V, due to low resistivity contrast between the electrolyte and pyrite. Estimates of $\tilde{V}$ have been made for sample suites H and G based on V" = .16, ρ_3=1Ω m and ρ_e values in table 4.1. Note that for electrolyte resistivities greater than about 1Ωm (e.g. not H-5) the inversion parameters (V) are comparable to the predicted $\tilde{V}$. Therefore suggesting that V can be approximately related to V" through equations (2-32) and (2-26, Model 2).

Figure 4.3 shows a family of curves for m versus ρ_E (e.g. ρ_e or ρ_1) for V=.16 and various ρ_3 values. The theoretical chargeability expression shown in figure 4.3 is left in general terms to represent both parts of equation (2-26) where ρ_E is some effective background resisitivity. The curves demonstrate that as ρ_E approaches ρ_3, m

Figure 4.3 Plot of chargeability (equation 2-26) versus an effective background resistivity ($\rho_E = \rho_1$, ρ_e) for a constant volume fraction (V = .085, .16). Inversion results for the synthetic sample data H-1 to H-5 and G-1 to G-2 are listed in table 4.1.

$$m = \frac{\rho_o - \rho_\infty}{\rho_o} = 1 - \frac{2(1-v)^2 \left[1 + \frac{\rho_3}{\rho_E}\left(\frac{2+v}{1-v}\right)\right]}{(2+v)(1+2v)\left[1 + \frac{2\rho_3}{\rho_E}\left(\frac{1-v}{1+2v}\right)\right]}$$

V = .16

V = .085

RESISTIVITY

O - H, □ - G
● ■ BACKGROUND - ρ_1, M_{ob}
O □ ELECTROLYTE - ρ_e, M_{ob}

CHARGEABILITY - m

EFFECTIVE BACKGROUND RESISTIVITY $\rho_E(\Omega\text{-m})$

CURVE NUMBER	ρ_3 (Ω-m)
I	0.1
II	.25
III	1.0
IV	10
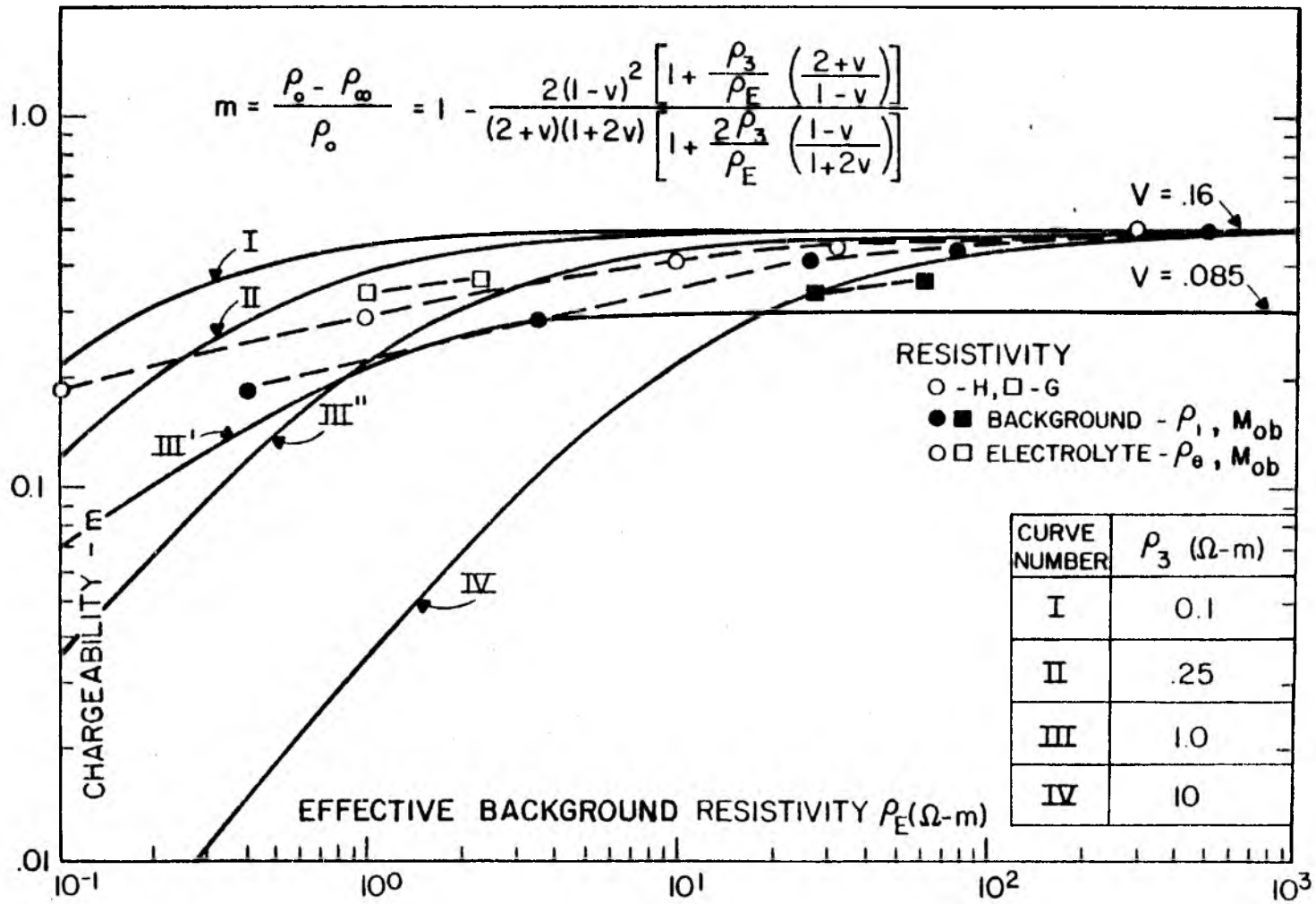
begins to fall off rather sharply for a given volume fraction. For sample suites H and G the observed m has been plotted in figure 4.3 as a function of their respective ρ_e and ρ_1 values as listed in table 4.1. Note that the majority of the open data points (m_{ob}, ρ_e) for sample suites H and G fall between curves II and III" (V=.16), suggesting that the resistivity of pyrite (ρ_3) lies between .25 and 1.0 Ωm. The majority of dark data points (m_{ob}, ρ_1) fall between curves III" and IV, suggesting the resistivity of pyrite lies between 1.0 and 10 Ωm. The former indicated resistivity range for pyrite is in good agreement with the rough estimates given earlier, suggesting that the effective background resistivty (ρ_E) with respect to the chargeability (m) is the electrolyte resistivity (ρ_e).

Sample suite H data points (m_{ob}, ρ_1 and ρ_e) plot close together in figure 4.3 due to a large porosity ($\emptyset_H$ = .38) and tend to fall mostly around curve III". This makes it difficult to distinguish between an effective background resistivity (e.g. ρ_1 or ρ_e) although a strong dependence on V" (=.16) is suggested which implies ρ_e theoretically. Sample suite G however has a much smaller porosity ($\emptyset_G$ = .16) and displays a greater difference between ρ_1 and ρ_e. Note how this samples' (m_{ob}, ρ_e) data points fall between curve II and III" suggesting ρ_{py} lies between .25 and 1.0 Ω m. This is within the range of values observed by Pridmore and Shuey (1975). Its (m_{ob}, ρ_1) data points on the other hand fall on curve IV, suggesting a ρ_{py} of 10Ω m. Values as large as 10 Ωm are at the extreme end of the observed resistivity range for pyrite (Pridmore and Shuey, 1975). If ρ_1 is to be the effective background resistivity as in Model 1 then more (m_{ob},

ρ_1) data points for sample suites H and G might be expected to fall
closer to curve III' in figure 4.3 which is a function of V' = .085.
In fact very few data points (m_{ob}, ρ_1 or ρ_e) are observed to plot
near curve III', which suggests that the inversion results are not
giving information about V'. Since the (m_{ob}, ρ_e) data points of
sample suite G (and H) indicate a more normal pyrite resistivity (e.g.
ρ_{PY} = .25-1.0 Ωm) by plotting near the theoretical curves II and III",
inversion results of V suggest that the effective background
resistivity with respect to the degree of total polarization (or m) is
the electrolyte resistivity (ρ_e).

In summary the effects due to the electrolyte resistivity on the
IP spectra are in approximate agreement with Model 1 (equation 2-27)
and Model 2 (equations 2-24, 2-25 and 2-26). The background
resistivity (ρ_1) is in approximate agreement with Archie's law and/or
equation (2-20) which relates ρ_e to ρ_1 through a porosity function.
With respect to the Cole-Cole model the chargeability (Model 2,
equation 2-26) is sensitive to low resistivity contrasts between the
electrolyte and pyrite for a given volume fraction (V"). For samples
containing cement equation (4-3) suggests a reasonable approximation
of ρ_1. Due to the large surface area and cation exchange capacity of
the cement particles, it appears as a conductive element in the
synthetic rock system and must be included in the determination of V"
as in equation (4-4). This suggests that clay minerals in rocks
should also be considered by equation (4-4). The time constant for
Model 1 (equation 2-27) depends strongly on the background resistivity
(ρ_1) and the minerals' Warburg impedance (A), which are both functions

of the electrolyte properties. As the electrolyte concentrations increases ρ_1 and A decrease. Decreases in ρ_1 give smaller time constants while decreases in A cause longer time constants. The time constant is approximatley proportional to $\left[\frac{\rho_1 a}{A}\right]\frac{1}{c}$, where c is observed to range between 0.5 and 0.8 depending apparently on which part of the frequency range the dispersive region occurs.

4.2 Volume Fraction

For a constant grain size fraction H, figure 4.4 shows the effect of increasing the volume fraction of pyrite on the observed IP spectra, for a series of samples saturated with 1 Ωm electrolyte (NaCl). The volume percent indicated in the observed section of figure 4.4 are the actual volume fraction of pyrite based on the total sample volume (i.e. V'). The observed resistivity amplitudes have been normalized by the background resistivity (ρ_1) to remove slight resistivity differences mainly due to variations in porosity. The samples have a cemented matrix and porosities are on the order of 15% (table 4.2).

Increases in the volume of pyrite are observed to increase the amplitude of the maximum phase angles and the asymptotic differences in the resistivity amplitudes. Note how the theoretical inversion model (left hand side of figure 4.4) responds in a similar fashion with changes in V. A measure of the asymptotic amplitude differences is the chargeability (m). Model 2, equation (2-26) indicates that for a given resistivity ratio ρ_3/ρ_e the chargeability should only depend on V". Here ρ_3/ρ_e is estimated at one.

Figure 4.4 Effect of volume percent on the theoretial model (equation 2-29) and the observed IP spectra obtained from a suite (H) of synthetic samples containing quartz sand, cement, and various amounts of pyrite in $1\Omega m$ electrolyte (NaCl). Sample statistics and inversion results of the observed IP spectra are listd in table 4.2. The observed resistivity amplitude has been normalized by the background resistivity (ρ_1).

EFFECT of VOLUME PERCENT

56
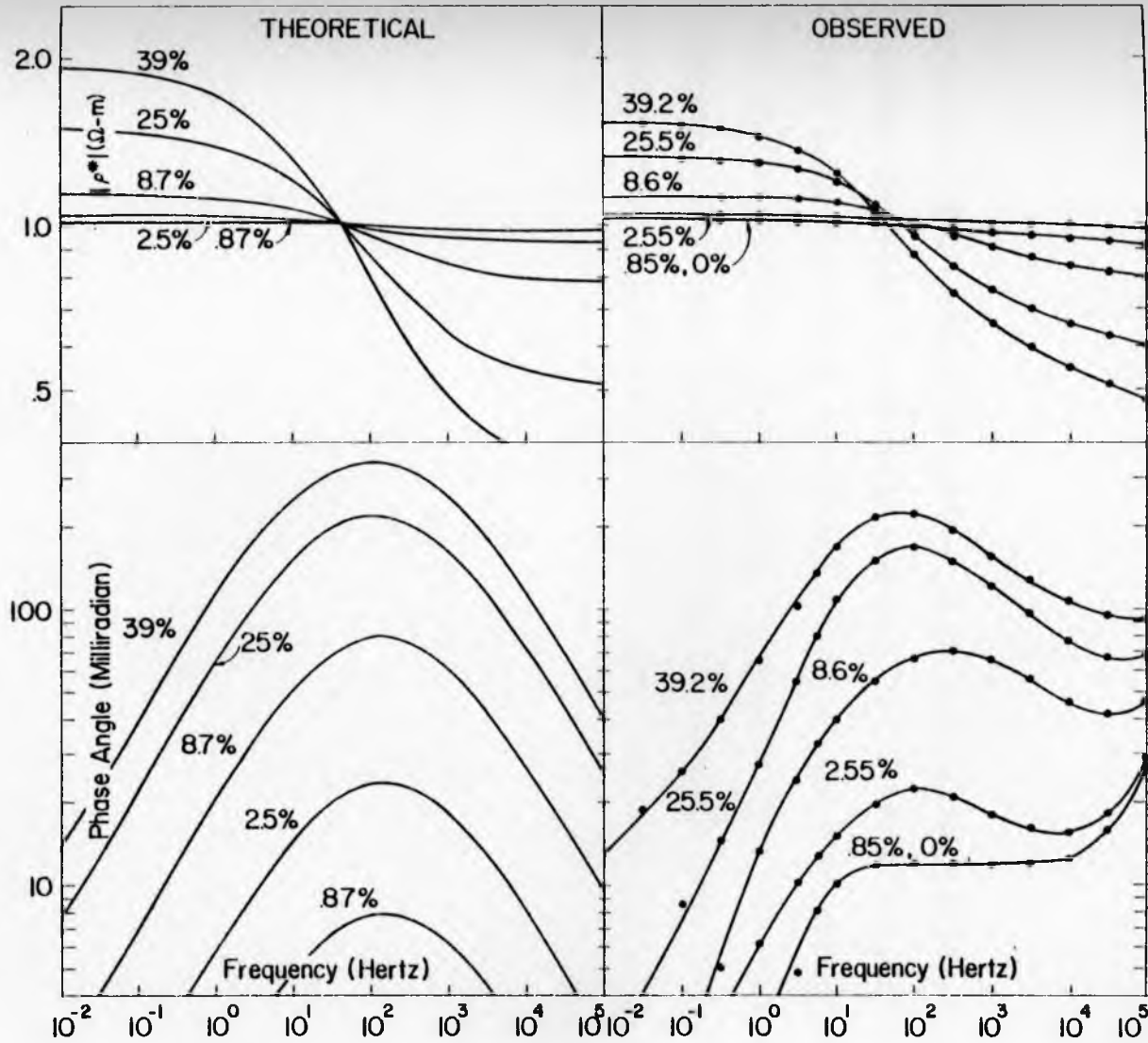
Table 4.2 Sample statistics and inversion results for pyrite volume fraction variations in synthetic samples. The observed IP spectra for sample suite H are shown in figure 4.4. V', V" and V are determined from equations (2-10), (4-6), and (4-7), respesctively. The Warburg impedance (A) is obtained by multiplying the observed grain radius (a) by the inversion parameter A/a. Letter grain radii are listed in table 4.3.

SAMPLE	POROSITY ϕ_e	VOL. FRACT. P_y			INVERTED PARAMETERS				WARBURG IMPEDANCE (Ω-m²)			TIME CONSTANT τ (SEC)
		V'	V''	$\bar{\bar{V}}$	V	ρ_1 Ω-m	C	A/a Ω-m	$A_{min.}$	$\bar{A}$	$A_{max.}$	
H 1	.16	.01	.02	.01	.0280	30.0	.433	639	.189	.281	.373	2.1×10^{-4}
H 3	.17	.03	.05	.02	.0218	27.2	.603	747	.220	.328	.436	1.5×10^{-3}
H 10	.14	.09	.17	.06	.086	24.1	.512	683	.201	.300	.399	6.1×10^{-4}
H 25	.17	.25	.32	.12	.179	21.8	.585	802	.236	.352	.468	1.5×10^{-3}
H 40	.17	.39	.39	.16	.243	18.4	.526	294	.087	.129	.172	5.0×10^{-3}
J 3	.13	.03	.05	.02	.0294	28.1	.452	361	.361	.542	.722	9.2×10^{-4}
J 10	.14	.09	.17	.06	.0796	25.0	.381	165	.165	.247	.330	2.1×10^{-3}
J 25	.13	.26	.33	.13	.189	23.6	.418	201	.201	.302	.402	4.0×10^{-3}
D 3	.14	.03	.05	.02	.0463	26.0	.618	3999	.148	.198	.248	1.2×10^{-4}
D 10	.16	.09	.16	.06	.170	23.9	.473	1520	.065	.087	.109	9.8×10^{-5}
D 25	.14	.24	.30	.12	.339	18.3	.447	925	.034	.046	.057	2.6×10^{-4}
D 40	.18	.31	.36	.14	.359	13.8	.305	172	.006	.009	.011	6.7×10^{-4}

The resistivity curves normalized by ρ_1 show a common intersection around $|\rho_a| = 1\Omega$ m and f = 30 hz, which is approximately coincident with the frequency position of the phase angle peaks (figure 4.4). Note how the theoretical inversion model displays a similar trend as the observed data. In the Cole-Cole model the peak phase angle position along the frequency axis is a function of τ and is indicated by equation (2-33) to be weakly dependent on the volume fraction V (V' or V"). However τ is indicated to have a strong dependence on ρ_1.

The low frequency asymptotes of the unnormalized resistivity amplitude (e.g. ρ_0) range between 26Ω m and 21Ω m. ρ_0 is not shown but can be calculated from equation (2-31) using the inversion results listed in table 4.2 and displays a slight increasing trend as the volume fraction of pyrite increases. This increasing trend of ρ_0 is in agreement with the idea of current going around the conductive particles at low frequencies so that larger volume fraction samples appear more resistive at low frequencies. Due to the model assumption of non-interaction among the particles and their fields (Maxwell's approach), equation (2-24, Model 2) shows that ρ_0 should depend only on the volume fraction (V") of spherical particles for a given background medium resistivity (ρ_1). Theoretically the properties of the background medium do not include effects due to conductive particles, which is apparently occurring in the samples suites H, J, and D. This is indicated by the decreasing trend in ρ_1 (table 4.2) as the volume fractions increase. Therefore contrary to theoretical expectations ρ_0 is relatively constant while ρ_1 decreases with

increases in the volume of pyrite.

Inversion results of the observed data in figure 4.4 for volume
series H are listed in table 4.2 along with those of two other
constant grain size suits J and D. Note that series D is suspect of
sample inhomogeneties as will be discussed in section 4.3. Such
inhomogeneties can produce biased inversion results, especially with
respect to parameters A/a, c, and V. As the volume of pyrite is
increased V increases, ρ_1 shows a small decreasing trend, while A/a
and c remain fairly constant. These parameter trends are in
approximate agreement with the theoretical model in that changes in
the actual volume of pyrite should only significantly change the
inversion parameter V (or m). Although theoretically ρ_1 should
remain independent of the actual volume fraction V" (see Maxwell's
approach and equation 2-24, Model 2) a decreasing trend is observed
for ρ_1 as V" increases. However for the lower volume fractions (V" <
0.2, V' < 0.1) samples listed in table 4.2 this trend in ρ_1 appears
small enough, so that the second part of equation (2-20) does a good
job of predicting the observed ρ_1, where M=2, $\rho_e = 1 \Omega m$ and $\phi_e = .15$.
For the larger volume fraction samples (i.e. H25, H40, also J and D)
ρ_1 shows more of a significant change due to increased volumes of
pyrite. Apparently at these large volume percents the distance
between neighboring pyrite particles are close enough that their
induced electric fields begin to affect one another, thereby giving
the background medium a more conductive appearance relative to an
individual pyrite particle. Therefore the background resistivity (ρ_1)
appears to be in agreement with the theoretical expectations (i.e.

relatively constant) for low volume fractions but begins to fall short at volume fractions greater than about V" = 0.2. The frequency dependence parameters (c) are around 0.5 indicating a Warburg frequency dependence (table 4.2). And the Warburg impedances ($\bar{A}$) are comparable to the magnitude obtained from the independent pyrite electrode measurments (e.g. figure 4.4 at ω=1). Therefore the inversion parameters ρ_1, A/a, and c are observed to be reasonably constant in the (low) volume fraction series H and J. Since only the volume of pyrite is thought to be changing in these samples, it appears then that the increasing trend observed in the inversion parameter V as the pyrite volume percent is increased, is due to the changing volume fraction of pyrite.

In the previous section 4.1 pyrite samples saturated with 1.0 m electrolyte were considered to give biased V Inversion parameters, due to a low resistivity contrast beween the electrolyte and the pyrite which does not allow maximum polarization. Here sample H10 (figure 4.4, table 4.2) contains the same grain sizes and volume fractions of quartz sand and pyrite as sample H-4 (figure 4.1, table 4.1), and both are saturated in 1 Ωm electrolyte (NaCl). These samples differ in porosity due to the cement in H10. Note the difference in ρ_1 between these two samples inversion results, due to porosity, while A/a, V, and c remain similar. Therefore the V Inversion parameters in this section must also be biased. Since V is similar for H10 and H-4 (and G-1) the degree of bias for the different volume fraction samples may be predicted (i.e. $\tilde{V}$) through the chargeability, as was done in section 4.1.

To assess the possible bias of the inversion parameters the method indicated by equation (4-6) was used to predict $\tilde{V}$ as listed in table 4.2. Remember $\tilde{V}$ is the predicted value of the observed inversion parameter V obtained from estimates of ρ_e (=1 Ωm) and V". For lower volume fraction (e.g. V'< 0.1, V"< 0.2) samples H3, H10, J3, and J10, the predicted volume fraction $\tilde{V}$ are in approximate agreement with their inversion paramters V as can be observed in table 4.2.

Note that sample H1($\neq$ H-1 of sec. 4.1) contains a very low volume of pyrite and the pyrite response is essentially masked by the membrane polarization of the cement (see figure 3.3 as reference), making its inversion results unreliable. At larger volume fractions (e.g. H25, H40, and J25) the actual inversion parameters V begin to get larger than their respective $\tilde{V}$, indicating a deviation from the theoretical model. For example as the volume of pyrite increases, the particles get closer together and more of their induced electric fields can interact which can increase the total polarization. The theoretical model does not take this into account because the Maxwell approach assumes non-interacting particle fields. Therefore the observed deviations at large volume fractions suggest when Maxwell's approach is appropriate. Since the lower volume fraction samples are observed to have inversion parameters V which can be approximately estimated by $\tilde{V}$, indications are that V is giving pertinent information relative to V", ρ_3 and ρ_e. With this in mind any similarity between V' (Model 1) and V, as is observed in figure 4.4 and table 4.2 is then purely coincidental.

So far equation (2-27, Model 1) has been suggested as being an appropriate expression for the time constant with respect to ρ_1, a, and A. In order to investigate this, equation (2-27) is rearranged and left in the general form

$$\tau^c \left[\frac{A}{\rho_1 a} \right] = \left(\frac{1+2V}{2(1-V)} + \frac{\rho_3}{\rho_E} \right) = \frac{1+2\tilde{V}}{2(1-\tilde{V})} \,, \qquad (4\text{-}8)$$

where V can represent V' or V", and ρ_E can represent ρ_1 or ρ_e. $\tilde{V}$ is an estimate of what the observed inversion parameter V might be, based on estimates of ρ_e, ρ_E and V in equation (4-8).

Figure 4.5 shows a family of curves and the general equation (4-8) used to calculate them for different volume fractions. Note each curve is calculated for a constant resistivity ratio. As ρ_3/ρ_E goes to zero, $\tilde{V}$ goes to V. For volume fractions lower than about 0.2 differences in the resistivity ratio merely raises or lowers the horizontal portion of the curves, indicating the weak effect of low volume fractions on the time constant. Therefore at low volume fractions the expression $\dfrac{1+2\tilde{V}}{2(1-\tilde{V})}$ calculated from the inversion results of V and plotted in figure 4.5, should give information relative to the effective resistivity ratio with respect to the time constant.

Typical resistivity values observed or estimated for the volume suites H, J and D are

$$\rho_3 = \rho_{py} \approx 1 \Omega m$$
$$\rho_e = 1 \Omega m$$
$$\rho_1 = 25 \Omega m$$

63

Figure 4.5 Plot of τ^c ($\frac{A}{a^\rho{}_1}$) versus the volume fraction using equation (4-8) for various effective resistivity ratios ρ_e/ρ_E. Inversion $\hat{\tilde{V}}$ results for the synthetic sample data H,J, and D are listed in table 4.2. $\tilde{V}$ is the biased volume fraction when $\rho_3/\rho_E \neq 0$.

$$\tau^c \left(\frac{A}{a \rho_1} \right) = \left[\frac{1+2v}{2(1-v)} + \frac{\rho_3}{\rho_E} \right] = \frac{1+2\breve{v}}{2(1-\breve{v})}$$

II: $\frac{\rho_3}{\rho_E} = 1$, $\breve{v} \neq v$

I: $\frac{\rho_3}{\rho_E} = 1/25$, $\breve{v} \approx v$

III: $\frac{\rho_3}{\rho_E} = 0$, $\breve{v} = v$

VOLUME FRACTION - V

SAMPLE SUITE	V'	V''
H	●	○
H, J	▲	△
D	■	□
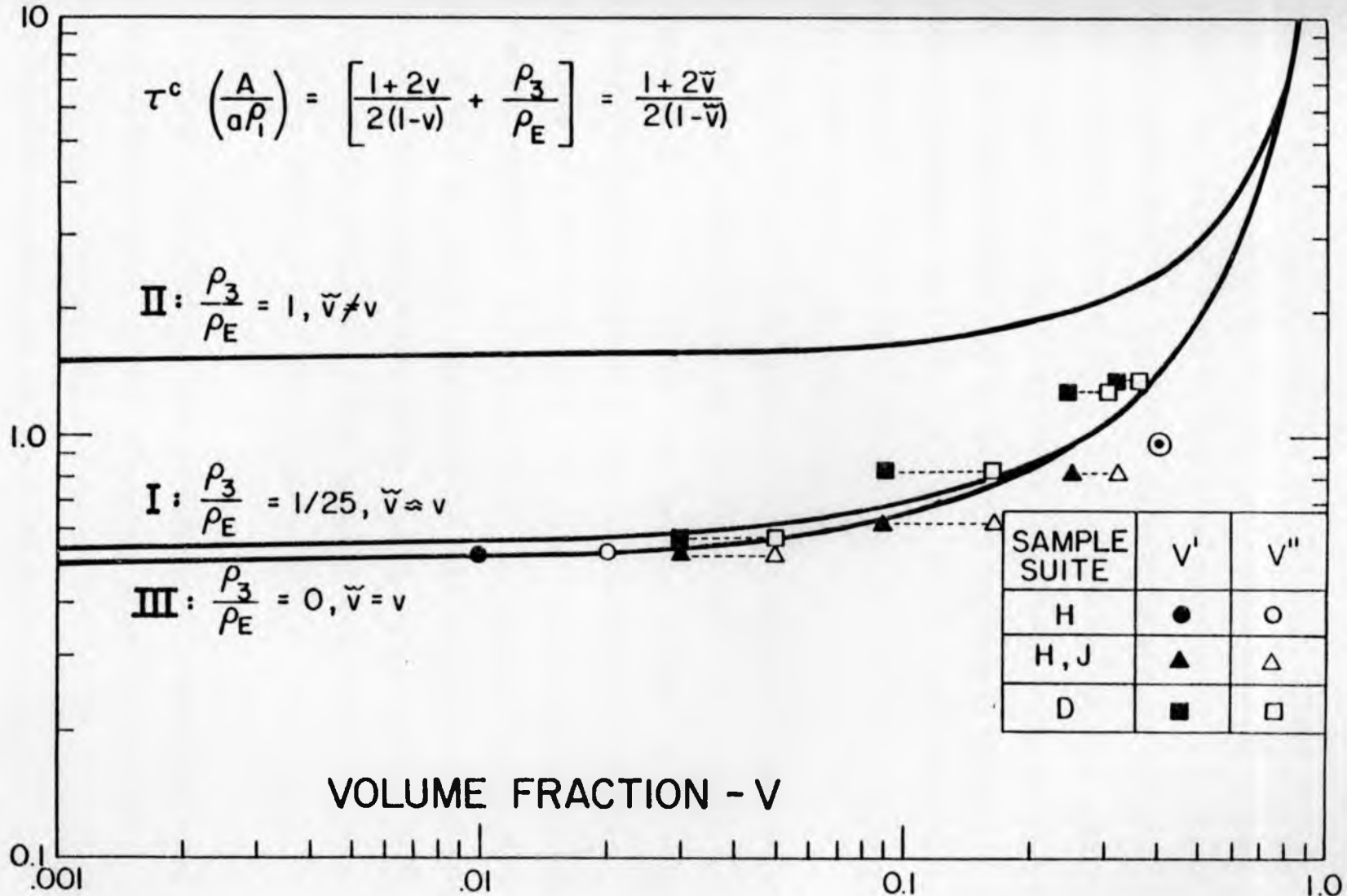
Note that the observed data points from suites H, J and D plotted in figure 4.5 fall around curves I and III, indicating a low resistivity ratio. Low resistivity ratios are indeed observed for ρ_3/ρ_1 (model 1) which suggest that the resistivity contrast between the pyrite (ρ_3) and the backgound resistivity (ρ_1) is influencing the time constant of these samples. The resistivity ratio ρ_3/ρ_e (Model 2) for suites H, J and D are approximately one and as can be seen none of their respective data points plotted in figure 4.5, are observed to fall near curve II. This suggests ρ_3/ρ_e is not the effective resistivity ratio with respect to the time constant.

Because V' and V" for suites H, J and D (table 4.2) do not differ by more than a factor of two and the time constant shows a weak dependence on V, it is difficult for the data observed in figure 4.5 to make a distinction between V' and V". However the strong indication of a low resistivity ratio (i.e. $\rho_3/\rho_1 \approx 0$, figure 4.5, curves I and III) theoretically must opt for V', as indicated in the first part of equation (2-27). Neglecting the data from sample D (samples thought to have inhomogeneous pyrite distributions), the data $(\frac{1+2V}{2(1-V)}$, V') for sample suites H and J does appear to plot closer to curves I and III in figure 4.5 than does the data $(\frac{1+2V}{2(1-V)}$, V") for these samples.

Figure 4.6 displays the data obtained by Grissemann (1971) for a set of synthetic rocks. Similar trends are observed in the data supporting the theoretical model. Figure 4.6 shows the chargeability as a function of volume percent, where the observed data follow a similar trend as the theoretical prediction. Although the time

Figure 4.6 Grissemann data for the time constant and chargeability versus the volume fraction.

GRISSEMAN DATA

$$m = \frac{9V}{(1+2V)(2+V)}$$

m

$$T = \left[\left(\frac{a\rho_1}{2}\right)\left(\frac{1+2V}{1-V}\right)\left(\frac{F^2}{RT}C\sqrt{D'}\right)\right]^2$$

T (sec)

T

V (VOLUME FRACTION SULFIDE)
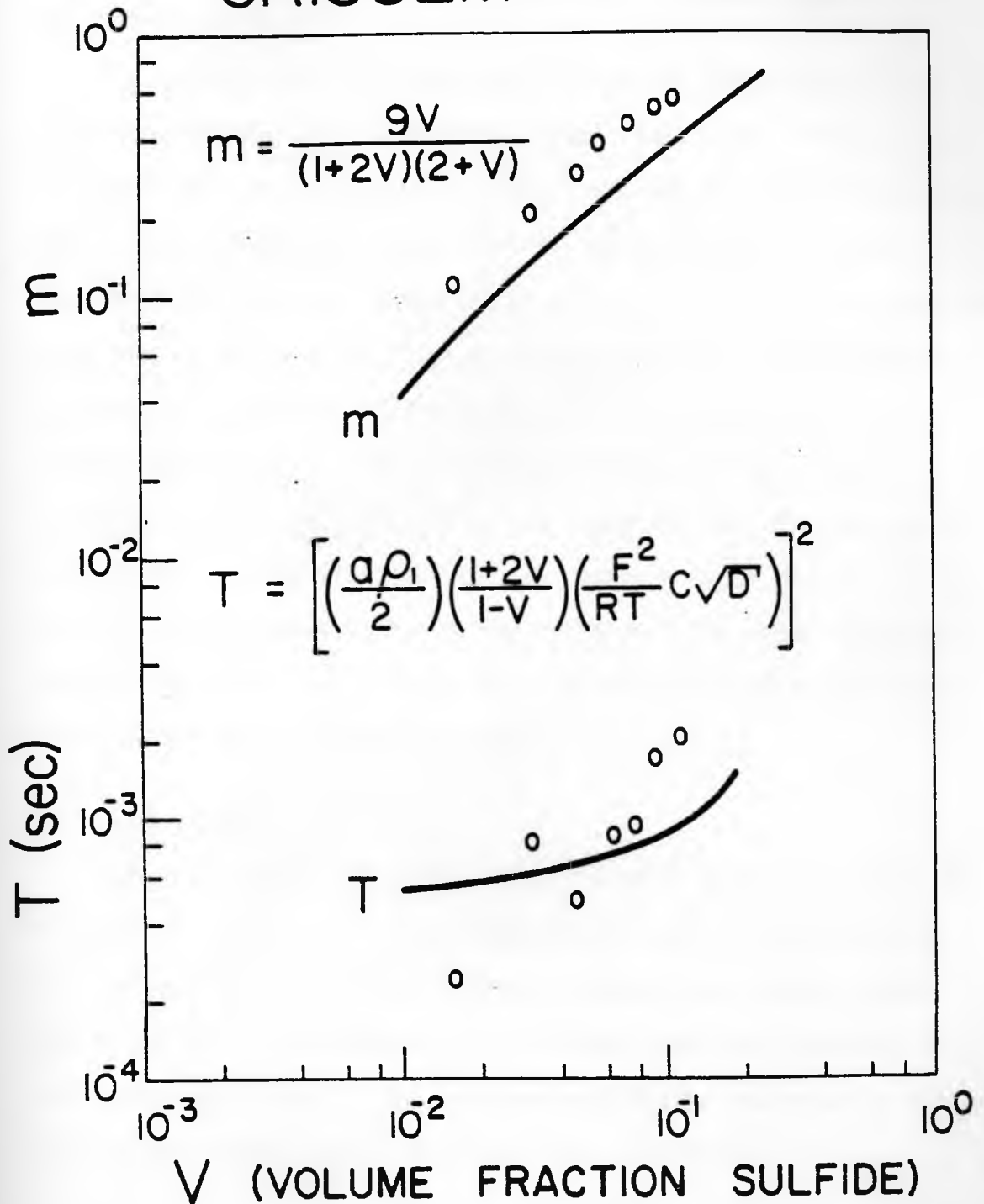
constant versus volume percent show a great deal of scatter in the observed data, there is a general trend in the same direction as the theoretical curve.

The observed data for the synthetic samples discussed in this section agrees well with theoretical model for changes in low volume fractions (V"), and resistivity contrast between the mineral particles and the electrolyte with respect to the chargeability (m). The chargeability expression given in equation (2-26, Model 2) was applied using the estimates of ρ_e, ρ_3, and V" to predict ($\tilde{V}$, $\tilde{m}$) the smaller IP response (i.e. observed inversion results V, m) due to less than maximum polarization. For low volume fractions (V"< 0.2) the predicted values ($\tilde{V}$,$\tilde{m}$) were within the range observed for the sample suites H and J. The time constant was observed to be fairly insensitive to changes in the volume fraction. The volume fraction V' and the resistivity ratio ρ_3/ρ_1 are indicated to be the appropriate terms in the time constant expression.

4.3 Grain Radius

Figure 4.7 shows the effect of pyrite grain size on the observed IP spectra. Sample grain sizes cover three orders of magnitude and are labeled A though M, where sample A contains the smallest grain size of pyrite. These samples contain cement and were saturated with 1 Ωm electrolyte (NaCl). The observed resistivity amplitude in figure 4.7 have been normalized by the background resistivity, ρ_1.

Note how the dispersive regions of samples C', I and M shift to lower frequencies as grain size is increased, in a similar fashion as

Figure 4.7 Effect of grain radius on the theoretical model (equation 2-29) and the observed IP spectra obtained from a suite (A to M) of synthetic samples containing pyrite, quartz sand, and cement in 1 m electrolyte (NaCl). Sample statistics and inversion results of the observed IP spectra are listed in table 4.3. The observed resistivity amplitude has been normalized by the background resistivity (ρ_1).

EFFECT of GRAIN SIZE
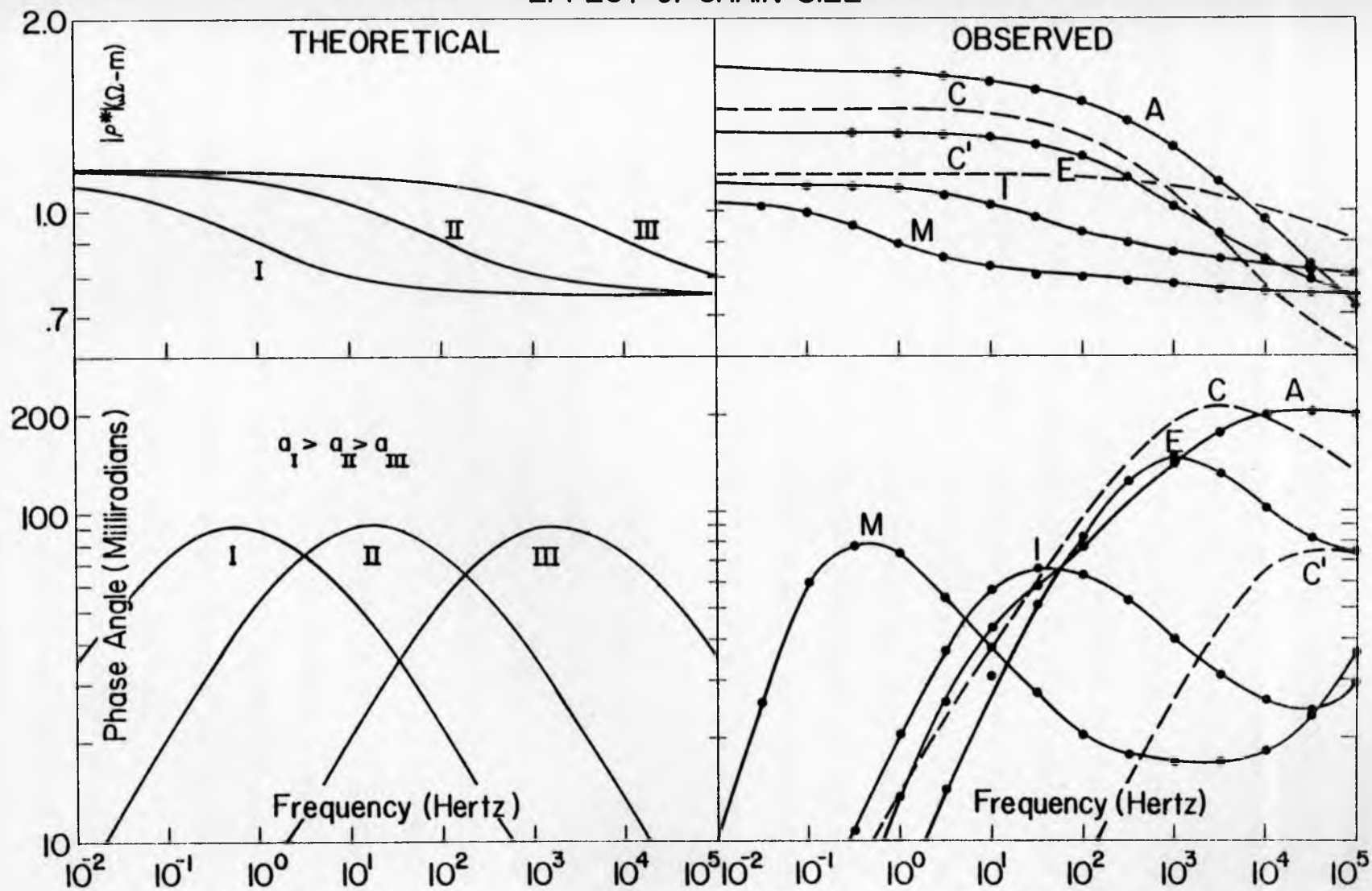
the theoretical inversion model (left side of figure 4.7). The Cole-Cole time constant (τ), which determines the frequency position of the dispersive region, has a strong dependence on grain size as in equation (2-33). Samples A, C, and E also shift their dispersive regions to lower frequencies, however their maximum phase angles and resistivity asymptotic differences (figure 4.7) show a decreasing trend as grain size is increased. This particular trend is not indicated by the theoretical model for changes in grain size. The chargeability (m) is a measure of the resistivity asymptotic difference, which theoretically (equation 2-26, Model 2) only depends on the volume fraction (A-M: V"=.16) of spherical particles and the resistivity ratio between the pyrite and the electrolyte (A-M: $\rho_3/\rho_e \approx 1$).

While for purposes of clarity figure 4.7 shows the observed data of a few of the grain size samples, table 4.3 lists all the inversion results and sample statistics. Theoretically as grain size (a) of pyrite increases, only the inversion parameter A/a should decrease. This is observed in table 4.3 for samples E to M and C'. Although samples A to D show a similar trend, it appears to be out of sequence with the larger grain size samples. Since the Warburg impedance (A) is assumed to be constant with grain radius (a) apparently a shift in the observed grain size has occurred, which has resulted in similar A/a parameters for samples such as D and F (table 4.3).

The background resistivity (ρ_1) is in approximate agreement with equations (2-20) and (4-3), and shows no significant trend due to changes in pyrite grain size. The frequency dependence parameters c

Table 4.3 Sample statistics and inversion results for pyrite grain size variations in synthetic samples. The observed IP spectra for some of the sample A-M are shown in figure 4.7. V', V'', and $\hat{V}$ are determined from equations (2-10), (4-6), and (4-7) respectively.

SAMPLE	POROSITY ϕ_e	PYRITE GRAIN RADIUS (a in mm)	VOL. FRACTION PY.			INVERTED PARAMETERS				WARBURG IMPEDANCE (Ω-m^2)		
			V'	V''	$\widetilde{V}$	V	ρ_1 Ω-m	C	A/a Ω-m	$A_{min.}$	$\bar{A}$	$A_{max.}$
A	.12	< .0125	.09	.18	.06	.281	35.8	.382	2048			.026
B	.12	.0125 - .0215	.09	.18	.06	.244	35.9	.425	1837	.023	.031	.040
C	.12	.0215 - .037	.09	.18	.06	.215	32.3	.510	3144	.068	.092	.116
C'	.21	.0215 - .037	.07	.15	.05	.075	5.34	.561	5779	.124	.169	.214
D	.16	.037 - .062	.09	.16	.06	.170	23.9	.473	1520	.065	.087	.109
E	.12	.062 - .104	.09	.18	.06	.122	29.8	.581	2993	.186	.248	.311
F	.12	.104 - .175	.09	.18	.06	.132	41.9	.543	1682	.175	.235	.294
G	.16	.175 - .295	.09	.16	.06	.093	28.3	.524	1076	.188	.253	.317
H	.14	.295 - .584	.09	.17	.06	.086	24.1	.512	683	.201	.300	.399
I	.16	.584 - 1.00	.09	.16	.06	.073	26.7	.512	318	.186	.252	.318
J	.14	1.00 - 2.00	.09	.17	.06	.080	25.0	.381	165	.165	.247	.330
K	.09	2.00 - 3.35	.09	.19	.07	.095	43.5	.439	11.3	.023	.030	.038
L	.12	3.35 - 470	.09	.18	.06	.039	36.0	.459	55.5	.186	.223	.216
M	.09	5.50 - 7.50	.09	.19	.07	.072	40.1	.527	46.4	.218	.302	.348

are around 0.5 indicating a simple Warburg dependence.

The inversion parameter V is similar for the larger grained samples G-M (and C'). However at sample F (table 4.3) V begins to suddenly increase and continues this trend as grain size is decreased toward sample A (C' not included). This trend is not indicated by the theoretical model for samples containing equal volumes of pyrite and a given resistivity ratio ρ_3/ρ_e . Remember from sections 4.1 and 4.2 that pyrite samples saturated with 1Ωm electrolyte (i.e. $\rho_3/\rho_e \approx 1$) having equal volume fractions (V"=.16) were considered to produce biased inversion results with respect to V. The degree of bias was estimated to be around $\tilde{V}$=.06, as a result of maximum polarization not occurring in such samples. Samples A-M are also saturated with 1 m electrolyte (NaCl) and contain pyrite so that their estimated $\tilde{V}$ might be expected to be around .06. In fact sample G (table 4.3) and G-1 (table 4.1) are the same sample, as are samples H (table 4.3) and H10 (table 4.2).

However, samples A-F show inversion parameters V two to five times greater than that which might be explained (V=.06) through resistivity contrast considerations involving the pyrite and electrolyte. These larger volume fractions especially over V" = .16, represent a greater degree of polarization within the samples than would be expected for spherical particles homogeneously distributed. Although nonspherical particle shapes can be responsible for greater polarization for a given volume of particles, the pyrite used here was fairly equi-granular with axial ratios generally not greater than 3:1:1.

Nonspherical particles can separate charge a greater distance than on a sphere of equal volume, so that its dipole moment will be larger then that of a sphere. Two or more spherical particles in electrical contact will allow charge to be separated a greater distance, resulting in a larger dipole moment. If these particles are not in electrical contact but close enough that their dipolar fields interact, the resultant field from a distance can appear to have a dipole moment of a nonspherical particle. This apparent dipole moment can be larger than the sum total of all the fields produced by the individual particles. Whether or not the particles are in electrical contact, an inhomogeneous distribution of particles can produce greater polarization and therefore larger inversion parameter V (and m) than if the particles are homogeneously distributed. However since the parameter A/a (and τ) is sensitive to distance (a) that charge is separated, this parameter (A/a) may be able to determine whether or not particles are in electrical contact. If the particles are touching then the inversion parameter A/a should be smaller (τ should be larger) than anticipated. The inversion results listed in table 4.3 suggest that the smaller grain size samples A to F are inhomogeneously distributed with respect to the pyrite. Although more experimental data is needed to make a case as to which inhomogenous samples have particles in electrical contact (or not), what data is available implies that samples B to F have a greater degree of particles in electrical contact, than has sample A.

The sample inhomogeneities are thought to be related to the very uniform size (H) of the quartz sand, which all the synthetic samples

in this report contain, except for sample C'. Sample C' is used as a test sample and contains pyrite and quartz sand of equal dimensions. Since a single size of quartz sand was used in all the samples, a non-uniform distribution of pyrite grains at small grain sizes is possible. Figure 4.8 (1) shows the possible geometry of sample H, having ten percent pyrite, where the grain size of quartz sand and pyrite are equal. As the radius of the pyrite is decreased (figure 4.8 (2), sample G) the tendency for pyrite grains to fit into interstitial spaces between the quartz grains in increased. Further decrease in radius (figure 4.8 (3), sample F) increases the probability of particles touching within these spaces.

In the inversion model the parameter V (or m) is a measure of the total charge separation and V in table 4.3 for samples F to A do exhibit larger values than anticipated ($\hat{V}$ = .06, V"=.16). The increasing trend observed in V as grain size is decreased from F to A would suggest that as the grain size is decreased more particles are getting closer together. For example, as a greater number of particles come together, more of their fields interact which can increase the total polarization. This could be happening in the pyrite samples when the pyrite gets fine enough relative to the quartz sand that, interstitial groups of pyrite would have a greater possibility of becoming electrically associated with each other. The inversion parameter A/a for samples F to A exhibit smaller values than anticipated, as indicated by the smaller calculated Warburg impedance (table 4.3) relative to the larger grain size samples G to M. This suggests that electrical contact between the pyrite particles may be

Figure 4.8   Approximate synthetic sample geometry showing quartz sand and pyrite distribution for different grain sizes of pyrite.

SAMPLE   GEOMETRY
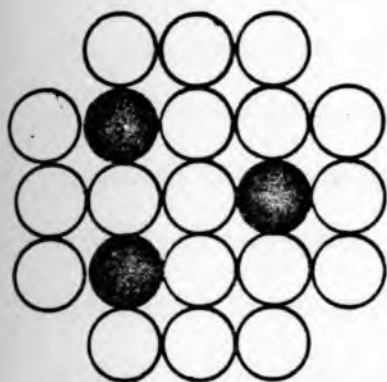
1 (H)
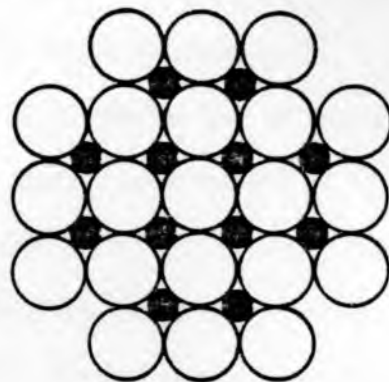
2 (G)
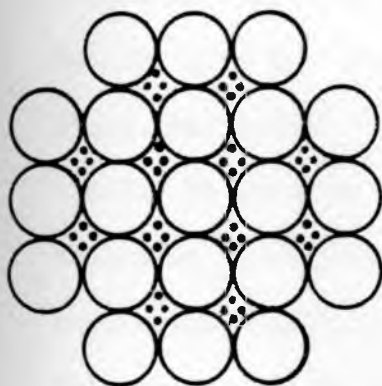
3 (F)

4 (I)

occurring to some extent in samples F to A.

Since the constant grain size of quartz sand is thought to be producing samples inhomogeneties with respect to the smaller grained pyrite distributions, a second sample C' was constructed. This sample has the same size sand as pyrite to promote a more homogeneous distribution of pyrite particles. Figure 4.9 compares the IP spectra obtained from samples C and C'. The dashed curve in figure 4.9 is the phase angle response with an approximate membrane polarization, due to the cement, removed. As can be seen the possible error due to membrane polarization does not fully account for difference in the maximum phase amplitudes or phase peak positions between these two samples. Most of the observable change in peak phase position is apparently due to differences in ρ_1 as a result of porosity variations. However sample C' does show a larger inversion parameter A/a and smaller V relative to sample C, and the calculated Warburg impedance (table 4.3) is closer to those of the large grain size samples G to M. The inversion parameter V (table 4.3) and the maximum phase amplitudes (figure 4.7) of sample C' also show magnitudes more similar to those of the larger grained samples (G-M). Therefore the inversion results for sample C' appear to be in agreement with the theoretical model, suggesting that the particle fields have less interaction due to a more homogeneous distribuion of pyrite.

Note that in table 4.3 the inversion parameter V shows no particular trend for the larger grain size samples G-M (and C') and ranges between .07 to .09. This range is roughly approximated by V=.06 as is observed. This suggests that the chargeability as

Figure 4.9 Amplitude and phase spectra of two synthetic samples
containing pyrite, quartz sand, and cement in 1 m electrolyte (NaCl).
The quartz grains in sample C are much larger than the pyrite, while
sample C' contains quartz sand and pyrite of similar grain sizes. The
inversion results and sample statistics of the observed data are
listed in table 4.3.
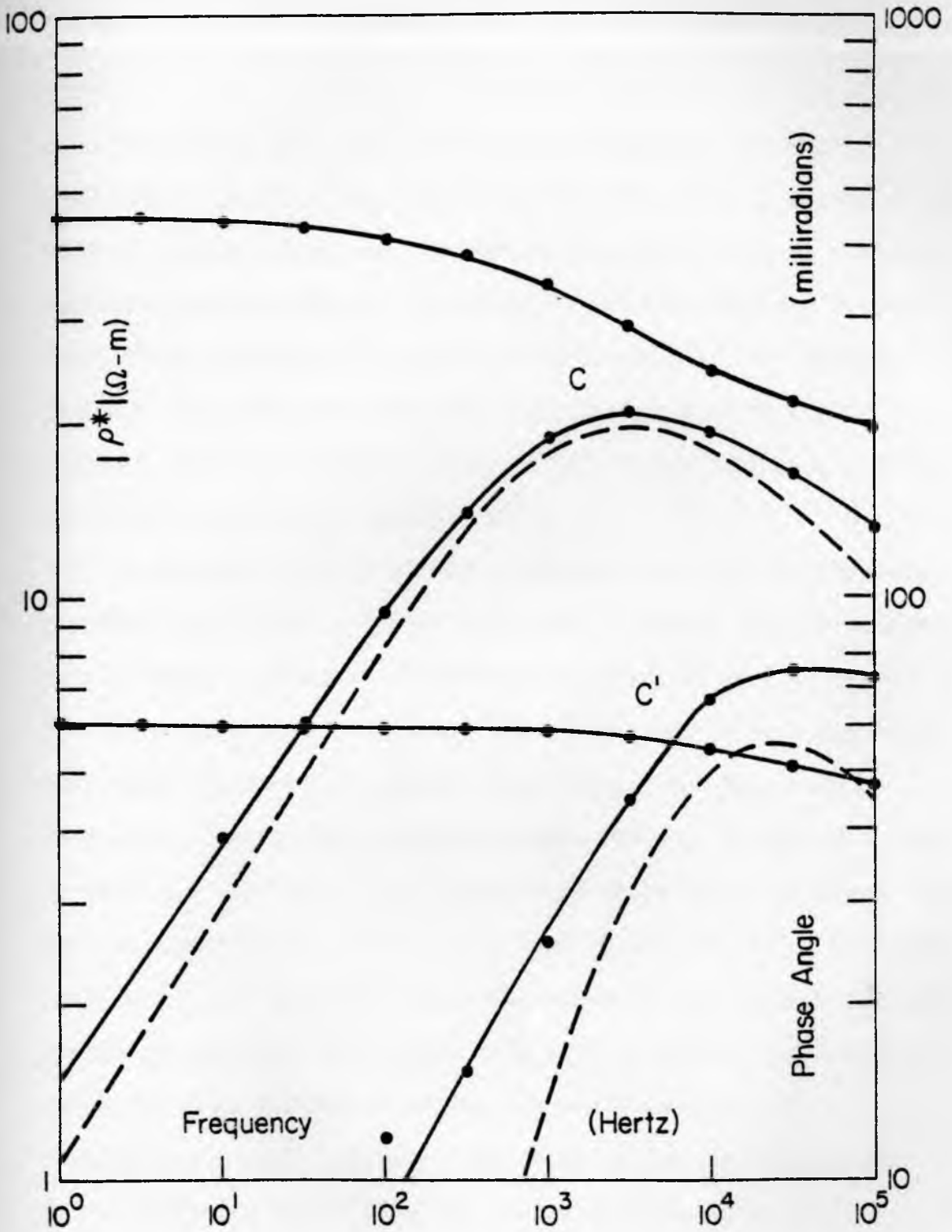
indicated by equation (2-32) is depending on the volume fraction V"
and the resistivity ratio $\rho 3/\rho_e$ and not a function of spherical grain
size.

This agrees well with the theoretical expectations of IP
phenomenon resulting from induced dipolar fields having a cube of the
particle radius dependence. Therefore predicting IP to be a volume
related phenomenon and not a function of the total exposed surface
area, which would have a radius squared dependence. For example
sample C' has about 200 times the total surface area of pyrite as
sample M, both have similar volumes of pyrite and both show inversion
parameters V around .07 (table 4.3).

As the grain size of pyrite increases from A to M the inversion
parameter A/a listed in (table 4.3) shows a general decreasing trend.
This parameter represents the Warburg impedance (A at $_\omega$=1) divided by
the grain radius (a). Since the grain size range in each sample is
well known the Warburg impedance range ($A_{min} < A < A_{max}$) can be
determined. The Warburg impedance ranges for samples A-M are listed
in table 4.3 and plotted as a function of grain radius in figure 4.10.
Note in figure 4.10 that for grain sizes C' and E-M, which vary over
three and a half orders of magnitude, quite similar Warburg impedance
ranges are observed with a mean value of $\overline{A} = .23\Omega m^2$. The impedance
ranges of these particular samples are again (section 4.1) in
reasonable agreement with the range observed for the independent
pyrite electrode measurements by various authors, using similar
electrolyte ion concentrations (e.g. $1.5\Omega m^2 < A < 0.1\Omega m^2$). In .3 m
NaCl, Scott and West (1969) show an average specific impedance of $.24\Omega$

Figure 4.10 Plot of Warburg impedance of pyrite versus grain radius. Inversion results for the synthetic samples (A to M) are listed in table 4.3. The dashed line in the figure is the average Warburg impedance based on samples E to M and C'. The closed circles represent samples containing one grain size fraction of pyrite, while the two open circles represent a single sample containing two different grain size fractions (B and M).

WARBURG IMPEDANCE OF PYRITE
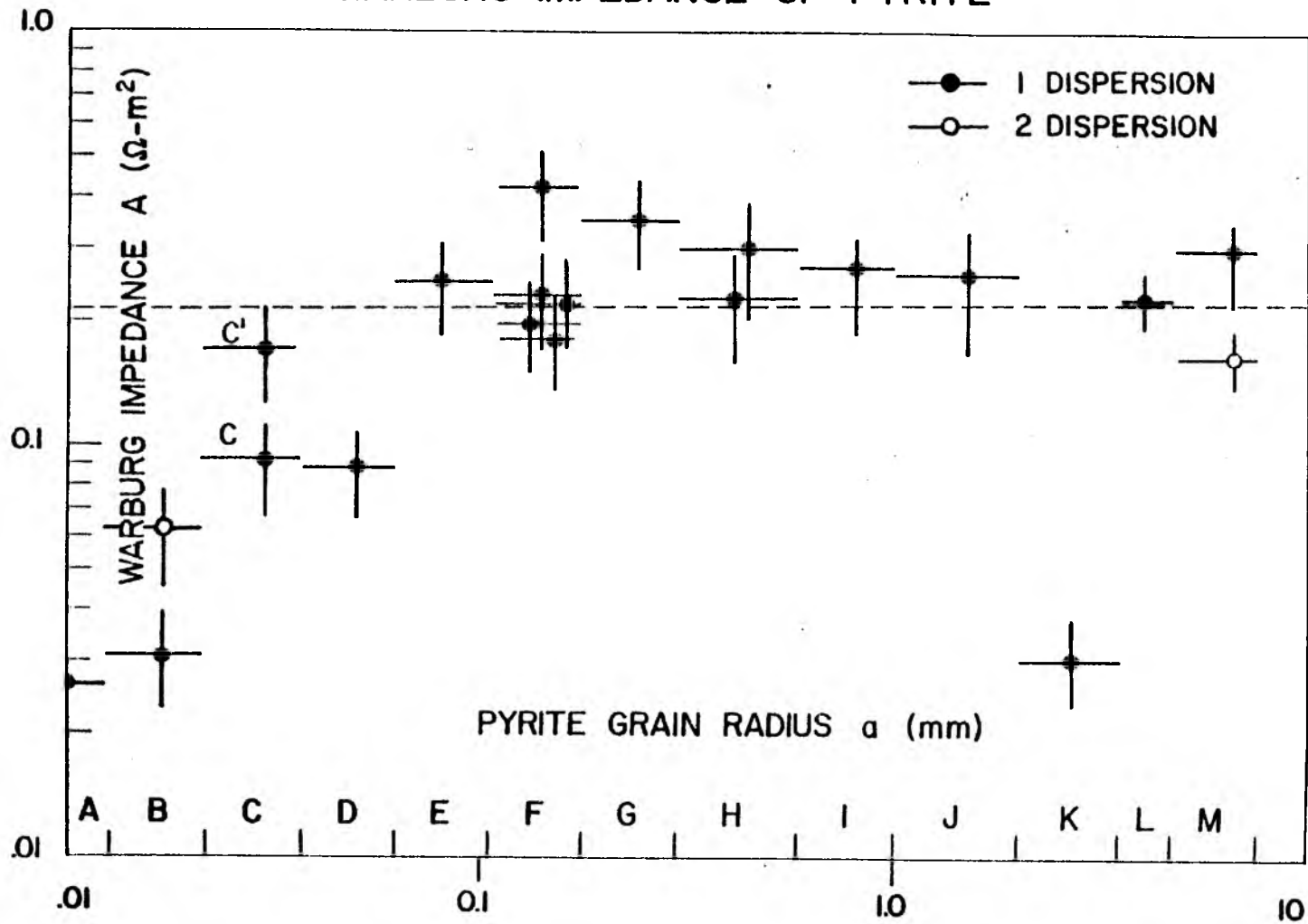
m^2 when using a subjective curve-fitting procedure on decay curves obtained from their artificial pyrite samples. Sample K in figure 4.10 appears to be noisy relative to the other grain size samples G to M and C'. The largest grain size samples K, L, and M were hand packed and have 56, 16 and 4 pyrite particles respectively in each sample (sample A has about .55 billion particles). Possibly the hand packed sample K did not achieve a homogeneous distribution, and it is felt that particles in this sample may be in electrical contact producing larger length scales than intended. Therefore with respect to the well known grain sizes ranges C' and F to M the inversion parameter A/a for most of these samples appear to be giving reasonable information about the impedance of pyrite at $\omega=1$. Note in figure 4.10 that samples D-A show a sudden decreasing trend in the calculated Warburg impedance as grain size is decreased. This trend is thought to be only an apparent trend due to sample inhomogeneities allowing electrical contact between the pyrite particles. This effectively increases the intended grain size so that the length scale (a) used to calculate the Warburg impedance is no longer well known. The direction of this apparent trend is in agreement with the idea of pyrite particles gathering into interstitial spaces until they get fine enough to form connecting stringers between the main interstitial groups.

The Cole-Cole time constant (equation 2-33) is indicated to be proportional to the grain size squared for a simple Warburg frequency dependence of c =.5. The inversion results (table 4.3) of sample suite A-M have been used to calculate the Cole-Cole time constant

Figure 4.11 Plot of time constant versus pyrite grain radius.
Inversion results for the observed data are listed in table 4.3. The
time constant has been normalized by the background resistivity (ρ_1).
The smooth and dashed lines are the theoretical predictions based on
estimates of the Warburg impedance (A), the biased volume fraction
($\tilde{V}$), and the frequency dependence (c).

$$\frac{\tau}{\rho_1^{1/c}} \left[\frac{(1+2\,\check{V})\,a}{2(1-\check{V})\,A} \right]^{1/c}$$

SAMPLE •———•

THEORETICAL / /

A = 0.1 Ω-m², V̌ = .06, C = 0.5

A = .25 Ω-m², V̌ = .06, C = 0.5

A = 1.0 Ω-m², V̌ = .06, C = 0.5

C

C'

GRAIN RADIUS - a (mm)
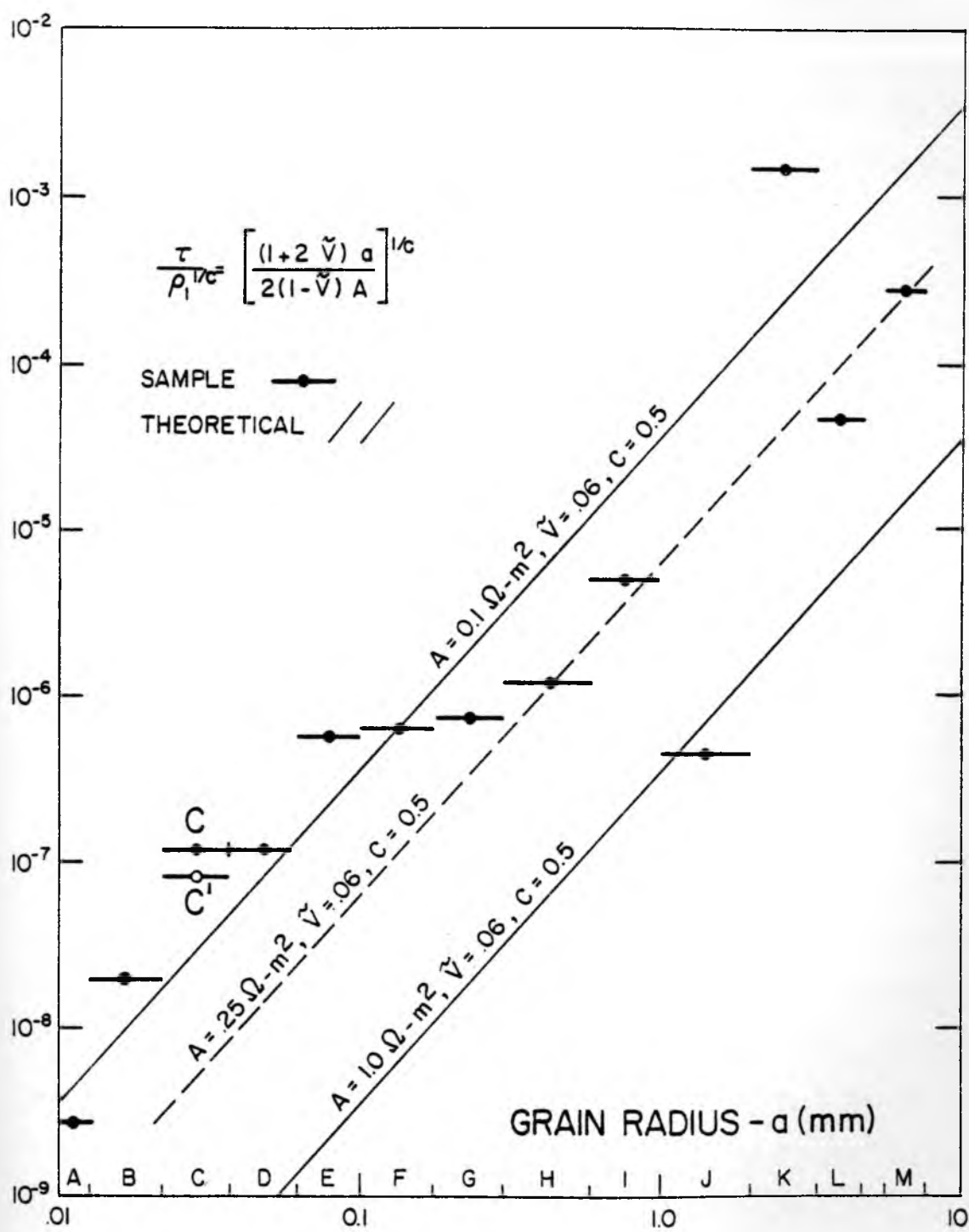
(τ) which is plotted as a function of grain size in figure 4.11. Note that τ has been normalized by $\rho_1^{1/c}$ to remove resistivity differences between samples having different porosities (e.g. samples C' and H). The observed data ($\tau/\rho_1^{1/c}$,a) for the larger grains size suite G-M, fall within the theoretical lines which are loosly based on independent electrode impedence measurements (i.e. $0.1\Omega m^2 < A < 1.0\Omega m^2$), estimates of $\tilde{V}$ ($\approx.06$), and where c=0.5. The observed data for these larger grain sizes are approximately fit by the dashed line, indicating an average Warburg impedance of $\bar{A}=.25$ Ωm^2 (see also figure 4.10) and a Warburg frequency dependence of c = 0.5. Sample K here is again noisy, however if particles are in electrical contact as suggested earlier then its data ($\tau/\rho_1^{1/c}$) in figure 4.11 should have been plotted at larger grain sizes. This would displace the data for sample K toward the theoretical region indicated in this figure. Sample J is also noisy and shows a lower value ($\tau/\rho_1^{1/c}$) than expected in figure 4.11. Most of this grain size fraction (J) was used in the large volume fraction samples (J suite, table 4.2) so that a shortage occurred. Therefore smaller grain sizes of pyrite may have been included to obtain an equal weight of pyrite relative to the other samples A-M. The position of the data ($\tau/\rho_1^{1/c}$) for sample J relative to theoretical expectations in figure 4.11 does suggest smaller grain sizes in this samples than intended. Although the data is noisy for the grain sizes G to M they do appear to support a grain radius (a) squared relationship with the time constant (τ).

The deviations observed for samples A to F (figure 4.11) from the theoretical region is thought to be related to pyrite particles coming

into electrical contact as discussed previously. This suggests that their data $(\tau/\rho_1^{1/c})$ should actually have been plotted at larger grain sizes. For example, figure 4.8 indicates that sample G is homogeneous but sample F is becoming inhomogeneous due to pyrite having preferred interstitial sites between quartz grains. As the grain size is further decreased (e.g. F to E in figure 4.11) the pyrite continues to collect into interstitial spaces of dimensions determined by the quartz size (H). Therefore although the grain size of pyrite is decreasing, the average interstitial groups of pyrite maintain their original dimensions. Note in figure 4.11 how the data $(\tau/\rho_1^{1/c})$ for sample E,F,G, and H remain fairly constant with grain size indicating common length scales. However as the pyrite becomes fine enough, stringers of pyrite may begin to form electrical connections between the main interstitial pyrite groups. Note in figure 4.11 that the data $(\tau/\rho_1^{1/c})$ for sample E to B again begin to decrease with grain size. Although due to the apparent larger length scales (a) than anticipated, their data plots above the theoretical region.

A length scale squared relationship with τ is again indicated however. As the pyrite gets very fine (e.g. sample A) the particles should become more homogeneously distributed in the available sample space, so that the possible electrical continuity is decreased. Note in figure 4.11 that the data $(\tau/\rho_1^{1/c})$ for sample A is within the theoretical region. However due to the much larger quartz size these finer pyrite particles must still be distributed in a smaller portion of the sample. Therefore it appears that although a majority of particles in sample A are not in electrical contact their close

proximity to one another still produces greater polarization due to particle field interaction. This greater degree of polarization is indicated by the larger inversion parameter V(=.3) than estimated ($\tilde{V}$=.06) for sample A (table 4.3).

Sample C' remember is thought to be more homogeneous than sample C and although their data in figure 4.11 plot close together, C' is closer to the theoretical region. Although this is a rather complex interpretation based on a common grain size of quartz for simple decreases in pyrite grain size, it does appear to explain the majority of trends observed in figure 4.11 within a theoretical framework. Since none of the small grain size distributions have actually been observed, this discussion is mainly an exercise to demonstrate the theoretical concepts. In general the time constant is observed to be proportional to the grain radius (a) squared or if particles are in electrical contact a length scale squared. Pyrite particles in electrical contact or close to each other can effect larger dipole moments and therefore greater chargeabilities (or V) than if the particles are far apart.

Figure 4.12 displays the data obtained by Grissemann (1971) for a set of synthetic rocks. Similar trends are observed in the data supporting the theoretical model. Figure 4.12 shows the observed time constant proportional to the radius squared and is in good agreement with the theoretical prediction. The chargeability data show an increasing trend with decreasing grain size. This was also observed in the present study.

In summary the effect of spherical grain radius (a) on IP spectra

Figure 4.12   Grissemann data for the time constant and chargeability versus the grain radius.

GRISSEMAN DATA

$$m = \frac{9V}{(1+2V)(2+V)}$$

$$T = \left[\left(\frac{a\rho_1}{2}\right)\left(\frac{1+2V}{1-V}\right)\left(\frac{F^2}{RT}C\sqrt{D}\right)\right]^2$$
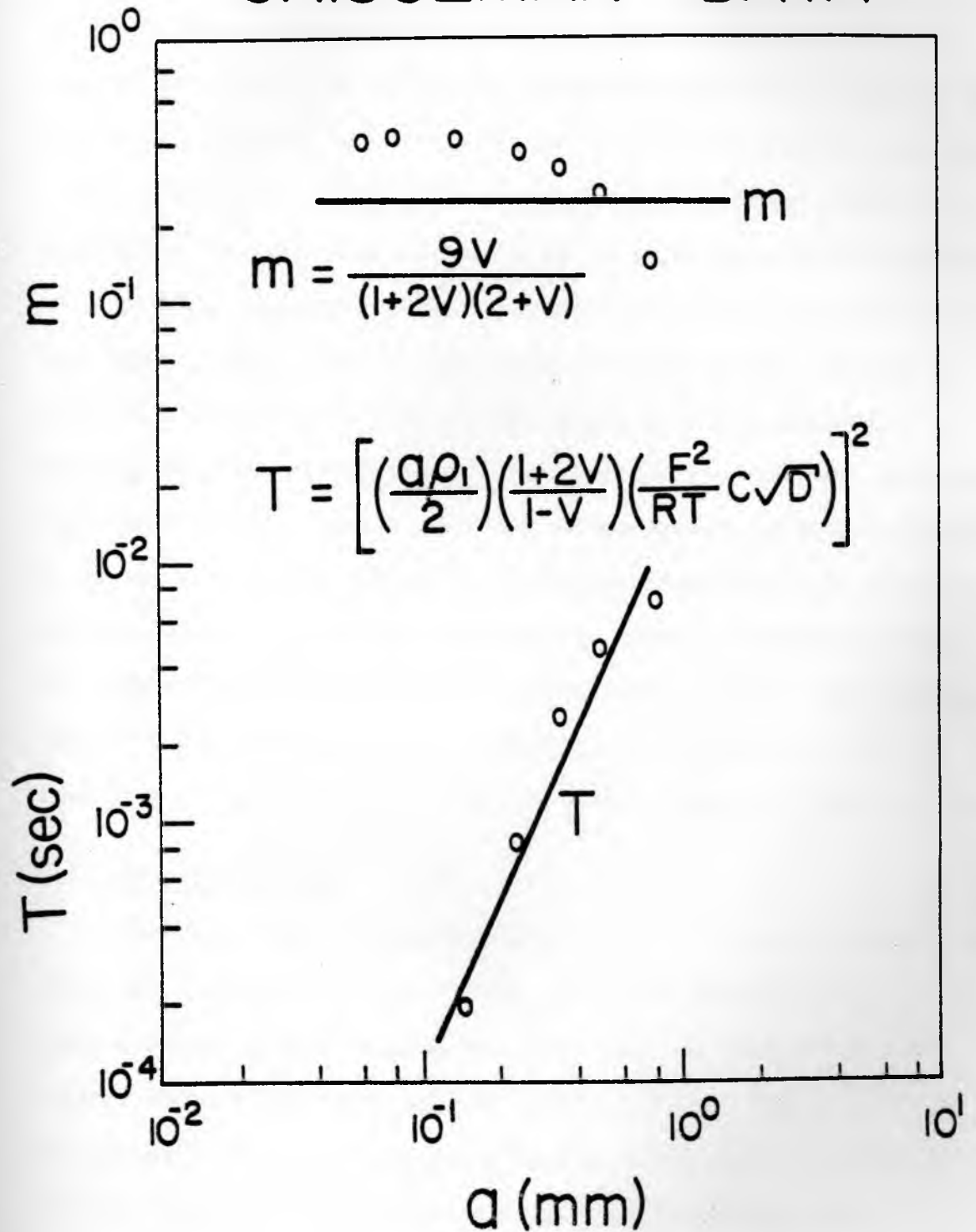
is in approximate agreement with the theoretical model (equation 2-29). The degree of polarization observed in the synthetic samples indicate that V (or m) depends on the volume fraction (V") of the mineral particles, the resistivity contrast between the mineral (ρ_3) and the electrolyte, and not on grain size related variables such as total surface area. Grain size ranges thought to be well known were applied to the inversion parameters A/a to obtain reasonable estimates of the Warburg impedance at $\omega=1$. However since grain size can easily vary over several orders of magnitude, the grain radius (a) must be precisely known within a very narrow range to afford comparable Warburg impedance calculations. The Cole-Cole time constant obtained from the synthetic samples exhibited an approximate dependence on the grain radius squared. Since τ is inversely proportional to frequency then the square root of the difference in order of magnitude between the frequencies at which prominent phase peaks occur (or the frequency limits of the width of a broad dispersion) in IP spectra, could be used as a crude estimate for relative range of possible length scales.

4.4 Warburg Impedance

Since the Warburg impedance (A, $\omega=1$) of pyrite was observed to be some what independent of grain size for a given electrolyte concentration, then by knowing the grain size, calculation of other mineral Warburg impedances appears to be possible. Table 4.4 lists the inversion results of synthetic samples containing (V' = .085, V" .16) chalcopyrite, galena, pyrite, copper metal, graphite and molybdenite. These samples are all saturated with 1 Ωm electrolyte

Table 4.4 Sample statistics and inversion results for synthetic
samples containing various conductive minerals. The observed IP
spectra for samples pyrite (H), pyrite (I), chalcopyrite (I) and
copper metal are shown in figures 4.4 (H10), 4.7, 3.2, and 5.3 (C1)
respectively. These samples were saturated with $1\Omega m$ electrolyte
(NaCl).

COMPOSITION	GRAIN RADIUS	VOL.FRAC.		PORO-SITY	INVERTED PARAMETERS				WARBURG IMPEDANCE (Ω-m^2)		
		V'	V"	ϕ_e	V	ρ_i Ω-m	C	A/a Ω-m	$A_{min.}$	$\bar{A}$	$A_{max.}$
CHALCOPYRITE	H	.09	.15	.29	.138	15.5	.668	1651	.486	.725	.964
CuFeS$_2$	I	.09	.16	.26	.127	14.2	.671	568	.332	.450	.568
GALENA	H	.09	.16	.27	.114	11.5	.648	918	.270	.403	.536
PbS	I	.09	.16	.27	.126	12.3	.640	525	.306	.416	.525
PYRITE	H	.09	.17	.14	.068	24.1	.512	683	.201	.300	.399
FeS$_2$	I	.09	.16	.16	.073	26.7	.512	318	.186	.252	.318
Cu METAL	H	.09	.16	.16	.158	19.57	.410	718	.212	.315	.419
GRAPHITE	H	.09	.18	.10	.362	34.0	.444	107	.032	.047	.062
	I	.08	.17	.10	.193	48.7	.504	175	.102	.139	.175
C	J	.09	.18	.10	.132	48.0	.502	115	.115	.173	.231
	K	.08	.16	.10	.079	47.6	.546	79.5	.159	.213	.266
MOLYBDENITE	G	.06	.10	.33	.087	13.5	.540	582	.102	.137	.172
MoS$_2$	H	.09	.14	.32	.113	12.3	.429	132	.039	.058	.077

(NaCl), contain cement, and have similar grain dimensions. The mean Warburg impedances ($\bar{A}$) calculated in this table do show a reasonable range of values for the electrolyte salinity (in comparison to mineral electrode measurements), with a general decrease in the magnitudes of the impedances from the top down. Apart from the degree of overlap observed between the impedance ranges of the different minerals, the entire range is mainly confined to a single order of magnitude. However if the inversion results (table 4.4) of two samples such as chalcopyrite (Cpy -H) and molybdenite (Mo-H) were compared with respect to the parameter A/a, one might expect sample Cpy-H to have a Warburg impedance an order of magnitude greater than that of Mo-H. This assumes of course a similar grain size and electrolyte ion concentration. If the grain size is also known for each sample, discrimination between the minerals in each may be possible. Since grain dimensions of minerals (and possibly the electrolyte resistivity) can vary over many orders of magnitude in natural environments, this method of mineral discrimination necessitates a precise knowledge of the dominant mineral dimensions (and the electrolyte resistivity). Obviously if the grain size is known there are more conclusive methods of mineral identification than the one presented here. However if the opposite approach is taken, where some average value for the Warburg impedance is assumed (for a given electrolyte ion concentration), the parameter A/a may be helpful in estimating a possible range of mineral grain sizes.

4.5 Frequency Dependence of the Electrode Impedance

Figure 4.13 shows the distribution of the inversion parameter c, representing the frequency dependence of the electrode impedance (or phase angle slope), for 52 samples which contained a limited range of grain sizes. The distribution shows a range of values between .3 and .7 with a mean of .51. This mean agrees well with the theoretical expectations for an ideal Warburg frequency dependence of c= .5. The rather large standard deviation however indicates that a significant amount of samples show a non-ideal Warburg dependence.

Assuming that a frequency dependence of 0.5 dominates over the measured frequency range, phase slopes less than 0.5 might simply be obtained by increasing the range of grain sizes or length scales within the sample so that a summation of spectra each having phase angle slopes of 0.5, results in smaller slopes. A sample containing the two different grain sizes B and M produced a phase spectra with two distinct peaks of comparable magnitude, each having slopes near 0.5. Two Cole-Cole dispersions fit to this data resulted in the two Warburg impedance values as plotted in figure 4.10 (open circles). Note that similar values were obtained as for the samples containing only one grain size range (B and M). Sample series D (table 4.2) are suspect to inhomgeneities resulting in larger length scale ranges. As the volume fraction increases this range might be expected to increase and the values of c are observed to decrease as the volume fraction increases. Similarly, samples D-A (figure 4.7, table 4.3) are liable to inhomogeneities, causing increased length scale ranges and these samples do exhibit low slope values.

Figure 4.13 Distribution of the inversion parameter c obtained for the majority of synthetic samples in this report containing a limited range of grain sizes.

DISTRIBUTION OF PARAMETER C

TOTAL NUMBER OF SAMPLES = 52
MEAN = .51
STANDARD DEVIATION = .08
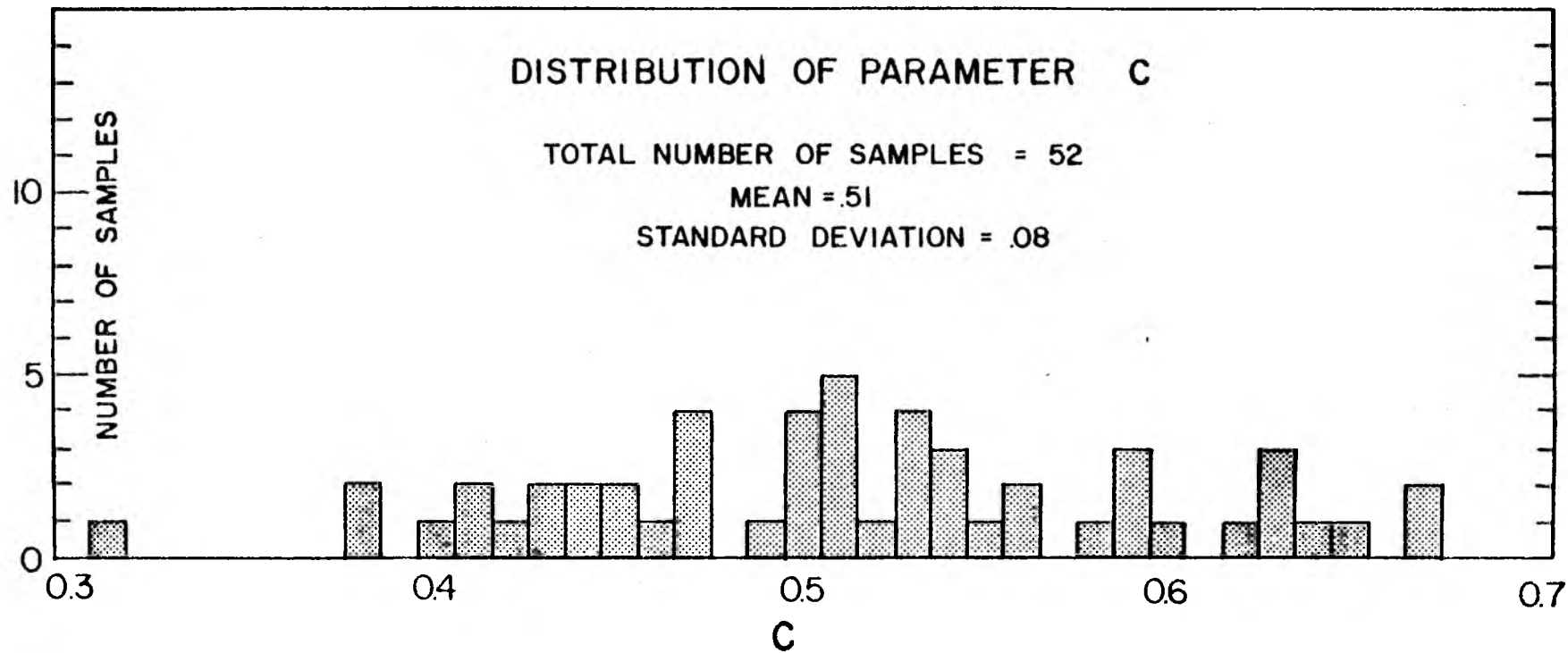
Modeling of summation spectra indicated that a log normal distribution of volume fractions which total to $\Sigma V_i = 0.1$, necessitated a length scale range of four orders of magnitude (e.g. log range 1 to 4) to obtain a slope of 0.25. Equal volume fractions necessitated a range of only two orders of magnitude to obtain a similar slope.

On the basis of these examples and modeling results the small phase angle slopes, often observed in field measurements, maybe an indication of the range of length scales within the deposit.

Amplitude and phase measurements on pyrite electrodes are shown in figure 4.14 and represent an observe electrode impedance function over the measured frequency range. Between .01 and 1.0 hz the amplitude spectrum displays a slope of .48, indicating a diffusion (Warburg, c=.5) controlled impedance. Between 1.0 and 1K hz the slope steepens to .84 indicating a capacitive (double layer) frequency dependence (ideal, c= 1.0). Above 1K hz the amplitude curve asymptotes due to the resistance of the double layer capacitance becoming less than that of the electrolyte (here ρ_e 1 Ωm, $|Z| \approx 10 \ \Omega$) between the two pyrite electrodes. Therefore over the measured frequency range the pyrite electrode impedance shows two rather different frequency dependencies. With respect to the theoretical model the general electrode impedance function is represented by $\frac{A}{(j\omega)^c}$. This form of representation only accounts for one type of frequency dependence and therefore a more complicated electrode impedance function may be appropriate (e.g. Madden and Marshall, 1959).

Figure 4.14 Amplitude and phase angle spectra of the impedance of two pyrite electrodes separated by 5mm of $1\Omega m$ electrolyte (NaCl). The Warburg impedance at $\omega = 1$ is $.59\Omega m^2$ for a single interface.

IMPEDANCE OF TWO
PYRITE ELECTRODES

(0.1 M NaCl SOLUTION)
AREA 4.4 cm²
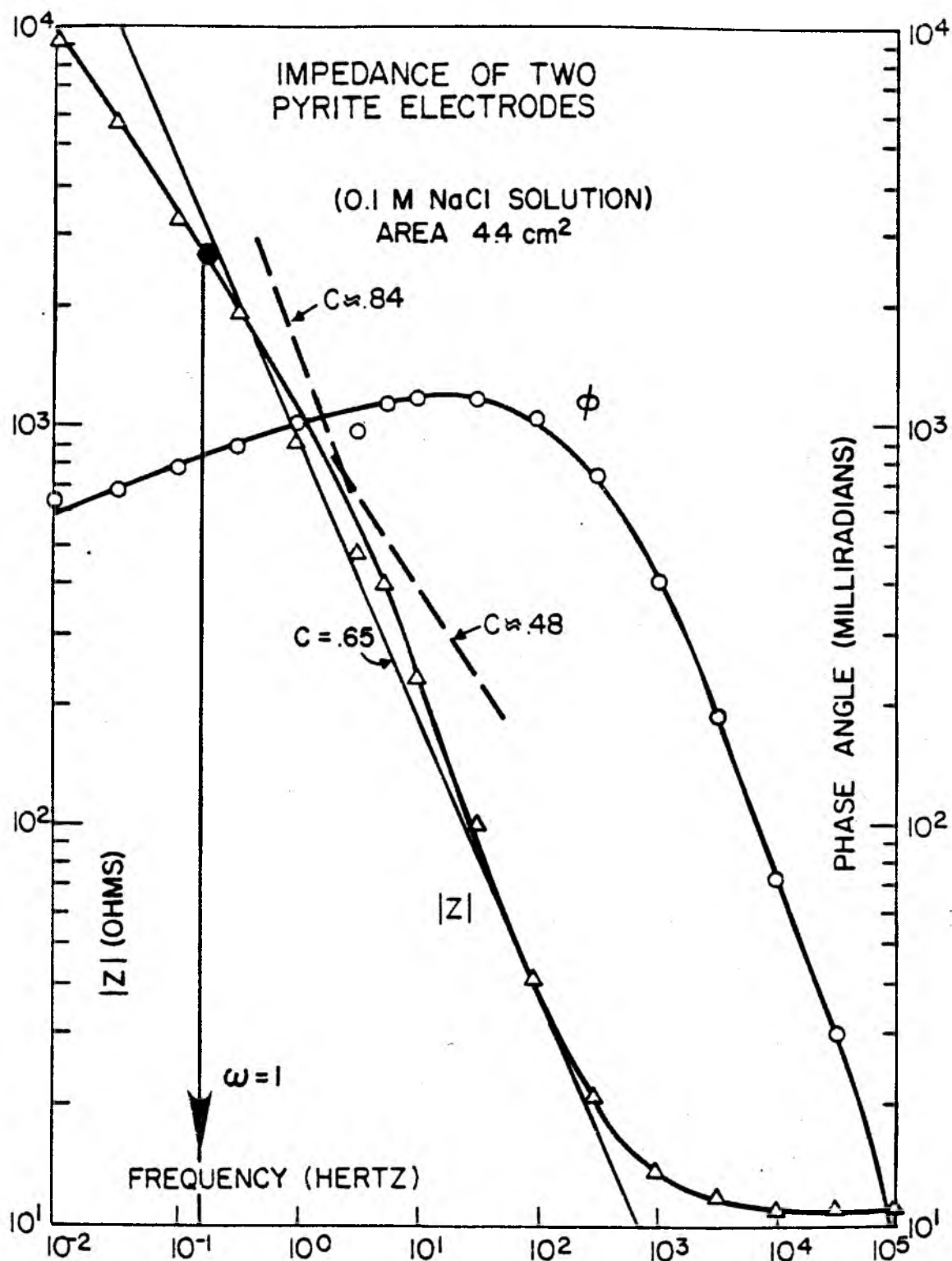
In figure 4.14 note that the amplitude data ($\Delta < 10^3$hz) can be approximately fit to a straight line with some average slope between 0.5 and 0.8 (e.g. $\bar{c}$ = .65). This suggests the electrode impedance function given by equation (2-5) can be a reasonable approximation and that resolving a more complex model is beyond the capability of most synthetic rock IP data (i.e. due to the summation effect of different length scales).

Because the two frequency dependencies (c= .5, .8) each dominate over a certain frequency range, the dispersive region of the synthetic samples at low frequencies (e.g. .01 to 1.0 hz) might be expectd to produce inversion results of c near 0.5, while those that occur at higher frequencies might be expected to approach 0.8. This type of trend is observed in the data obtained from the variable grain size sample E-M and C'.

As the grain size was decreased (figure 4.7, table 4.3), shifting the dispersive region to higher frequencies, the inversion parameter c is observed to increase from around 0.5 to 0.6. A similar trend is observed as the electrolyte resistivity is decreased for the sample H series (figure 4.1, table 4.1). Note that the average frequency dependence of series H was estimated to be around .66 (figure 4.2) which is in excellent agreement with the anticipated $\bar{c}$ = .65, as discussed above. Chalcopyrite and galena samples (figure 3.2, table 4.4) whose dispersive regions occur at higher frequencies also show slopes of around 0.6 to 0.7.

With respect to the resolving power of the IP data, the observed character of the electrode impedance with frequency (figure 4.14), and

the trends in c observed for the synthetic rock data, the general electrode impedance function given in equation (2-5) is an adequate representation in the model. The asymptotic slope of the phase angle spectra of synthetic rocks is a function of the frequency dependence of the electrode impedance and the range of length scales oriented parallel to the applied electric field. For a limited length scale range, the phase angle slope is approximately equal to the dominant or average frequency dependence of the elctrode impedance, which was observed to vary betwen 0.5 and 0.8. Phase angle slopes less than 0.5 are a result of a summation of IP spectra (c = .5 -.8) produced by a large range of length scales within the sample.

CHAPTER 5

PARTICLE SHAPE

5.1 Theoretical Ellipsoidal Models

To investigate the effect of particle shape on IP spectra a layered ellipsoid model is developed for both parallel and random orientations. In the special case of a sphere figure 2.1 shows the three regions representing a single ellipsoid of conductivity σ_3, with a thin surface layer (σ_2) embedded in some background medium (σ_1). This three component boundary value problem is solved in the fashion of section 2.1, however in an elliptical coordinate system. The coefficient of the dipole term for the electric potential exterior (i.e. region 1) to ellipsoids, oriented parallel to the electric field is (Sill, 1977, personal communication)

$$B_1 = \frac{\alpha\beta\gamma}{2}\left[\frac{1 - \dfrac{\sigma_2 i^2}{\sigma_1 \sigma t}}{1 + \dfrac{\alpha\beta\gamma}{2}I_i\left(\dfrac{\sigma_2 i^2}{\sigma_1 \sigma t} - 1\right)}\right] \quad , \quad (5-1)$$

where $t \ll \alpha,\beta,\gamma$ and

$$i = \text{axis parallel to } \vec{E}(\alpha \geq \beta \geq \gamma) \quad , \quad (5-2)$$

$$I_i \equiv \frac{\alpha\beta\gamma}{2}\int_0^\infty \frac{d\lambda}{(i^2+\lambda)\Delta\lambda} \quad , \quad (5-3)$$

$$\Delta\lambda = \sqrt{(\alpha^2+\lambda)(\beta^2+\lambda)(\gamma^2+\lambda)} \qquad . \qquad (5\text{-}4)$$

I_i is the definite elliptic integral describing the depolarization factor of each axis. In the case of a sphere $I_i = 1/3$ and equation (5-1) reduces to the coefficient of dipole term in equation (2-2). However it has been assumed here that $\sigma_3 >> \sigma_1$ to imply maximum polarization. At this point a Maxwell appraoch (figure 2.2) could be applied to equation (5-1) for determining the net effect of a distribution of layered ellipsoids. However theoretical mixing formulas for nonspherical particles, derived mainly for mixtures of dielectrics, are given extensively in the literature. Although these formulas are usually for two component systems, by comparing the coefficient of the dipole terms exterior to the suspended particles to equation (5-1), they can easily be extended to include a thin surface layer around the particles.

For example Fricke (1953) gives an excellent discussion on the mathematical treatment of the electrical conductivity of dispersed systems. Specifically he derives the coefficient of the dipole term for the potential in the suspending medium (σ_1) exterior to a single ellipsoid (σ_2) oriented parallel to the electric field as

$$D = \frac{\alpha\beta\gamma}{2}\left[\frac{1 - \dfrac{\sigma_2}{\sigma_1}}{1 + \dfrac{\alpha\beta\gamma}{2} I_i \left(\dfrac{\sigma_2}{\sigma_1} - 1\right)}\right] \qquad . \qquad (5\text{-}5)$$

As can be seen the exterior coefficient of the dipole terms D and B_1, for the two and three component systems are similar and can be compared to each other through

$$\frac{\sigma_2}{\sigma_1} \rightarrow \frac{\sigma_2 i^2}{\sigma_1 \sigma t} = \frac{i^2 (jw)^c}{\sigma_1 \sigma A} \qquad . \qquad (5\text{-}6)$$

Note that an electrode admittance function $(g_2 = \frac{\sigma_2}{t})$ has been equated to $\frac{(j\omega)^c}{A}$ in the second part of equation (5-6), to account for the frequency behavior of the diffuse zone between the eletrolyte and the conductive ellipsoid.

Fricke (1953) derives several mixing formulas describing the Maxwell-Wagner dispersion in a suspension of ellipsoids. For high concentrations of parallel conductive ellipsoids (Fricke, 1953)

$$\sigma = \sigma_1 \left[\frac{\frac{\sigma_2}{\sigma_1} + X_i + X_i V(\frac{\sigma_2}{\sigma_1} - 1)}{\frac{\sigma_2}{\sigma_1} + X_i - V(\frac{\sigma_2}{\sigma_1} - 1)} \right] \qquad (5\text{-}7)$$

and for random orientations

$$\sigma = \sigma_2 + \frac{(\sigma_1 - \sigma_2)(1 - V)}{1 + \frac{V}{3} \sum_{i=\alpha,\beta,\gamma} \frac{\sigma_1 + \sigma_2}{\sigma_2 + X_i \sigma_1}} \qquad (5\text{-}8)$$

The form factors (X_i) are related to the depolarization factors (I_i) by

$$x_i = \frac{1 - I_i}{I_i} \qquad , \qquad (5\text{-}9)$$

where both X_i and I_i have been tabulated in the literature, Fricke (1959) and van Beek (1967) respectively for various axial ratios. Note that for spherical particles of radius α, $x_\alpha = 2$ and equation (5-7) reduces to the same form of equations (2-11) and (2-19) derived for the net effect of a distribution of layered spheres in chapter 2.

To assess any highly correlated ellipsoidal parameters it is convenient to rearrange the random and parallel orientation models

into the form of Cole-Cole models. First equation (5-6) is substituted into the parallel and random orientation models given by equations (5-7) and (5-8) respectively to incorporate the frequency dependence of the diffuse layer. As frequency goes to zero and infinity, the low and high frequency resistivity asymptote (ρ_o and ρ_∞) and the chargeability (m) of the Cole-Cole model for parallel orientations become

$$\rho_o^P = \rho_1 \frac{(x_i + V'')}{x_i(1 - V'')} \quad , \quad (5\text{-}10)$$

$$\rho_\infty^P = \rho_1 \frac{(1 - V'')}{(1+x_i V'')} \quad , \quad (5\text{-}11) \; .$$

$$m_i^P = \left[1 - \frac{x_i(1-V'')^2}{(1+x_i V'')(x_i+V'')} \right] \quad , \quad (5\text{-}12)$$

where i (α, β, γ) is the axis parallel to $\vec{E}$. For random orientations

$$\rho_o^R = \rho_1 \left[\frac{1 + \frac{V''}{3} \sum_{i=\alpha,\beta,\gamma} \frac{1}{x_i}}{(1 - V'')} \right] \quad , \quad (5\text{-}13)$$

$$\rho_\infty^R = \rho_1 \left[\frac{(1 - V'')}{1 + \frac{V''}{3} \sum_{i=\alpha,\beta,\gamma} x_i} \right] \quad , \quad (5\text{-}14)$$

$$m^R = \left[1 - \frac{(1 - V'')^2}{(1 + \frac{V''}{3} \sum_{i=\alpha,\beta,\gamma} \frac{1}{x_i})(1 + \frac{V''}{3} \sum_{i=\alpha,\beta,\gamma} x_i)} \right] \quad . \quad (5\text{-}15)$$

The superscripts P and R denote parameters which are derived from

parallel and random orientation models. Note that V" (equation 4-5) has been used for the volume fraction based on observations in section 4.1 and that for maximum polarization, $\rho_3/\rho_e = 0$. While the concentrated parallel orientation model can be easily rearranged into the form of a single Cole-Cole dispersion to isolate the time constant as

$$\tau_i^p = \left[\frac{(1+x_i V") \; \rho_1 i^2}{x_i (1-V") A\alpha} \right] \qquad , \qquad (5\text{-}16)$$

the concentrated random orientation model is more complicated and does not appear to have a simple equivalent summation of Cole-Cole dispersion with respect to the time constants.

Fricke (1959) also gives a low concentration model for random orientations of ellipsoids for which he indicates the electrical behavior of such a suspension can be represented by a uniform mixture of the three principle axis orientations of the ellipsoids. Also by expanding the high concentration model (equation 5-8) into a series solution by assuming low volume fractions the small volume fraction terms drop out, and the high concentration model reduces to Fricke's (1959) low concentration model. The form of this low concentration model can be rearranged into a summation of Cole-Cole dispersions, one for each principle axis. However the synthetic samples are considered to have a high concentration (i.e. V" > 0.1) of particles so that low concentration models are theoretically inappropriate.

Therefore to analyze the observed IP spectra obtained from the synthetic samples constructed to test the random orientation model a simple Cole-Cole model with multiple dispersions is given as

$$\rho^*_{RANDOM} = \rho_0 \left[1 - m_\alpha(1 - \frac{1}{1+(j\omega\tau_\alpha)^c}) \right]\left[1 - m_\beta(1 - \frac{1}{1+(j\omega\tau_\beta)^c}) \right]$$
$$\left[1 - m_\gamma(1 - \frac{1}{1+(j\omega\tau_\gamma)^c}) \right] \qquad . \qquad (5\text{-}17)$$

The inversion results obtained from this Cole-Cole model will then be compared to the various high concentration forms of the chargeability (m^R) and time constants τ_i^p given in equations (5-15) and (5-16) respectively, to see if low concentration theory can be extended to higher concentrations. For high concentrations of parallel ellipsoids the equivalent Cole-Cole model becomes

$$\rho^*_{PARALLEL} = \rho_0^p \left[1 - m_i^p(1 - \frac{1}{1+(j\omega\tau_i^p)^c}) \right] \qquad , \qquad (5\text{-}18)$$

where ρ_0^p, m_i^p and τ_i^p are given by equations (5-10), (5-12) and (5-16) respectively. Note that the frequency dependence (c) is not subscripted in the models since it will generally be set to 0.5 for a simple Warburg diffusion impedance.

The time constants for parallel orientations (equation 5-16) are proportional to a length scale $(\frac{i^2}{\alpha})$ squared for a simple Warburg diffusion impedance, in similar fashion as the spherical model (i.e. α^2, equation 2-33). Although the time constants are weighted by form factors (x_i), for similar spherical and minor ellipsoidal axis parallel to the electric field the time constant expressions are of comparable magnitude.

Figures 5.1 and 5.2 show a family of curves (m vs V) for parallel and random orientations chargeabilities at various axial ratios $i(\alpha,\beta,\gamma)$.
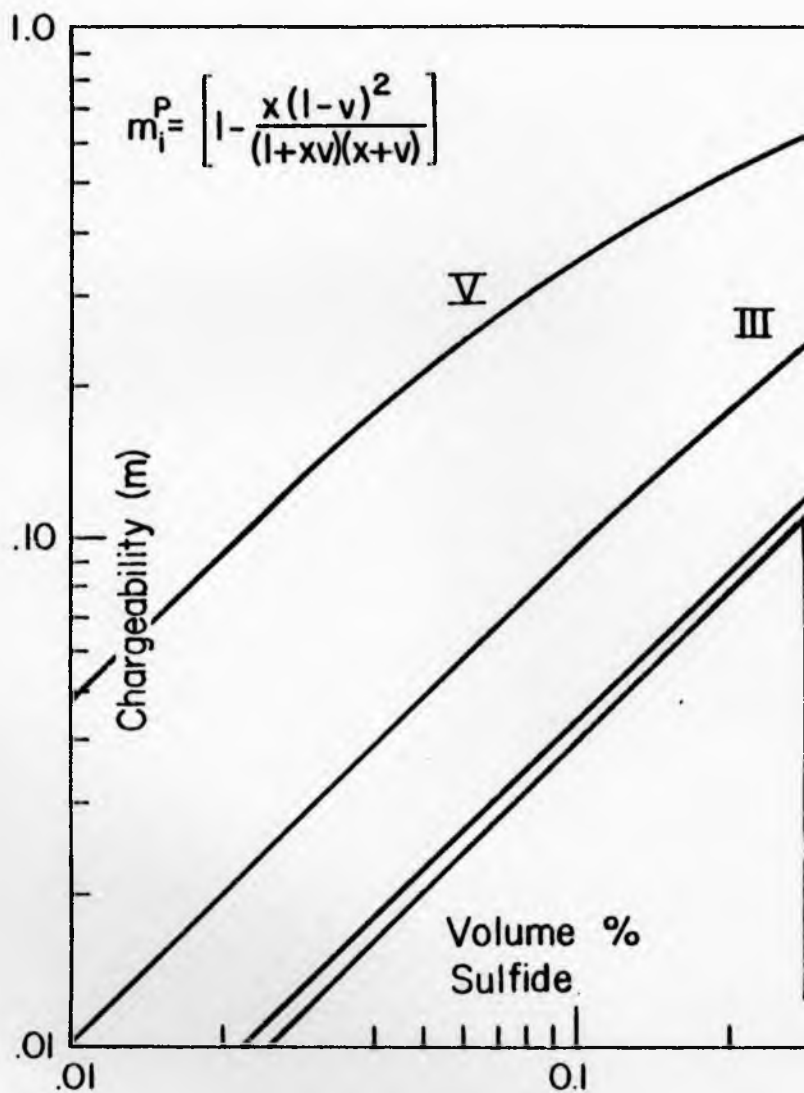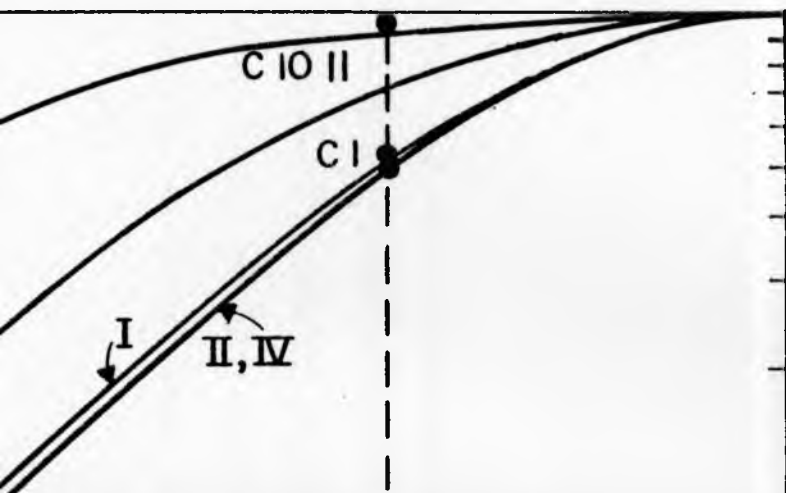
The form factors (χ_i) in figure 5.1 are the same as those used in figure 5.2. The data points shown in these figures are obtained from the inversion results from a suite of synthetic samples containing copper wire cut into various lengths. The agreement between the theoretical and observed chargeabilities will be discussed in detail in section 5.2.

For a given volume fraction (e.g. V" = .16) in figure 5.1, as the ellipsoids begins to elongate in the direction of the electric field the chargeability increases (e.g. to curves II and V). In this parallel particle orientation, charge can be separated a greater distance which gives rise to larger dipole moments and therefore greater chargeabilities. Figure 5.2 (random orientations) shows a similar trend, however to a lesser extent due to the smaller charge-abilities resulting from a portion of the ellipsoids having their minor axis (β or γ) aligned parallel to the electric field. As the volume fraction increases in both figures 5.1 and 5.2, the chargeability curves increase in a linear fashion in log-log space until about V=.2, at which point all the curves converge to m=1 at V=1.0.

Note that for parallel orientations (figure 5.1) curve I (sphere), II and IV (ellipsoid along short axis) are almost identical. Also for the random orientations (figure 5.2), curve I (sphere) and curve II (3:1:1) are close to each other for the entire volume percent range. Due to the apparent inability of IP data to resolve more than four basic parameters, the similarity between some of the theoretical chargeability curves indicates that a simple spherical model (with

Figure 5.1 Plot of chargeability (equation 5.12) versus the volume
percent for various principle axis $i(\alpha,\beta,\gamma)$ orientations of ellipsoids
in an applied electric field. The observed chargeabilities plotted in
this figure are obtained from synthetic samples containing copper
rods, whose inversion results are shown in figure 5.4.

Curve Number	Axial Ratio $\alpha:\beta:\gamma$	Axis Parallel to E Field	FORM X_i FACTOR
I	1:1:1	α or β or γ	2.0
II	3:1:1	β or γ	1.2
III		α	8.2
IV	10:1:1	β or γ	1.06
V		α	48.3

10   16   100

Figure 5.2 Plot of chargeability (equation 5-15) versus the volume
percent for random orientations of ellipsoids of various axial ratios
i(α:β:γ). The observed chargeabilities plotted in this figure are
obtained from synthetic samples containing copper rods, whose
inversion results are shown in figure 5.4. Form factors (X) are shown
in figure 5.1.

$$m^R = \left[1 - \frac{(1-v)^2}{(1+\frac{v}{3}\Sigma\frac{1}{x})(1+\frac{v}{3}\Sigma x)} \right]$$

Chargeability (m)

III

II

I

Volume % Sulfide

Random Orientation	
Curve Number	Axial Ratio $\alpha : \beta : \gamma$
I	1 : 1 : 1
II	3 : 1 : 1
III	10 : 1 : 1

CIOR

C3R, CI

10   16   100
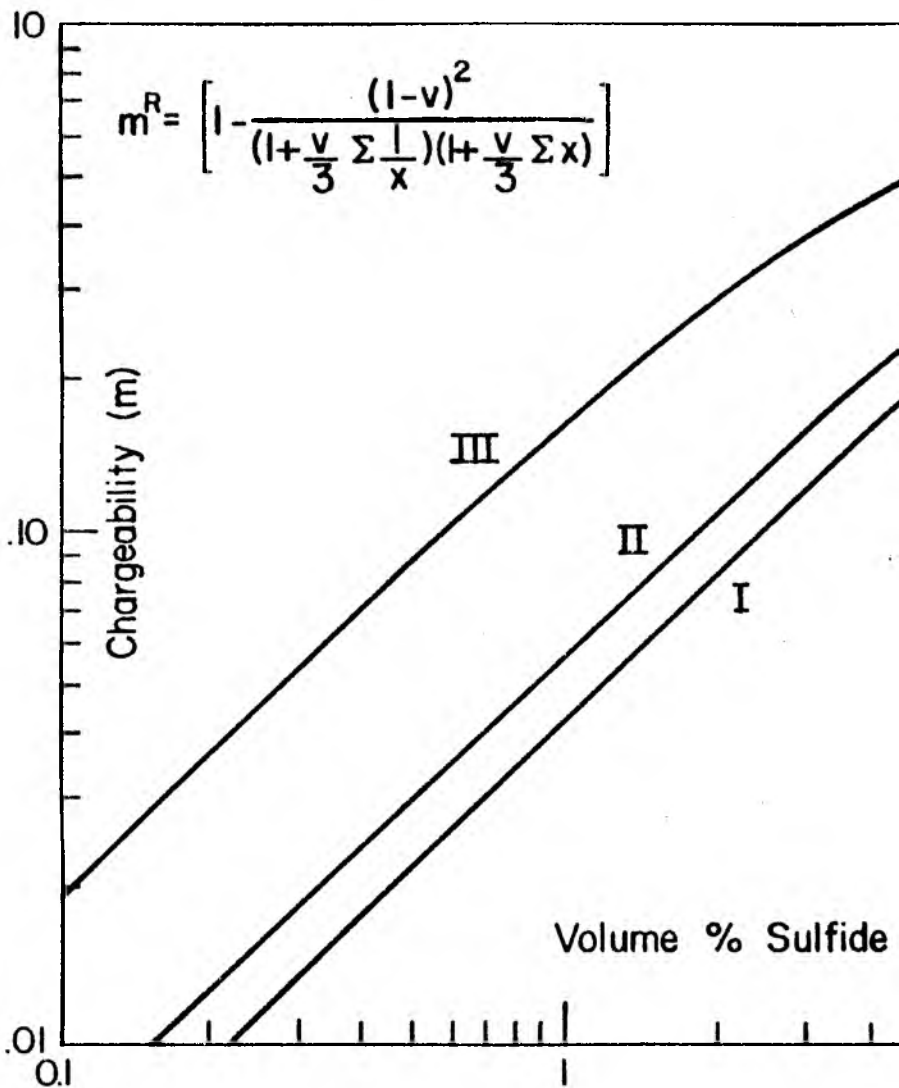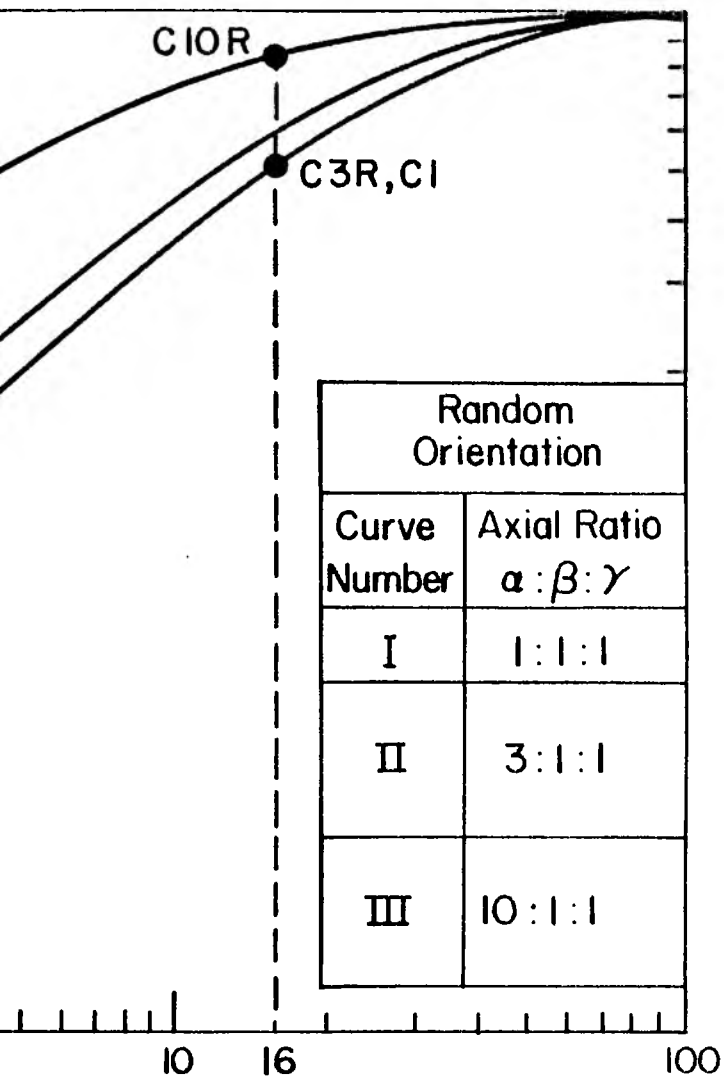
respect to m) would have a difficult job of distinguishing between the indicated particle configurations and volume fractions (i.e. figure 5.1; I, II, IV: figure 5.2; I, II). These particular chargeability curves represent a fairly wide range of sample configuration from spherical (1:1:1) to ellipsoidal particles of (10:1:1) axial ratios. This range might in some cases reasonably approximate natural mineralized environments, such as disseminated type deposits, veined deposits having preferred orientations (e.g. figure 5.1, IV), or veined deposits of axial ratios (3:1:1) having random orientations (e.g. figure 5.2, II).

Therefore since the ellipsoidal models have time constants of similar form (and in some cases similar magnitude) to the spherical model and theoretical indications are that m(elliptical) may be approximated by the spherical model chargeability for a range of ellipsoidal orientations, it appears impractical at this point to apply a more complex model than spherical to observed IP spectra. For example as in the spherical model where ρ_3/ρ_e was highly correlated with V", the form factors (X_i) in the ellipsoidal model would also be highly correlated with these parameters (see equation 5-12 and 5-15). Although some estimates of ρ_3/ρ_e and V" might be attempted in in situ measurements, estimates of three form factors for distributions of particle orientation could be very misleading. Therefore any advantages that might be gained in using an ellipsoidal inversion model would be negligible when compared to the spherical model, which appears in some cases to reasonably approximate nonspherical conditions. This assumes of course a spherical model representation

of τ (equation 2-33) can adequately represent nonspherical conditions. Observations from the synthetic samples appear to be in favor of this up to a point. In anticipation of a spherical model being able to adequately represent some nonspherical sample conditions the ellipsoidal models are left in terms of a general Cole-Cole model (i.e. τ and m). Then any similarities between the spherical model and the ellipsoidal model can be easily assessed.

5.2 Observations and Results

Figures 5.3 and 5.4 show the observed data in real and imaginary resistivity, and corresponding sample geometry (in similar figure positions) for five samples all containing (V' = .085, V"=.16) copper wire (1mm dia.) cut into various lengths (1mm, 3mm, 10mm). The position of the imaginary resistivity peak is indicative of the time constant and the IP spectra have been plotted in this manner to facilitate the analysis. These samples are saturated with 1 m electrolyte (NaCl) and contain cement to reduce the porosities to around 14%. Therefore note that V" has been calculated via equation (4-6). The smooth curves (figure 5.3) are the theoretical Cole-Cole models (equation 5-17 and 5-18) fit to the data. The numbers in parenthesis (figure 5.4) are the theoretical predictions (equations 5-12 to 5-15 and 5-16) based on the polarization of layered triaxial ellipsoids.

The axial ratios and form factors are given in figures 5.1 and 5.2. The axial dimensions are given in table 5.1 along with the volume fractions V". The background resistivity (ρ_1 =25Ωm) is

Figure 5.3 Real (ρ') and imaginary (ρ'') resistivity for synthetic samples containing quartz sand, cement, and copper rods of various lengths and orientations. The samples were saturated in 1 m electrolyte (NaCl). The smooth curves are the actual theoretical Cole-Cole model (equations 5-17 and 5-18) fit to the data. The Cole-Cole model inversion results and sample geometry are shown in figure 5.5. Spherical model inversion results and sample statistics are listed in table 5.1.

COMPLEX RESISTIVITY
'PARTICLE SHAPE'
AXIAL RATIO OF
COPPER ROD

SAMPLE	α	β	γ
CI	1 :	1 :	1
C3	3 :	1 :	1
CIO	10 :	1 :	1
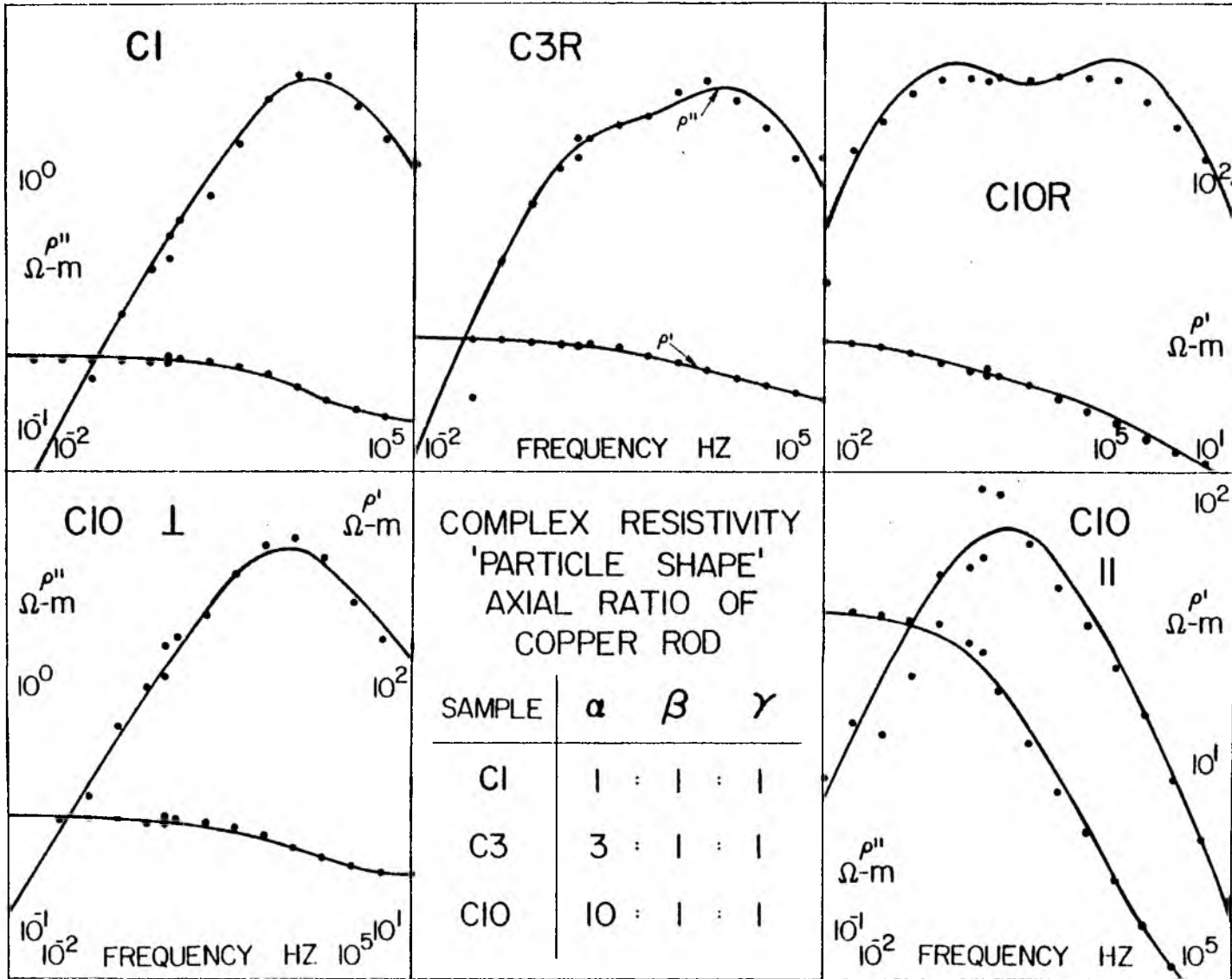
Figure 5.4   Sample geometry and Cole-Cole inversion results (τ and m) for synthetic samples containing copper rods of various lengths and orientations. The observed IP spectra for these samples are shown in figure 5.3.

$\tau = 8.40 \times 10^{-5}$

(9.7×10^{-6})
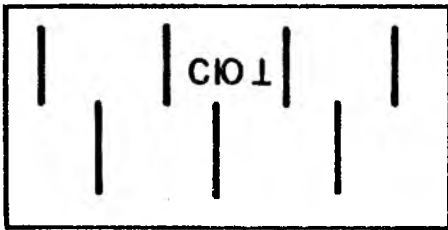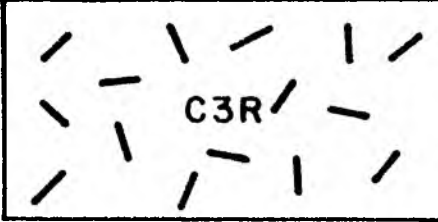
$\tau_\beta = 5.00 \times 10^{-5}$ $m_\beta = .346$

(1.9×10^{-4})

$\tau_\alpha = 1.45 \times 10^{-2}$ $m_\alpha = .127$

(4.9×10^{-4})

$\tau_\beta = 1.40 \times 10^{-4}$ $m_\beta = .564$

(2.2×10^{-5})

$\tau_\alpha = 1.71 \times 10^{-1}$ $m_\alpha = .294$

(9.6×10^{-4})

$m^R = .501 \ (.51)$ $m^R = .473 \ (.59)$ $m^R = .858 \ (.83)$

$\tau_\beta^p = 2.48 \times 10^{-4}$

(2.7×10^{-5})

$m_\beta^p = .469 \ (.48)$
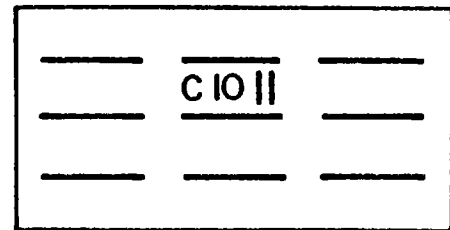
$\tau_\alpha^p = 1.28 \times 10^{-2}$

(7.3×10^{-3})

$m_\alpha^p = .971 \ (.92)$

estimated from a cement blank (figure 3.3) and the Warburg impedance

of copper metal is estimated at $.3\Omega$ m^2 as indicated by the inversion

results from sample Cl (table 4.4). Since these samples contain

copper metal particles and $1\Omega m$ electrolyte maximum polarization can be

assumed (i.e. $\frac{\rho_3}{\rho_e} \approx 0$).

In the analysis of the observed data it will be convenient to

compare the square root of the ratio of the time constants to indicate

length scale differences between different samples or a sample showing

two or more dispersions. A simple Warburg impedance (i.e. c=.5) is

assumed and for convention the smaller time constant $\tau(S)$ will be

divided into the larger time constant $\tau(L)$ to maintain a ratio of one

or greater. Three such ratios will be compared which are calculated

from equations (5-11) to 5-13) and designated as

1. Observed

$$\sqrt{\frac{\tau(L)}{\tau(S)}} = OR \qquad . \qquad (5\text{-}19)$$

2. Spherical model

$$\sqrt{\frac{i(L)}{i(S)}} = SR \qquad . \qquad (5\text{-}20)$$

Note in this spherical model approximation to nonspherical

particles i is the length scale (α, β, γ) parallel to the electric

field (i.e. assumed to be the radius of a sphere) and all other

terms in equation (2-33) cancel.

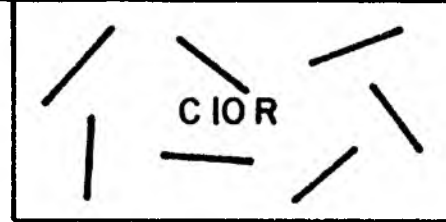Table 5.1 Sample statistics and inversion results using spherical model for synthetic samples containing copper rods of various lengths and orientations. The observed IP spectra in real and imaginary resistivity for these samples are shown in figure 5.3. The geometry of these samples are shown in figure 5.4.

Cu METAL SAMPLE	VOL. FRACT. v''	POROSITY ϕ_e	LENGTH SCALE RANGE (II TO $\vec{E}$) a (mm)	INVERSION PARAMETERS			
				ρ_1 Ω-m	V	A/a Ω-m	C
C 10 $\perp$	.16	.16	0.5	30.5	.144	646	.402
C I	.16	.16	0.5	19.6	.158	718	.410
C 3R	.17	.11	0.5 - 1.5	24.3	.139	355	.388
C 10 R	.17	.13	0.5 - 5.0	18.6	.313	108	.294
C 10 II	.16	.14	5.0	8.51	.702	218	.470

3. Ellipsoid Model

$$\frac{(1 + x_{i(L)}{}^{V''})i(L)^2}{x_{i(L)} \; \alpha(L)} \Bigg/ \frac{(1 + x_{i(S)}{}^{V''})i(S)^2}{x_{i(S)}{}^{\alpha(S)}} = ER \qquad . \qquad (5\text{-}21)$$

Note here that from equation (5-16) only the background resistivity (ρ_1), the Warburg impedance (A) and the term (1-V") cancel.

Therefore the $\sqrt{\tau}$ ratios SR, ER and OR which are close to unity will imply similar length scales between samples. Ratios greater than unity will imply different length scales between samples. This assumes of course that other parameters such as ρ_1, A and V" do not change significantly.

C1 is a sample containing equidimensional particles of copper and it shows an IP spectra (figure 5.3) similar to those obtained for the sulfide samples (sharp peaks and c $\approx$ .5). C10 $\perp$ is a sample containing copper rods having an axial ratio of 10:1, which are oriented perpendicular to the applied electric field (figure 5.4). Theoretically one might expect similar time constants and chargeabilities for both and in fact the two IP spectra are similar (figure 5.3). The theoretical chargeability $m_i{}^p$ equation (5-12) does a reasonable job of predicting the observed chargeability as seen by the data (m,V") plotted in figure 5.1 for samples C10$\perp$ and C1. Note also that the chargeabilities are indeed similar for these two samples. The $\sqrt{\tau}$ ratios (equations 5-19 to 5-21) indicating length

scale differences are SR = 1.0, ER = 1.7 and OR = 1.7. These ratios are all relatively close to unity suggesting similar length scales parallel to the electric field in both samples as is observed. While the ellipsoidal model seems to be in better agreement with the observed ratio, the spherical model ratio is comparable suggesting the feasibility of a spherical model approximation. However note that the observed and theoretical time constants (figure 5.4) for each sample (Cl and $C10\perp$) differ by a factor of ten in the same direction, which is not apparent when analyzing the $\sqrt{\tau}$ ratios. Assuming the model is correct, there appears to be an error in the estimates of ρ_1, A and/or c used in the theoretical calculation (equation 5-16). Since these are only rough estimates used in the theoretical calculations, the actual magnitudes of the predicted time constants should not be relied upon. However the relative magnitude of a time constant to other time constants does seem appropriate.

When the long axis of the copper rods (10:1) are oriented parallel to the electric field as in sample $C10\|$ (figure 5.4), a dramatic differnce is observed in the IP spectra (figure 5.3) relative to $C10\perp$ (also Cl). Due to the greater distance charge can separate in $C10\|$, the resulting larger dipole moments give rise to much greater chargeabilites. The theoretical chargeability m_α^p (equation 5-12) does a reasonable job of predicting the observed chargeability for $C10\|$ (see figures 5.1 and 5.4), which is about twice as large as that observed and/or theoretically predicted for $C10\perp$. The $\sqrt{\tau}$ ratios between sample $C10\perp$ and sample $C10\|$ are SR=10, ER=16 and OR=8.5. In this case the spherical model approximation (i.e. SR) appears to

agree more with the observed $\sqrt{\tau}$ ratio (OR). Note that a factor of 2.5 exists between the observed and theoretical time constant in figure 5.4 for $ClO_{\parallel}$. However the important point here is that the ratios (between $ClO_{\perp}$ and $ClO_{\parallel}$) all gave values much greater than unity, suggesting a large difference between length scales in these samples (i.e. relative to the measurement direction). Unlike the observed IP spectra for Cl and $ClO_{\perp}$, simple observation of the IP spectra for $ClO_{\parallel}$ and $ClO_{\perp}$ (figure 5.3) would indicate a significant difference between the two samples.

On the basis of the IP spectra for $ClO_{\perp}$ and $ClO_{\parallel}$, which show sharp peaks and slopes of about .45, a sample with random orientations (ClOR) would be expected to produce an IP spectra containing a range of time constants, one for each length scale. The summation of these spectra should produce broad maximum and slopes less than .45, and this is what was observed for ClO R (figure 5.3). The actual observed IP spectra showed a slope of about .29 and a broad flat peak roughly bracketed by the time constants obtained in samples $ClO_{\perp}$ and $ClO_{\parallel}$. The IP spectra labeled ClOR is the Cole-Cole model (equation 5-17) fit to the data with two time constants $(\tau_{\alpha}, \tau_{\beta})$ and chargeabilities (m_{α}, m_{β}), and the slope constrained by c=0.5. More dispersions could have been used to obtain a better fit, however to see if low concentration theory (see section 5.1) can be extended to the higher concentrations observed in sample ClOR (and C3R) only two dispersion are used, one for each principle axis (i.e. $i=\alpha, \beta=\gamma$). The two observed time constants for ClOR are similar to those obtained for $ClO_{\perp}$ and $ClO_{\parallel}$, and two dispersions do seem to approximate most of the

IP data. The $\sqrt{\tau}$ ratios for C1OR are SR=10, ER=6.6 and OR=35. Neither theoretical ratio is in agreement with the observed, however the fit of two dispersions to the IP spectra of C1OR is also a bit noisy. Note that due to the lower volume fraction (i.e. V"/3 for a uniform mixture) used to calculate τ_α associated with the long axis, its time constant is smaller than that calculated for C1O$_{\parallel}$. And the observed and calculated τ_α , for C1OR differ by a factor of around 200. Therefore the application of two dispersions to approximate the random conditions in C1OR seems to have some serious difficulties when interpreting the observed time constant through equation (5-11). However the $\sqrt{\tau}$ ratios being greater than unity, again indicate length scale differences within the sample. The chargeability m^R (equation 5-15) on the other hand, is in agreement with the sum of the observed chargeabilities ($m_\alpha + m_\beta$) for sample C1OR (see figures 5.2 and 5.4). C3R is also a random sample with copper rods of axial ratios of 3:1. A similar broad peak is observed (figure 5.3) over a narrower frequency range due to the smaller range of length scales. Two dispersions fit the data to within 10% error. The time constant ratios for C3R are SR=3, ER=1.6, and OR=17. As in C1OR neither theoretical ratio is close to the observed even though a better fit is observed using two dispersions. Although the observed and calculated $\sqrt{\tau}$ ratios differ for C3R, the observed ratio is greater than unity indicating length scale differences within the sample. Also note that the calculated ratios, SR and ER, are similar suggesting the theoretical possibility of a spherical model approximation to the nonspherical sample conditions of C3R. The chargeability m^R (equation

5-15) is in approximate agreement with the sum of the observed chargeabilities $(m_\alpha + m_\beta)$ for sample C3R (see figurs 5.2 and 5.4).

Although the calculated time constants (equation 5-16) do not accurately predict the observed time constants for the copper samples, the larger observed and calculated values are associated with the larger length scales. Also note that the observed time constants τ_β and τ_α (figure 5.4) for C10R and C3R correlate approximately with those observed for C1:C10$\perp$ and C1C$_\parallel$ respectively. The sum of the observed chargeabilities are in agreement with the theoretical values (figure 5.2) based on equation (5-15). These observations obtained through a summation of Cole-Cole dispersions suggest that equation (5-17) can do an approximate or relative job of estimating the random orientation model (high concentration) based on equations (5-7) and 5-8). This suggests that a uniform mixture of the three principle axis orientation can represent a high concentration of randomly distributed ellipsoids.

Other broad phase peaks were observed for some of the pyrite samples thought to be inhomogenious, especially the large volume fraction samples of small grain size D (not shown). In figure 4.7 note the second phase peak beginning to surface in the lower frequency ($\approx$ 30hz) phase data for sample A. This minor phase peak is approximately coincident with the phase peak of pyrite sample I. Since grain size I is about one hundred times greater than grain size A, this might suggest that one hundred grains (size A) are in electrical contact and effect an IP response similar to a single but larger grain size I. Although it is difficult to imagine one hundred

pyrite grains in electrical contact, with respect to the estimated half a billion pyrite grains in sample A it is not too unreasonable. In section 4.3 it was suggested that particles in electrical contact with one another can produce an effective dipolar field similar to those of larger particles. The similarity in phase angle spectra (i.e. broad peaks and small phase slopes due to a range of length scales) between samples A, C3R and C10R appear to be in agreement with this line of thought.

Although the theoretical model indicates that the form factors can have a large influence on τ, the observations from the synthetic copper samples suggest that the actual length scale parallel to the electric field is more dominant. The similarity between the time constants observed from samples C1, C10$_\perp$, C3R(τ_β) and C10R(τ_β) and the relative magnitudes of τ for samples C10$_\parallel$ and C10$_\perp$ suggest that a spherical model in reference to equation (2-27) might indeed be applied to some nonspherical sample configurations. The comparable magnitudes of the theoretical and observed chargeabilites for C1, C10$_\perp$ and C3R, also suggest the feasibility of a spherical model application.

5.3 Spherical Model Applications to Nonspherical Conditions

To investigate the feasibility of using a spherical model to approximate nonspherical conditions, a spherical inversion model (equation 2-29) was applied to the IP spectra from copper metal samples and the inversion results are listed in table 5.1. A single dispersion (i.e. one grain size of a given volume percent) is fit to

the IP data because unless separate dispersions occur (or indications of them) a summation of dispersions results in significant correlation between the different dispersion parameters (i.e. τ, m, and c). In order to work with summation spectra having low correlations between parameters, the frequency dependence c could be set to 0.5 for a simple Warburg frequency dependence and assumptions can be made as to the distribution of volume fraction (V or m) of each length scale (a) parallel to the electric field. This method indeed seems applicable to the IP spectra observed for C3R, C10R and sample A however such distinctive breaks in phase angle slope (suggesting different length scales) appear to be the exception to the rule in rock samples and field IP measurements. Therefore a single dispersion is used here to get an indication of the practical limits of a spherical model to give relevant information about nonspherical conditions which typically exist in natural environments.

The inversion result (table 5.1) obtained from the copper metal samples do show parameter trends which are reasonably explained in terms of a spherical model. The background resistivity (ρ_1) is in approximate agreement with equation (4-3), which accounts for the increase in sample conductivity due to surface conduction occurring in the cement (or "clay" type minerals). For example assume the effective cement conductivity in these samples is σ_s=1mho/m as sample C1 seemed to indicate in section 4.1. With σ_e=1 mho/m, the average porosity of ϕ_e= .14, and 1.8<M<2.1, then from equation (4-3)

$$\rho_1 = \frac{1}{\sigma_1} = \frac{1}{\phi_e^M(\sigma_e + \sigma_s)} = 17 - 31\Omega m \qquad , \qquad (5\text{-}22)$$

which is within range of the observed ρ_1 values obtained from samples C10$\perp$, C1, C3R and C10R (table 5.1). However $\rho_1 (=3.5\Omega m)$ for sample C10$\parallel$ is smaller than the predicted range and, in relation to the other samples shows a similar trend as when the volume fraction of pyrite was increased in sample suites H,J, and D (table 4.2). In reference to the second part of equation (2-20) used to calculate ρ_1 influenced by conductive mineral volume fractions, a V'=.2 would produce the observed ρ_1 of C10$\parallel$. A V' of .2 in these samples would result in V"=.3, which is not in agreement with the inversion parameter V=.7 or the observed value of V"=.16. Therefore it appears that axial ratios of 10:1:1 with their long axis oriented parallel to the electric field have exceeded the limits of a spherical model to give relevant information, especially with respect to the parameters ρ_1 and V.   Note also that C10R shows a larger V parameter of .31 which does not correspong with the observed V" (=.16).

However remember that for sample C1, the inversion parameter of V=.16 was in excellent agreement with its observed V"(=.16) and was considered to obtain maximum polarization. Note how samples C10$\perp$ and C3R produce comparable inversion results with respect to V(=.14). This similarity in the inversion and observed volume fraction (also ρ_1) suggest that particle configurations as represented by C10$\perp$ and C3R, may be within the range of the spherical model to give approximate information about the actual volume fraction (V"). In other words on the basis of the inversion results listed in table 5.1 and the IP spectra shown in figure 5.3, it would be hard to distinguish between the sample configurations (figure 5.4) of C10$\perp$,

C1, and C3R. However note that sample C3R appears to have longer length scales parallel to the electric field, since its parameter A/a is less than that of C10$^\perp$ and C1 (i.e. assuming A independent of grain dimensions and axial ratios).

The observation of a smaller phase slope (c) for C3R (table 5.1) relative to C10$_\perp$ and C1, also suggest a larger range of length scales. C10R has a larger length scale range and longer length scales than C3R, and is observed to have an even smaller phase slope (c) and A/a parameter. C10$_\parallel$ has the largest length scales, all oriented parallel to the electric field (note c=.47) and from a spherical model approximation would be expected to have the smallest A/a parameter of this sample group. However note that C10R actually has the smallest (A/a) in table 5.1. This apparent theoretical contradiction suggests that either C10R or C10$_\parallel$ sample conditions are not being approximated by the spherical model.

The anticipated decreasing progression of the inversion parameter A/a as the length scale (a) gets longer (table 5.1), suggest that sample C10$_\parallel$ is again (also ρI and V) giving erroneous information of actual sample conditions. For example as listed in table 4.4, sample C1 displays a Warburg impedance of copper metal of around A = .3$_\Omega$m^2. Assuming A is constant with particle orientation in the copper samples (as the spherical model assumes A is constant with grain size), note how C10$_\perp$ (table 5.1) has a similar A/a parameter as C1. Therefore one might expect similar length scales parallel to the electric field in both samples, and this is indeed observed. Next consider sample C3R which has an A/a parameter about half the magnitude of sample C10$_\perp$

and C1. From this one might expect the length scales ($\parallel$ to $\bar{E}$) in sample C3R to be about twice as long as those in sample C10$_\perp$ and C1. This is also observed to be possible. Continuing this analysis to sample C10R which shows an A/a parameter about 1/6 to 1/7 that of C10$_\perp$ and C1, length scales ($\parallel$ to $\vec{E}$) in C10R should be 6 to 7 times larger than in C10$_\perp$ and C1. This is also observed. However note that samples C10$_\parallel$, which from a spherical model approximation might be expected to have an A/a parameter 1/10 that of samples C10$_\perp$ and C1, has only a factor of 1/3 between the two samples. The inversion parameter A/a for C10$_\parallel$ is lower than anticipated as a result of V being larger and ρ_1 being smaller, than those observed for C1 and C10$_\perp$. Therefore it appears that sample conditions of C10$_\parallel$ are not represented in terms of a spherical model with respect to A/a (i.e. length scale analysis) as was also noted earlier for ρ_1 and V.

Although the inversion results of sample C10$_\parallel$ alone are unreliable, in conjunction with the inversion results of C10$_\perp$, it may be possible to estimate an axial ratio between these two samples. This estimate would indicate not only a veined texture (i.e. τ or A/a ratios not equal to unity) but also the preferred direction of orientation. For example consider the inversion results of the IP spectra from a sample or survey location measured in two perpendicular directions (e.g. samples C10$_\perp$ and C10$_\parallel$ or a veined deposits with preferred orientation). The square root (or cth root) of the ratio of the Cole-Cole time constants (OR) would be an estimate of the axial ratio between the two measurement directions. Remember for samples C 10$_\perp$ and C10$_\parallel$ the observed axial ratio was 10 while OR indicated

8.5. An axial ratio (or OR) near unity would indicate random orientation or in the special case spherical particles (e.g. disseminated deposits). Through the parallel chargeability equation (5-12) the possible accuracy of the estimate may be checked. The form factors in equation (5-12) can be determined from the estimates of the axial ratio (tables in Fricke, 1953). An estimate of the volume fraction (V") should be the inversion parameter V for the direction with the smaller time constant (τ) or larger A/a parameter (e.g. C $10^\perp$). For example the chargeabilities of sample C1 and $C10^\perp$ were similar and suggested a V" = .14 to .16 which is observed. This inversion parameter V(of $C10^\perp$) however may be biased due to low resistivity contrasts between the electrolyte and the conductive minerals (see chapter 4). Therefore with V" and $X^{\alpha,\beta}$ (i.e. from axial ratio estimates and tables listing form factors) the chargeability (equation 5-12) can be calculated for each measurement direction and then compared to the observed chargeabilities (e.g. $C10^\perp$ and $C10^\parallel$ in figure 5.4). A match between the theoretical and observed chargeabilities would indicate the assumptions (spherical model) made and the information obtained (i.e. V", axial ratio and X_i) appear to fit the data.

Based on the observations and calculation from the copper samples depicted in figure 5.4, a spherical model does appear capable of estimating some nonspherical sample configurations having axial ratios as large as 10:1:1. A preferred orientation might be inferred from the IP spectra observed from two directions of measurement as was done for $C10^\perp$ and $C10^\parallel$ using the ratio of the time constants to the cth

root. The inversion parameters V and A/a gave approximate information about the actual volume fractions (V") and length scales parallel to the electric field in samples C1, C3R, and C10⊥ . The random particle configuration of C1, C3R C10R were then distinguished on the basis of the parameters A/a and c becoming smaller with larger length scales and increased length scale ranges respectively.

CHAPTER 6

ROCK SAMPLE AND IN SITU IP SPECTRA

6.1 Introduction

Figure 6.1 shows the observed IP spectra for a core sample from
the Tyrone porphyry copper deposit near Silver City, New Mexico. Also
shown is the apparent resistivity and phase data (dashed lines)
obtained from an in situ IP measurement at the Tyrone deposit (Pelton
et. al., 1978). Although the electrolyte resistivity at the Tyrone
field site is unknown, the core sample was saturated with $0.1\,\Omega m$
electrolyte (NaCl) so that the phase peak due to sulfide
mineralization could be shifted to higher frequencies for better
analysis. In reference to figure 4.1, which shows the effect of
changing the electrolyte resistivity in a single synthetic sample, the
IP spectra in figure 6.1 would suggest a simple electrolyte variation
between the two measurements of about a factor of ten.

Note that the IP spectra (figure 6.1) for the core sample and in
situ measurements resemble those obtained for the synthetic samples in
figures 3.1, 3.2, 4.4, and 4.7. The dispersion related to the sulfide
response is symmetrical and reasonably separated from the higher
frequency dispersion. The high frequency dispersion for the Tyrone
core sample and in situ data is thought to be caused by membrane
polarization of the alteration minerals. Both high frequency

Figure 6.1 Amplitude and phase spectra for a core sample and in situ IP measurement from the Tyrone porphyry copper deposit near Silver City, New Mexico. The smooth curve is the theoretical spherical model fit to the core sample data. The dashed line is drawn through the observed Tyrone in situ IP spectra (dipole-dipole array, n=1, x=1m). Inversion results and sample statistics are listed in table 6.1.

Tyrone IP Spectra
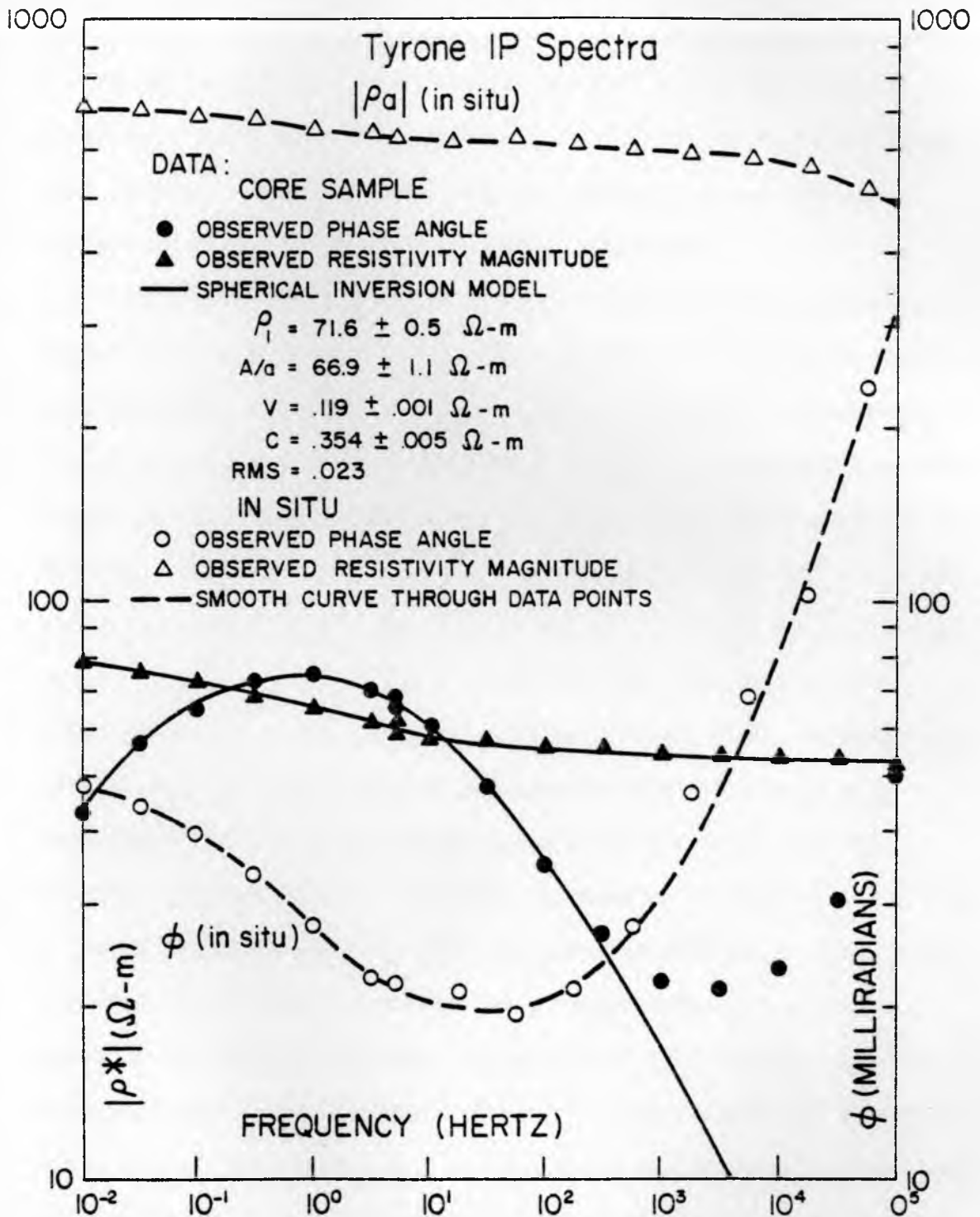
dispersions can be handled either by ignoring the high frequency data points or by using a second dispersion. The smooth curve in figure 6.1 is the theoretical model fit to the core sample data through inversion, where the high frequency (i.e. 10^3 to 10^5 hz) data points were ignored. The in situ IP data was analyzed using a second dispersion to handle the high frequency dispersion.

Table 6.1 lists the model inversion results of the data shown in figure 6.1. Also listed are the inversion results of the IP spectra obtained from a second Tyrone core sample and in situ measurement. The in situ data labeled Copper Cities 1 and 2 was obtained from the Copper Cities porphyry copper deposit in the Globe-Miami district of Arizona. This in situ IP data was collected by Pelton et. al., 1978, using a one meter dipole-dipole array (n=1) over exposed mineralized areas. Rock textures and compositions of the core samples are afforded by sample petrographic analysis (Jacobs, 1975, personal communication). Rock textures and compositions for the in situ measurements are from the actual measurement sites (Pelton, 1977, personal communication). The rocks represented in table 6.1 are from a quartz monzonite porphyry with disseminated sulfides. These rocks are from the phillic alteration zone, composed mainly of quartz, sericite and pyrite. However, Copper Cities 1 is observed to have more chalcopyrite than pyrite. The pyrite grain radii (a) listed in table 6.1 are the maximum and minimum values observed in petrographic examination. The pyrite shapes include equant, veinlet and highly irregular. Axial ratios of veinlets generally do not exceed 3:1. This suggests that the spherical inversion model can be used to

Table 6.1 Sample statistics and inversion results using a spherical model for core samples from Tyrone, New Mexico and _in situ_ IP measurements from Tyrone, New Mexico and Copper Cities, Arizona. The observed IP spectra for the core sample (T_y2) and _in situ_ IP measurement (T_y2) are shown in figure 6.1.

SAMPLE	TEXTURE DIS:VEIN	DOMINANT MINERAL	POROS-ITY ϕ_0	VOL. FRACT.		INVERTED PARAMETERS				WARBURG (Ω-m^2)		SULFIDE GRAIN RADIUS $\approx a$ (mm)	TIME CONSTANT τ (SEC)
				$\approx V'$	$\approx V''$	V	ρ_1 Ω-m	c	A/a Ω-m	$A_{min.}$	$A_{max.}$		
					"CLAY" 20%-5%								
					CORE	SAMPLES							
TYRONE 1	3:1	PYRITE	.06	.04	.13 - .27	.09	10	.38	7.4	4×10^{-6}	7×10^{-3}	.0005 - 1.0	7.9×10^{-1}
TYRONE 2	10:1	PYRITE	.03	.05	.18 - .38	.12	72	.35 ·	67	7×10^{-4}	3×10^{-2}	.01 - 4.0	4.5×10^{-1}
			IN	SITU	MEASUREMENTS	(1m	DIPOLE-DIPOLE)						
TYRONE 1	√	PYRITE		.06		.066	192	.40	55				6.4×10^{0}
TYRONE 2	√	PYRITE		.06		.087	782	.28	182				3.8×10^{1}
COPPER CITIES 1	√	CHALCO-PYRITE		.01		.12	129	.29	360				8.2×10^{-3}
COPPER CITIES 2	√	PYRITE		.10		.09	75	.34	43				1.5×10^{0}

analyze the IP data for the core samples and in situ measurements, as was done in section 5.3 for sample C3R (figures 5.3 and 5.4, table 5.1).

6.2 Tyrone Core Samples

The inversion results (table 6.1) for the core sample IP data of Tyrone 1 (Ty1) and Tyrone 2 (Ty2) show parameter trends in approximate agreement with what might be theoretically explained in terms of the observed textures and compositions of these samples.

The background resistivity (ρ_1) is in approximate agreement with equation (4-3) which gives σ_1 as a function of the porosity (ϕ_e), electrolyte conductivity ($\sigma_e = 10$ mho/m) and the effective clay conductivity (σ_s). The porosity of Ty2 is estimated to be about half that of Ty1 and, ρ_1 for Ty2 is greater than that observed for Ty1 (table 6.1). σ_s for Ty1 and Ty2 is estimated at 20 mho/m and 5.5 mho/m, respectively. For 10 mho/m electrolyte, B the equivalent conductance of the clay exchange cation (Na+) as a function of solution conductivity (σ_e) is estimated at 3.8 liter/equiv.-ohm-m. For such B values the effective clay concentration (Q_v) is 5.3 equiv./liter (Ty1) and 1.4 equiv./liter (Ty2), (Waxman and Smits, 1968). The term "clay" in this report will be loosely applied to any mineral which exhibits a degree of cation exchange capacity that will increase the electrical conductivity of the sample. Such minerals indicated in the petrographic analysis might therefore include K-mica, montmorillonite and/or kaolinite. These "clay" minerals are estimated to range between 5% to 20% by volume. With this amount of "clay" the

effective clay concentration (q_m, equation 4-5), where the density of "clay" (ρ_c) is estimated at 2 g/cc, is 100-300 meq./100 g and 10-40 meq./100 g for Ty1 and Ty2, respectively. The q_m values for Ty1 and Ty2 are comparable to the q_m values obtained in studies using kaolinite and montmorillonite of 3.0-5.0 meq./100 g and 80-150 meq./100 g respectively (Keller and Frischknecht, 1966). Therefore as is observed in the core samples, equation (4-3) suggests a degree of "clay" mineral content which increases the sample conductivity due to increased surface conduction.

Equation (4-6) determines the volume fraction V" to which the inversion parameter V is sensitive. However V" is relative to the pore space volume (ϕ_e), the volume fraction (V') of the sulfide minerals in the sample, and the volume fraction (V_c) of "clay" minerals. The petrographic analysis indicates a range for V_c between .05 and .20 in the Tyrone core samples and a V' between .04 and .05. Although the inversion parameter V for Ty1 and Ty2 are similar, V for Ty1 is slightly smaller suggesting a smaller volume fraction (V"). This is in agreement with Ty1 having a larger porosity (ϕ_e) and larger effective clay concentration (Q_v) than does Ty2. With the range of possible "clay" content, equation (4-6) was used to estimate V" for each core sample as listed in table 6.1. As can be seen the volume of "clay" minerals can have a strong influence on V", so that estimates of V" range between .13 and .38. Note that the lower limit of this range is close to the inversion parameter V obtained for Ty1 (V=.09) and Ty2 (V=.12). Although the V" estimates may be in error, this

would imply near maximum polarization. Therefore the inversion parameter V might be assumed to be giving approximate information about V". However if V" lies in the upper part of the estimated range then maximum polarization (i.e. $\rho_3/\rho_e \gtrsim 10^{-2}$) cannot be assumed, as was observed for the synthetic sample containing pyrite and saturated with an electrolyte of similar resistivity (see sample H-5, figure 4.1, table 4.1).

Therefore to interpret the inversion parameter V, several estimates and assumptions were necessary as to the rock porosity, electrolyte and mineral resistivity, "clay" and sulfide content and particle shape (assumed spherical). Although the variable estimates for the core samples have the theoretical capability of producing the observed inversion parameter V, such estimates are not usually available for exploration sites. Therefore the practical application of the inversion parameter V for exploration purposes appears to be limited, except for possible relative magnitude comparison between other measurement sites or different measurement direction at one site. However note that due to a variable "clay" content the magnitude of the phase response (i.e. V or m) can be quite different for equal volume fraction (V') of sulfide in the deposit.

The frequency dependence (c) or the asymptotic phase slope for the Tyrone core samples is around c=0.4, and the grain size range listed in table 6.1 are observed to have a two to three order of magnitude spread. Modeling of normal distributions of volume fractions for grain sizes differing by two to three orders of magnitude gave similar asymptotic phase slopes. Therefore the

observed data seems to be in agreement with the model using a summation of dispersions exhibiting a Warburg frequency dependence (i.e. c=0.5).

The inversion parameter A/a for the Ty2 core sample is about ten times larger than that observed for Ty1 (table 6.1). Assuming the pyrite in both core samples have similar Warburg impedances, the difference in the inversion parameter A/a indicates that Ty1 has larger length scales than Ty2. As can be seen in table 6.1 the textural observations do indicate a greater percentage of veinlets in Ty1 than in Ty2. Multiplying the observed grain size range by the inversion parameter A/a, estimates are obtained for the Warburg impedance range (A_{min} to A_{max}). As seen in table 6.1 the Warburg impedance range is rather large for mineral discrimination purposes due to the range of possible grain sizes. However the upper limit of this range (A_{max}) does approach that observed for the synthetic pyrite sample having similar electrolyte ion concentrations (see sample H-5, $A = 0.1 \ \Omega m^2$, figure 4.1, table 4.1).

The observed trends in the inversion parameters of the Tyrone core samples are in approximate agreement with the theoretical model considering the range of sample variables estimated from the petrographic report. The background resistivity (ρ_1) was a function of the porosity, the electrolyte resistivity and the effective clay resistivity (ρ_s). Although the porosity and electrolyte resistivity can vary in natural environments, in some cases a low background resistivity may be an indication of "clay" alteration. The magnitude of the inversion parameter A/a appears to be mainly a function of

grain size in the core samples, suggesting that relative comparison between other samples' inversion results might be used to distinguish textural differences. The inversion parameter c (i.e. phase slope) suggest a range of grain sizes in the core sample. The inversion parameter V suggest similar volume fractions of pyrite. However due to the number of variables that can affect the inversion parameter V, especially the "clay" content, its practical application appears limited to relative comparison between inversion results of other samples or measurement directions.

6.3 Tyrone In Situ IP Data

The inversion results (table 6.1) of the Tyrone _in situ_ IP data (Ty1 and Ty2) show similar trends in all the inversion parameters as observed in section 6.2 for the Tyrone core samples. The similarity between the inversion results suggest that the core samples might be representative of the field sites. Therefore the general information obtained from the petrographic analysis of the Tyrone core samples will be used in conjunction with the actual site observations, to aid in the analysis of the _in situ_ IP data. The general conclusions in this section are essentially the same as discussed in section 6.2.

The background resistivity (ρ_1) for field site Ty2 is greater than Ty1 field site, as observed for the Tyrone core samples (table 6.1). Therefore suggesting that the Ty2 field site has a smaller porosity and/or "clay" content, than at the Ty1 field site. Note that ρ_1 for field sites Ty1 and Ty2 are both around a factor of ten greater than that observed for their respective core samples. This suggests a

pore water resistivity of 1.0 Ωm relative to the core sample electrolyte resistivity of 0.1 Ωm. Although such electrolyte resistivities were roughly measured in the various field site areas (i.e. ρ_e = 1 Ωm to 100 Ωm), these measurements were performed on water lying on the ground surface. Therefore these surface waters may not be representative of the actual pore waters due to the possibility of contamination (e.g. rain water). However the predicted value of 1.0 Ωm for the Tyrone pore water resistivity does approach the observed surface water resistivity range.

Since the electrolyte resistivity at the field sites are indicated to be greater than that used in the core samples, a greater degree of polarization at the field sites might be expected (assuming the core samples did not obtain maximum polarization). Therefore one might expect a larger inversion parameter V for the field site data. While the inversion parameter V (table 6.1) for the Ty field sites show a similar trend as the core samples, they are smaller than those observed for the core samples. This would indicate that on the average the core samples contain more pyrite. Although estimates of the pyrite content V' listed in table 6.1 would suggest the opposite, the petrographic analysis did mention that up to 10% by volume of the thin-sections were open space which could result from plucking during thin-section preparation.

As in the Tyrone core samples, the inversion parameter A/a for field site Ty2 is larger than observed for field site Ty1 (table 6.1). While the field site observations indicate a veined texture for both, the difference between the inversion parameter A/a suggest that field

site Ty1 has larger length scales parallel to the measurement
directions. Note that the core sample (Ty1) textural observations
indicate a greater portion of veinlets to disseminated pyrite than
observed for Ty2. Although larger length scales do not necessarily
imply a greater degree of veining, the larger grain dimensions are
generally associated with the pyrite veinlets in the petrographic
report. Relative to the core samples, the A/a parameters are larger
for the in situ measurements suggesting a greater Warburg impedance of
pyrite (assuming similar grain sizes). In the synthetic samples the
Warburg impedance of pyrite was observed to increase with increasing
electrolyte resistivity (see figure 4.1, table 4.1). This suggests
the increase in the Warburg impedance indicated for the Tyrone field
site data (relative to the core samples) is due to a greater
electrolyte resistivity.

If the data points $(\rho_1/A_{max}, \tau)$ from all the Tyrone inversion
results were plotted in figure 4.2, the data points fall near the
extension (top of figure 4.2, off scale) of the line formed by the H-1
to H-5 synthetic sample data points. Although A_{max} was arbitrarily
chosen, data points falling on the same line in figure 4.2 would
suggest similar grain dimensions for all samples. The grain size $H(\bar{a}$
= .44 mm) is within the grain radius range observed for the core
samples (i.e. 5.0×10^{-4} mm $< a < 4.0$ mm).

The phase slope (c) for the Ty field sites are similar to those
of the core samples (table 6.1). While Ty2 field site displays a
smaller phase slope (c=.3) than field site Ty1 (c=.4) suggesting
length scale range differences, when working with two dispersions to

remove membrane polarization or inductive coupling, small differences in phase slopes between inversion results can be misleading due to the correlations between the two dispersions.

In summary, the inversion results of the Tyrone in situ IP measurements using a spherical model show parameter trends in agreement with the textural and composition observations at the measurement sites and in the core samples. Simple observations of the inversion results would suggest length scale differences (or in some cases Warburg impedance variations) from the parameter A/a. The background resistivity (ρ_1) indicates porosity and/or "clay" concentration differences (or in some cases electrolyte variations). The inversion parameter V is similar for both field site data suggesting comparable volumes of pyrite. Although the field site observations tend to support this conclusion, porosity and "clay" content variations can affect different V inversion parameters for comparable total sulfide content (V'). The asymptotic phase angle slopes (c) indicates a two to three order of magnitude spread in the length scale range.

6.4 Copper Cities In Situ IP Data

The Copper Cities (CC1 and CC2) inversion results and field site observations show different trends in the data. The textural observations in table 6.1 indicate that disseminated sulfide predominates over sulfide veins for both CC1 and CC2 field sites. Field site CC1 however contains more chalcopyrite than pyrite, while for field site CC2 pyrite is the dominant mineral. The total sulfide

content (V') is quite different for the two Copper Cities deposits. While field site CC1 shows a V' = .01, field site CC2 shows a V' = .10 (table 6.1).

The background resistivity (ρ_1) for field site CC1 (ρ_1 = 129 Ωm) is greater than that observed for field site CC2 (ρ_1 = 75 Ωm). While changes in the porosity (ϕ_e), "clay" content (V_c) and electrolyte resistivity (ρ_e) can cause ρ_1 variations, the inversion parameter V and the field site observations of V' suggest that ϕ_e and V_c are responsible for the observed ρ_1 difference and that ρ_e might be similar for the two Copper Cities deposits. For example, the inversion parameter V is similar for the two field sites (i.e. V= 0.1, table 6.1), while the observed V' differ by a factor of ten. It would appear from equation (4-6) that for a 1% (CC1) sulfide content to produce a comparable inversion parameter V (sensitive to V") to that of a 10% (CC2) sulfide content, that the porosity (ϕ_e) and/or "clay" content (V_c) must be smaller at field site CC1 than at field site CC2. The petrographic report (Jacobs, 1975, personal communication) of core samples from the two Copper Cities deposits does indicate that the CC2 core sample is pervasively altered making it difficult to obtain evidence for an igneous origin. Although no "clay" percentages are given, this would indicate that field site CC1 has a smaller "clay" content than field site CC2.

Therefore in comparing the inversion parameter V between samples or in situ measurements, variations in the porosity and "clay" content must be considered. If exploration sites are in the same general area, the electrolyte resistivity and porosity might be assumed

comparable, so that variations in the inversion parameter ρ_1 may give information about the relative "clay" content between sites. That is the lower background resistivity might indicate a greater degree of mineral alteration between neighboring sites. In the case of field sites CC1 and CC2 the more extensive alteration (CC2) was associated with the greater sulfide content per rock volume.

The asymptotic phase slope ($\bar{c}$ = .3) for the Copper Cities deposits (table 6.1) indicates a two to three order of magnitude difference in the length scale range (i.e. assuming a log normal volume fraction distribution). The field site observations indicate a disseminated sulfide texture and the petrographic report of samples from each field site does suggest a two to three order of magnitude variation in grain radius (a) from .005 mm to 1.0 mm. Although phase slope observations can be misleading (i.e. dispersion correlations), they may serve to indicate a larger (c=.1 to .3) or smaller (c=.3 to .5) grain size range. In the case of field sites CC1 and CC2 similar length scale ranges are indicated (i.e. $\bar{c}$ = .3), however note that this does not necessarily mean similar grain sizes.

In view of the core sample observations of similar grain sizes, variations in the inversion parameter A/a between field sites CC1 and CC2 may be an indication of mineral Warburg impedance (A) differences. As can be seen in table 6.1, the inversion parameter A/a for field site CC1 (dominant mineral chalcopyrite) is greater by about a factor of 8 than that observed for field site CC2 (dominant mineral pyrite), suggesting a larger Warburg impedance for the chalcopyrite at field site CC1. Although the chalcopyrite and pyrite used in the synthetic

samples was not obtained from the Copper Cities deposits, chalcopyrite was observed to generally have a larger Warburg impedance value by about a factor of 1 to 5 (i.e. from A_{min} and A_{max} values, table 4.4) than that observed for pyrite. It would appear then that the larger inversion parameter A/a for field site CC1 is caused by a larger Warburg impedance of chalcopyrite. While the inversion results (A/a) and actual field site observations for the Copper Cities deposits suggest the possibility of relative mineral discrimination, the grain size must also be considered. Due to the possible greater variation in grain size (see table 4.3) relative to the apparent limited range of mineral Warburg impedance values (see table 4.4), this method of mineral discrimination should be applied cautiously.

In summary, the inversion results of the Copper Cities in situ IP measurements using a spherical model show parameter trends in agreement with the textural and composition observations at the measurement site and in core samples. By assuming some average porosity and electrolyte resistivity, the difference in the background resistivity between field sites CC1 and CC2 was attributed to a variable "clay" content. Similarly the comparable magnitude of the inversion parameter V between field sites CC1 and CC2 produced by different total sulfide contents (V') was attributed to a variable "clay" content. The asymptotic phase angle slope (c) suggested a two to three order of magnitude spread in the length scale range as did the phase slopes obtained at Tyrone. Although variations in both the grain size and Warburg impedance can be responsible for changes in the inversion parameter A/a, the observed difference in inversion results

(A/a) for the two Copper Cities field sites appear to be a function of the Warburg impedance of chalcopyrite.

CHAPTER 7

CONCLUSIONS

Two simple rock models have been derived for complex resistivity.
The two models consider the inhomogeneous background medium composed
of electrolyte and a nonconductive rock matrix. The models account
for the frequency dependent behavior occurring at the
electrolyte-conductive mineral interface and, considers the
microscopic (Model 2) charge separation occurring in the diffuse zone
and the macroscopic (Model 1) decay of the charge build up into the
surrounding background medium. The time constant (τ) of the Cole-Cole
model (equation 2-27, model 2) was a function of ρ_1, a, A, ρ_3 and V'.
While the chargeability (m) (equation 2-26, model 2) was a function of
V", ρ_3 and ρ_e. Although the models are based on spherical particles,
it can be applied to some nonspherical conditions, which can typically
exist in natural environments.

The ellipsoidal model for parallel orientations was put in terms
of a single Cole-Cole dispersion. Both the chargeability (m_i^p)
equation (5-12) and the time constant (τ_i^p) equation (5-16) did an
approximate job of predicting the observed data. An ellipsoidal model
was developed for random orientations and approximated in terms of a
multiple Cole-Cole dispersion model (equation 5-17). The
chargeability (m^R) equation (5-15) seemed to do a better job of
predicting the observed data than the time constant (τ_i^p) equation

(5-16). However, due to the number of unresolvable parameters in these models with respect to the IP data, a simple spherical model approximation was attempted with some success.

The four basic parameters of the spherical model are the background resistivity (ρ_1), mineral volume fraction (V"), the frequency dependence (c), and the interface parameter A/a. The background resistivity is essentially a function of the porosity (ϕ_e), electrolyte resistivity (ρ_e) and the "clay" content (V_c). The volume fraction (V") is relative to the pore space and "clay" content and not the total rock volume. Low resistivity contrasts between the electrolyte (ρ_e) and the mineral (ρ_3) can result in less than maximum polarization so the inversion parameter V may be smaller than the observed V". The frequency dependence (c) or the asymptotic phase slope is a function of the frequency dependence of the Warburg impedance and the range of length scales parallel to the electric field. The parameter A/a is a combination of the Warburg impedance (A) and the mineral grain radius (a). The Warburg impedance depends on the type of mineral and the electrolyte ion concentration, and does not vary over many orders of magnitude.

In order to apply the model to core samples and _in situ_ IP spectra, it is essential to obtain as much information about the phase peak associated with the mineralization as possible. Otherwise the inversion parameters will not be resolved due to significant correlations developing between parameters. Due to the number of variables which can affect each inversion parameter, the practical application of this model to _in situ_ measurements lies in relative

comparison between inversion results obtained at different sites or measurements taken in two directions at the same site.

APPENDIX 1

SPHERICAL BOUNDARY VALUE PROBLEM

Spherical Particles

Figure 2.1 shows a model for a single sphere of conductivity σ_3 with a thin surface layer (σ_2), embedded in some background medium (σ_1). These three regions represent respectively the sulfide particle, the diffuse zone between the particle and the electrolyte, and the medium surrounding the particle which in some cases might be the rock matrix with electrolyte filled pore passagaes. In relating this model to rock sample measurements, using low current densities, several assumptions are made.

1. Conductivity is a complex function of frequency.

2. Displacement currents are negligable.

3. All media are linearly conductive, isotropic, homogeneous and have electrical properties which are independent of time, temperature and pressure over the measurement time scale.

4. The background medium is frequency independent.
Provided assumptions 1, 2 and 3, the current density is related to the electric field by the constitutive relation

$$\vec{J} = \sigma^* \vec{E} \, e^{j\omega t} \qquad , \qquad \text{(A-1)}$$

Due to the models' spherical symmetry where,

1. Conductivity is only a function of radius.

2. The applied electric field is in the $\theta = 0$ direction.

3. No ϕ dependence.

The potential fields obeying Poisson's equation reduce to

$$\phi_1 = -E_0\cos\theta + \frac{B_1}{r^2}\cos\theta \qquad , \qquad \text{(A-2)}$$

$$\phi_2 = A_2 r\cos\theta + \frac{B_2}{r^2}\cos\theta \qquad , \qquad \text{(A-3)}$$

$$\phi_3 = A_3 r\cos\theta \qquad . \qquad \text{(A-4)}$$

Given assumption 3,

$$\vec{E} = -\nabla\phi \qquad , \qquad \text{(A-5)}$$

and the electric fields in each region becomes

$$\frac{\partial\phi_1}{\partial r} = -E_0\cos\theta - \frac{2B_1}{r^3}\cos\theta \qquad , \qquad \text{(A-6)}$$

$$\frac{\partial\phi_2}{\partial r} = A_2\cos\theta - \frac{2B_2}{r^3}\cos\theta \qquad , \qquad \text{(A-7)}$$

$$\frac{\partial\phi_3}{\partial r} = A_3\cos\theta \qquad . \qquad \text{(A-8)}$$

By applying the conditions of continuous electric potential and normal current densities at the boundaries of this model, using the six field equations, the unknown field constants can be determined where at r=b

$$A_2 + \frac{B_2}{b^3} = -E_o + \frac{B_1}{b^3} \qquad , \qquad \text{(A-9)}$$

$$\sigma_2\left(A_2 - \frac{B_2}{b^3}\right) = \sigma_1\left(-E_o - 2\frac{B_1}{b^3}\right) \qquad , \qquad \text{(A-10)}$$

and at r=a

$$A_3 = A_2 + \frac{B_2}{a^3} \qquad , \qquad \text{(A-11)}$$

$$\sigma_3 A_3 = \sigma_2\left(A_2 - \frac{2B_2}{a^3}\right) \qquad . \qquad \text{(A-12)}$$

In preparing the model for a surface frequency dependent behavior being related to the thin surface layer, its thickness (t) is substituted here by setting

$$b = a + t, \qquad \text{(A-13)}$$

and shrinking it essentially to zero so that

$$t/b \ll 1 \qquad , \qquad \text{(A-14)}$$

and

$$b^3 \approx a^3 \qquad \text{(A-15)}$$

With this approximation and the proper substitutions, using the boundary conditions at r=b, the dipole term B_1 becomes

$$B_1 = \frac{a^3 E_o\left[1 - \left(\frac{\sigma_1}{\sigma_3} + \frac{\sigma_1 t}{\sigma_2 a}\right)\right]}{\left[1 + 2\left(\frac{\sigma_1}{\sigma_3} + \frac{\sigma_1 t}{\sigma_2 a}\right)\right]^2} \qquad . \qquad \text{(A-16)}$$

Therefore the total expression for the electric potential in region 1, equates to

$$\phi_1 = -E_o r \cos\theta + \frac{a^3 \left[1 - (\frac{\sigma_1}{\sigma_3} + \frac{\sigma_1 t}{\sigma_2 a})\right]}{r^2 \left[1+2(\frac{\sigma_1}{\sigma_3} + \frac{\sigma_1 t}{\sigma_2 a})\right]} E_o \cos\theta \qquad . \qquad (A-17)$$

$$\underset{\text{source}}{} \qquad \underset{\text{dipole}}{}$$

APPENDIX 2

SYNTHETIC SAMPLE COMMENTS

A.2.1 Sample Construction

The samples consist of a mixture of Portland cement, quartz sand and various semiconductive minerals (e.g. pyrite) which was contained in a plastic (Lucite) sleeve (Figure A.2.1). Some samples were made under uniaxial pressure to reduce the porosity. The samples were saturated with an electrolyte (NaCl) for about two weeks to allow equilibrium between the electrolyte and samples' contents to be reached. To avoid using large amounts of electrolyte, rubber stoppers were placed in the ends of the Lucite sleeve and then sealed with a rubber cement. The samples were then measured with a four electrode arrangement over the frequency range of 10^{-2} to 10^5 hz. Fine meshed brass screening was used for the current and potential electrodes (Figure A.2.1).

A.2.2 Semiconductive Mineral Shapes

Pyrite was generally equidimensional, however a small portion of 3:1 axial ratios were observed. Platy minerals such as molybdenite and graphite displayed triaxial ellipsoid shapes. The sieving process was biased toward the selection of the intermediate (β) axis ($\alpha > \beta > \gamma$). Galena was cubic in shape. Chalcopyrite displayed mixtures of equidimensional to irregular shaped grains. The irregular
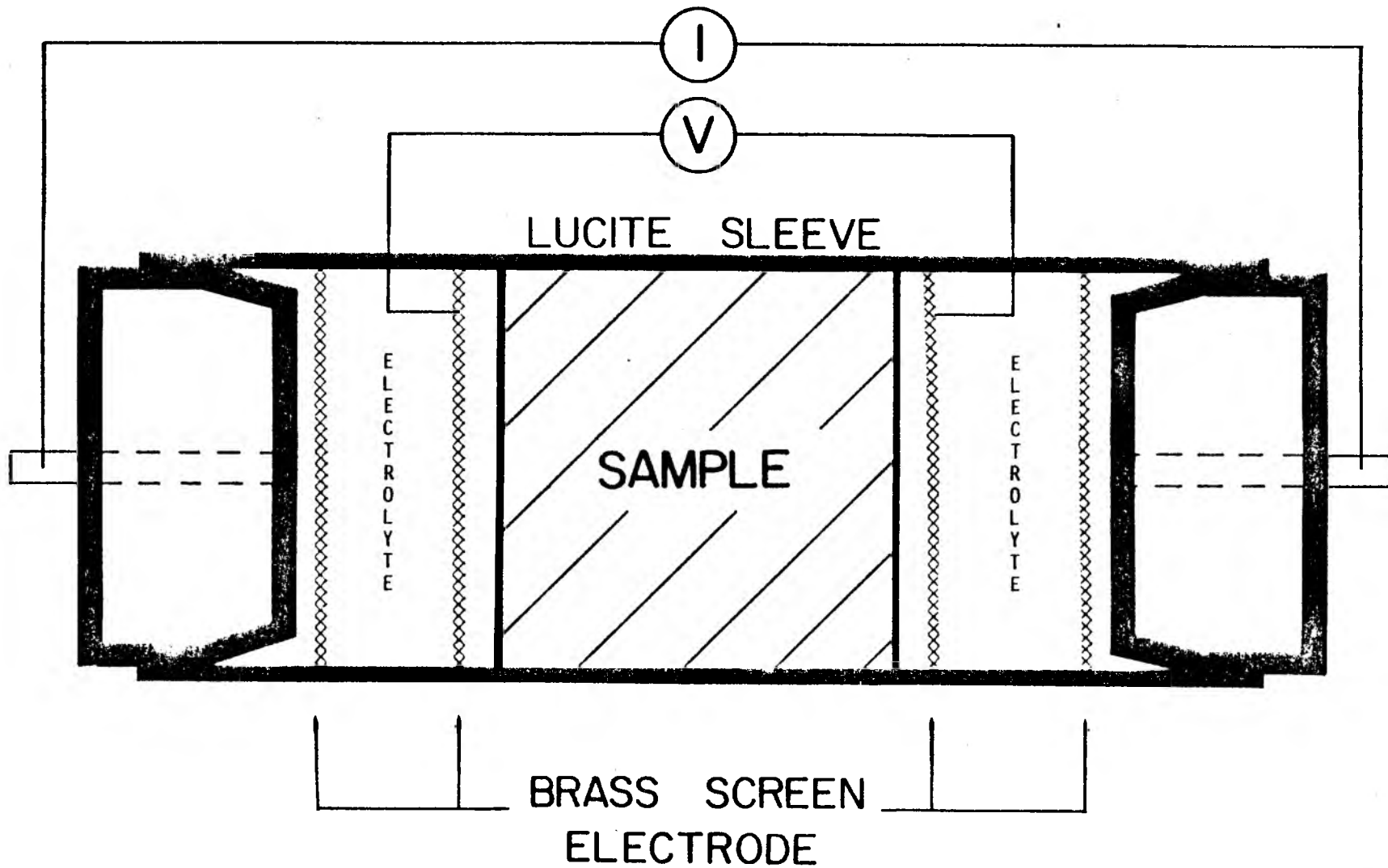
Figure A.2.1 Diagram of the synthetic sample
              construction showing current and
              potential electrode contacts.

BRASS SCREEN
ELECTRODE

particles often displayed axial ratios on the order of 3:1.

A.2.3 Quartz Sand

The quartz sand used in the synthetic samples was of a very uniform size and rounded shape. Due to the uniform sand size, the minerals of smaller grain size began to fit into interstitial positions between the larger quartz grains. This results in sample inhomogeneities with respect to the fine grained minerals. Therefore if one wishes a more homogneous distribution of mineral grains, the quartz sand should be of similar (or smaller) dimensions.

A.2.4 Cementing Agents

In order to reduce the sample porosity, fine grained cementing agents were used which could fit into interstitial spaces between the quartz and mineral grains. Both plaster of paris and a low alkali Portland cement were investigated. While both aided in the porosity reduction, little if any difference was observed in the resulting IP spectra of the synthetic samples. Due to the large total surface area of both cementing agents, membrane polarization was observed at the higher frequencies measured (see Figure 3.3). The Portland cement was preferred due to its bonding strength, especially when samples were constructed under pressure. Over a period of one year the synthetic samples became more resistive. Small translucent bladed crystals were observed in the samples after a period of time. It appears some form of recrystallization occurred, which might possibly be related to the Portland cement, causing the porosity to decrease. The electrolyte resistivity however did show a slight increase over the one year

period.

A.2.5 <u>Sample Construction Under Pressure</u>

The synethetic samples were constructed under variable uniaxial pressure conditions to obtain small porosities. Samples which display 10% to 15% porosities (tables 4.2, 4.3 and 5.1) were constructed under 5,000 psi for a period of 12 to 24 hours. Samples displaying 20% to 25% porosities (table 4.4) were hand packed and no confining pressure was applied. Samples displaying 40% porosities (table 4.1) contained no cement and the quartz sand and pyrite mixture was held in place with brass screening which served as potential electrodes.

Although it was desirable to obtain low porosities which would approximate actual rock porosities, the variable porosities were adequately represented in the background resistivity (ρ_1). Therefore, I would suggest not using cement so that membrane polarization can be avoided. If low porosities are necessary, a mixture of large and small quartz sand might be used, in place of large quartz grains and cement.

REFERENCES

Archie, G. E., 1942, The electrical resistivity log as an aid in determining some reservoir characteristics: Am. Inst. Mining Met. Eng., Tech. Publ. 1442.

Collet, L. S., 1959, Laboratory investigation of overvoltage, in Overvoltage Research and Geophysical Applications: New York, Pergamon Press.

Fricke, H., 1924, A mathematical treatment of the electric conductivity and capacity of dispersed systems, I. The electric conductivity of a suspension of homogeneous spheroids: Phys. Rev. 24, p. 575-587.

Fricke, H. 1953, The Maxwell-Wagner dispersion in a suspension of ellipsoids: J. Phys. Chem., Vol. 57, p. 934-937.

Frohlich, H., 1949, Theory of Dielectrics: Oxford Univ. Press, London, p. 169.

Grahme, D. C., 1947, The electric double layer and the theory of electro-capillarity: Chem. Rev. Vol. 41, p. 441.

_____, 1952, Mathematical theory of the faradaic admittance: Jour. of Electrochem. Soc., Vol. 99, p. 370.

Grissemann, C., 1971, Examination of the frequency-dependent conductivity of ore-containing rock on artificial models: Scientific Report No. 2, Electronics Laboratory, University of Innsbruck.

Keller, G. V., and Frischknecht, F. C., 1966, Electrical Methods in Geophysical Prospecting: Pergamon Press, New York, p. 23.

Klein, J. D., and Pelton, W. H., 1976, A laboratory investigation of the complex impedance of mineral-electrolyte interfaces: presented at the 46th annual international meeting of the SEG, Houston, Texas, October 26, 1976.

MacDonald, J. R., 1953, The theory of ac space-charge polarization effects in photoconductors, semiconductors, and electrolytes: Phys. Rev., Vol. 92, p. 4.

Madden, T. R., and Marshall, D. J., 1958, A laboratory investigation of induced polarization: USAEC Report RME-3156.

Marquardt, D. W., 1963, An algorithm for least squares estimation of nonlinear parameters: J. Soc. Indust. Appl. Math., No. 2, p. 431-441.

Pelton, W. H., Ward, S. H., Hallof, P. G., Sill, W. R. and Nelson, P. H., 1978, Mineral discrimination and removal of inductive coupling with multifrequency IP, accepted for publication in Geophysics.

Pridmore, D. F., and Shuey, R. T., 1975, The electrical resistivity of galena, pyrite, and chalcopyrite: American Mineralogist, Vol. 66, p. 248-259.

Scott, W. J., and West, G. F., 1969, Induced polarization of synthetic high-resistivity rocks containing disseminated sulfides: Geophysics, Vol. 34, p. 87-100.

Shuey, R. T., 1975, Semiconducting Ore Minerals: Elsevier Sci. Pub. Co., New York, p. 116-319.

Van Beek, L. K. H., 1967, Dielectric behavior of heterogeneous systems, in J. Birks (Editor), Progress in Dielectrics: Heywood, London, Vol. 7, p. 69-114.

Wait, J. R., 1959, A phenomenological theory of overvoltage for metallic particles, in Overvoltage Research and Geophysical Applications: Pergamon Press, London, p. 22.

Ward, S. H., and Fraser, D. C., 1967, Conduction of electricity in rocks, in Mining Geophysics, vol. II: Tulsa, Society of Exploration Geophysicists.

Waxman, M. H., and Smits, L. J. M., 1968, Electrical conductivities in oil-bearing shaly sands: Soc. of Petroleum Eng. Jour., vol. 8, p. 107-122.